MSc thesis in Marine Technology

PIV measurements of a fast ship's diffuser stern

R.I.Tiel – 4355008
August 18, 2021

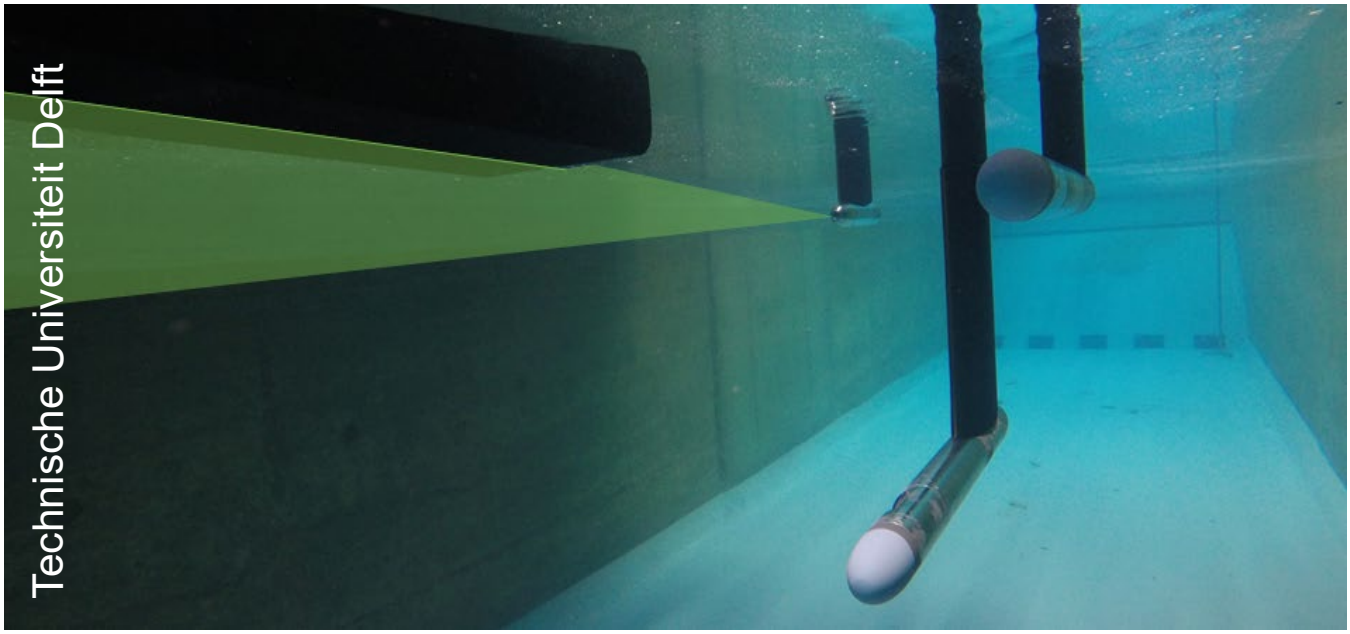

TU Delft

DAMEN

PIV measurements of a fast ship's diffuser stern

MSc Thesis

by

R.I. Tiel

to obtain the degree of Master of Science
at the Delft University of Technology,
to be defended publicly on Friday August 27, 2021 at 14:00

Student number:	4355008	
Thesis committee:	Dr. ir. I. Akkerman,	TU Delft, Chair of committee
	Dr. ir. A.A. Kana,	TU Delft
	Dr. ir. G. Jacobi,	TU Delft
	Dr. ir. A.K. Rijkens,	Damen Shipyards

An electronic version of this thesis is available at `http://repository.tudelft.nl/`.

Summary

Fast ships sailing in waves encounter high vertical peak accelerations caused by large heave and pitch motions that limit the ship's speed and can be harmful to the crew. The interceptor diffuser is a design concept that has the potential to decrease vertical peak accelerations. This research aims to contribute to the development of the interceptor diffuser, which potential is proven in model scale experiments from Rijkens et al. [2013]. By creating a negative lift force induced by the diffuser shape of a fast ships' stern, the range of lift forces is increased relative to the conventional interceptor, and the pitch motions can be influenced. The first step to improve the interceptor diffuser stern is to get an understanding of the flow field, specifically about the effect of the shape on the acceleration and detachment of the flow on the negative lift force that is created. Also, the effect of velocity, trim angle, and pitch oscillations are examined. With Particle image velocimetry (PIV) measurements combined with force measurements, the flow field is obtained, and the effect on the negative lift force is examined. Additionally, the experimental data is used to validate the CFD results of a pre-study performed by Damen Shipyards.

PIV measurements capture the flow field under the diffuser stern. In a model scale experiment with a fast ship ($L_{wl} = 1.52m$), the water is seeded with particles. A laser light illuminates the particles, and with two high-speed cameras, pictures from the particles under the diffuser stern are made. Local velocities are found with the displacement of the particles between two pictures. Simultaneously the forces are measured to find the lift and drag force of the diffuser stern relative to a straight stern.

It was found that the stern radius of 70 mm leads to an increase of negative lift relative to the stern with a radius of 50 mm. The increase of negative lift is beneficial for the seakeeping behavior because the range of lift that the interceptor diffuser configuration can create increases. Additional side plates only increased the negative lift for higher velocities. The increase of negative lift by the largest stern radius can be explained by the fact that the flow acceleration is higher relative to the straight stern and that the attachment length was longer. The relative acceleration decreased with velocity. Also, the attachment length of the flow decreased with velocity.

The results of the CFD pre-study gave a good agreement for the straight stern and the stern with a radius of 50 mm. Regarding the development of the boundary layer, the flow detachment point, and the resulting lift force. For the 70 mm stern, the CFD over predicted the negative lift force compared to the measured force. An explanation is that a smaller grid size may give a more accurate representation of the negative lift since the lift did not converge in the grid convergence study.

Acknowledgment

The research initiative about PIV measurements of a fast ship's diffuser transom started from my interest in the exciting things in ship hydromechanics: fast ships, high waves, and heavy weather.

I contacted Albert Rijkens from Damen Shipyards to ask if he had an idea for a graduation topic about fast ships, of which you can say that it is one of Damen Shipyards' specialties. They wanted to know more about the interceptor diffuser system to improve the seakeeping behavior of fast ships in waves. Thanks to Gunnar Jacobi, I got the opportunity to research this topic with PIV experiments. Gunnar and Albert guided me through this project together and allowed me to make it my own, for which I want to thanks them both. Ido Akkerman also helped in this project by providing feedback and a fresh view of my work. Last but not least, I would like to thank the external committee member Austin Kana for assessing the quality of my work.

At times, especially during a COVID-19 lockdown, writing a thesis did not feel satisfactory. Fortunately, there were more exciting times where I was allowed to perform PIV experiments at the university. These wouldn't be possible to carry out without the help of the towing tank crew: Jasper den Ouden, Peter Poot, Jennifer Rodrigues Monteiro, and Pascal Chabot. I also would like to thank Sebastian Sigmund from Damen, who provided the CFD study and made time for interesting discussions.

Not only the people from the TU Delft and Damen have been a support. I also want to thank my friends and roommates for the good distraction moments and Joris, who has an endless repertoire of motivational speeches. I did not always believe that I was able to finish this project. But in the end, here is a report that I hope you, all readers, enjoy reading.

R.I. Tiel
Rotterdam, August 2021

Contents

1

Introduction

1.1. Problem statement

1.1.1. Vertical peak accelerations of fast ships sailing in waves

Fast ships sailing in head waves encounter high vertical peak accelerations. The slamming on the waves causes these vertical peak accelerations due to large heave and pitch motions. The heave and pitch motions are large because fast ships are relatively short compared to the wavelength. Besides that, the encounter frequency can be close to the natural pitch frequency, leading to resonance in the pitch motion. Figure 1.1 shows an example of a moment when the fast ship is about to “fall” after sailing over a wave crest. This will induce the upward vertical acceleration peak.

Figure 1.1: Type NH1816 SAR vessel in head waves (KNRM/Flyingfocus [2015])

The impacts can induce severe injuries to the crew (Margés [2018]) or are at least uncomfortable. The regulations of the Maritime and Agency say that the limit for a ”whole-body vibration” is 1.15 m/s^2. However, De Jong [2011] found that accelerations of 3G are still reached on SAR vessels. Van Deyzen [2014] found that the crew finds 1G acceptable and that the crew of search and rescue vessels voluntarily decreases speed. This is undesirable for a fast ship, supposed to be as fast as possible for search and rescue operations. Another uncomfortable motion of fast ships in waves is the roll motion, occurring in almost any wave condition.

1.1.2. Current solutions and their limitations

Several solutions have been developed to reduce the vertical peak accelerations of fast ships sailing in head waves. Two mitigating solutions are springy seats that can compensate a part of the vertical accelerations and a proactive control system to adapt the speed to reduce the vertical accelerations with a minimized speed reduction (Rijkens [2016]). There are also examples of changes in hull design that have been made. Two hull changes to reduce vertical peak accelerations are the ESC (enlarged ship concept) from J.A. Keuning and van der Velde [2002] and the axe bow from Keuning et al. [2002].

Also, appendages like a trim flap and the interceptor are commonly used to improve the seakeeping behavior. Both devices create a force at the stern and induce a moment to influence the pitch motion of the ship. A trim flap is used dynamically on fast ships in waves to reduce the pitch motions (Dawson and Blount [2002]). The angle of the flap at the stern can be changed with a hinge. An interceptor is a vertical plane at the stern which height can be changed. This system is widely implemented stationary for resistance reduction in calm water. The interceptor plate can also be used dynamically. Both create a positive lift at the stern to trim the bow down (Brizzolara [2003]). Figure 1.2 shows the systems and the resulting pressure distribution. Either system creates a high pressure under the stern by decelerating the flow. In the case of the interceptor, the flow is even stagnated. Dawson and Blount [2002] concluded that the lift that the interceptor and trim flap can create is similar at the same drag. There are also combinations known of the flap and interceptor that reach a higher positive lift (Song et al. [2018]).

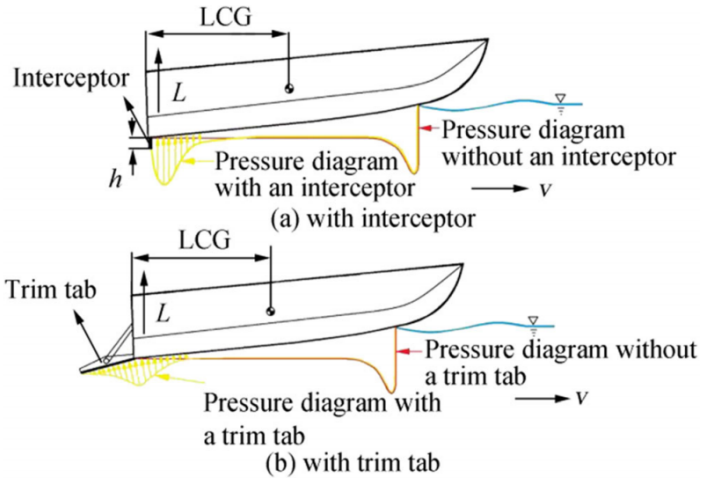

Figure 1.2: Pressure distribution interceptor and trim flap (Sakaki et al. [2019])

The appendages can potentially also reduce roll motions by using them asymmetrically and thereby creating a rolling moment beside the trimming moment.

A trim flap can only create a small negative lift because the flow starts to separate at the sharp edge that occurs with a negative angle of the trim flap (Cleijsen [2013]). The conventional interceptor cannot create a negative lift. The ability to create a negative lift increases the influence on the pitch motion and sequentially the influence on the pitch motion to increase the seakeeping behavior. A new design concept, the interceptor diffuser, has the potential to do so.

1.1.3. Development of solution: interceptor diffuser

The interceptor-diffuser is a combination of a hull change and an appendage, as shown in figure 1.3. The stern is rounded, and the interceptor plate is placed at the same place as the conventional interceptor. Figure 1.4 shows the system in detail.

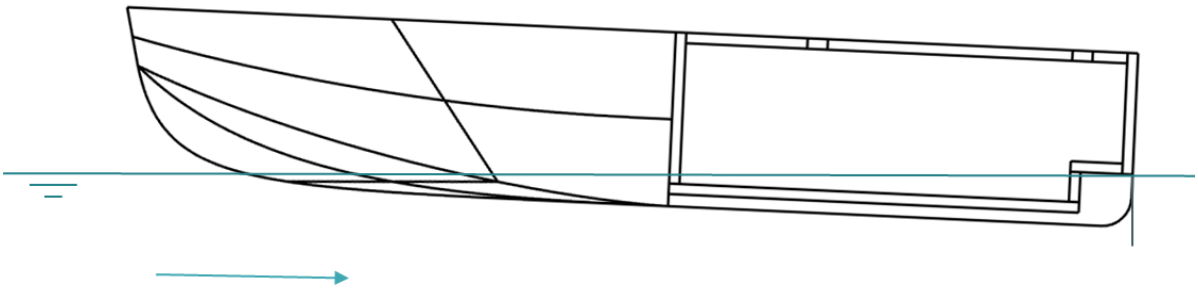

Figure 1.3: Fast ships' model with interceptor diffuser

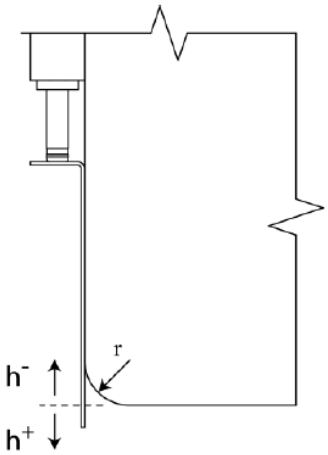

Figure 1.4: New interceptor configuration Rijkens et al. [2013]

The interceptor diffuser has proven in an experimental setup and 2D+t simulations with input from the experiments to create a positive lift comparable to the conventional interceptor and also a negative lift (Rijkens et al. [2013]). Details of this research are discussed in the next chapter. A negative deflection of the plate (h-) creates a negative lift. The stern shape works as a diffuser that accelerates the flow before the curve, and as a result, low pressure is created. The resulting negative lift creates a moment that trims the bow up. A positive deflection (h+) creates a positive lift which will trim the bow down. In front of the interceptor plate, the flow will stagnate, and higher pressure is created. The range of lift that can be created is increased compared to the conventional interceptor and sequential the influence on the pitch motion, which is beneficial for the seakeeping behavior. Since the previous study is only a proof of concept at model scale, the interceptor diffuser needs further research to be finally implemented in a design.

1.2. Project description

1.2.1. Aim of the project

The project aims to contribute to the development of the interceptor diffuser in three ways: by creating an understanding of the flow behavior under a diffuser stern, by making a first step in the design improvement, and by creating validation data for a numerical optimization study. The interceptor plate is left out of scope, so only the diffuser stern is studied. This is done because the positive lift was found to be very similar to a conventional interceptor, and the flow behavior of the conventional interceptor has already been studied with both numerical methods and PIV experiments. The knowledge gap exists in the flow behavior around the diffuser stern and the resulting negative lift.

The main goal of this research is to get an understanding of the flow behavior under the diffuser stern. This will be done by performing PIV (particle image velocimetry) experiments that capture the flow field under the diffuser stern in a model scale experiment. Specifically, the flow acceleration induced by the diffuser stern and the flow detachment are of interest. At the same time, the lift and drag forces of the ship model are measured.

Testing an improved design in the model experiments that increases the negative lift force would accomplish two goals at once. Therefore a CFD pre-study is performed by Damen Shipyards to make this first design improvement. The pre-study resulted in a newly designed shape and the implementation of side plates. The new shape is a circular rounded 70 mm stern starting 50 mm from the stern. Side plates with a height of 20 mm will be added with the aim to reduce the sideward flow at the sides of the model and thereby increase the negative lift force.

Since a CFD study is performed and model experiments with force and PIV measurements will be performed, it is possible to compare the found forces and the flow characteristics. Comparing the results has the aim of validating the CFD code for this specific application. The case of the rounded stern is particular because it involves a turbulent flow that is expected to separate from the round shape, and it is a two-phase flow. No validated numerical study is found for a comparable case. The wish for future development is to optimize the rounded shape of the stern to further increase the range of lift forces that can be created. Optimizing a shape is not possible by performing model experiments since changing the shape is time-consuming. Numerical methods are commonly used for shape optimizations in hydrodynamic designs. In order to use numerical methods for optimization, validation data is required to find a valid method for the optimization.

An extensive explanation of the steps leading to the choices for the experiments is given in chapter 2.

1.2.2. Research questions

The aim of this research to contribute to the development of the interceptor diffuser has lead to the following research questions.

1. What is the influence of the following factors on the lift created by a fast ship's diffuser stern?

- Stern radius
- Velocity
- Trim angle
- Side plates

- Pitch oscillations

2. What is the influence of the flow acceleration and the flow detachment point on the lift?

3. Does the numerical method used for the pre-study suffice for the use in an optimization study of the interceptor diffuser?

1.3. Report structure

The next chapter gives an extended explanation of the steps leading to the PIV experiments. It details the previous study about the interceptor diffuser and the knowledge gap that this study aims to fill.

Then, for readers unfamiliar with PIV, it is recommended to read the introduction into PIV experiments in appendix A. The steps in PIV experiments are introduced and the state of the art of PIV experiments in towing tanks is presented. For the literature background of fluid dynamics in a boundary layer, appendix B was added. This appendix introduces the fundamental fluid dynamics, including boundary layer theory of a turbulent flow and the determination of flow separation.

The performed PIV experiments are described in chapter 3. It includes the test program, design of the setup and the data processing. The last section is devoted to the evaluating of the PIV experiments. The results are split into three parts related to the three research questions: chapter 4 on the results of varying velocity, trim angle, shapes and side plates, and oscillations, chapter 5 on the effect of flow acceleration and detachment, and chapter 6 on the comparison with CFD results. In chapter 7 the conclusions are drawn. Further recommendations are made in chapter 8.

2

Steps leading to the performed experiments

The proof of concept of the interceptor diffuser by Rijkens et al. [2013] was the starting point for this research. Therefore the most relevant results are presented in this chapter, and steps for further development are discussed. As stated in the introduction, this research aims to contribute to the development of the interceptor diffuser by creating an understanding of the flow behavior at a diffuser stern, making a first step in the design improvement, and creating validation data for a numerical optimization study. Section 2.2 elaborates on the reasons for the chosen contributions and what they will add to the existing knowledge. In preparation for the experiments, a CFD study is performed by Damen Shipyards. In section 2.3, the code and settings of the pre-study are described, and the results are presented. The conclusion of this chapter in section 2.4 summarizes the findings presented in this chapter.

2.1. Previous interceptor diffuser study

This section gives a short description of the proof of concept study from Rijkens et al. [2013]. The knowledge gap regarding the interceptor diffuser is described.

2.1.1. Summary and discussion of the previous study

Model scale experiments with the interceptor diffuser have been carried out in the TU Delft towing tank by Rijkens et al. [2013]. The aim was to find the lift and drag coefficients for two stern radii: 25 and 50 mm relative to a straight stern for a general planing ship model with a length of 1.75 m ($L_w l = 1.52m$). The lift and drag forces are compared to a stern without an appendage and to a conventional interceptor. The height of the interceptor plate was varied. The velocity was varied from 3 to 5 m/s, and the trim angle between 3 and 6 degrees. The model itself was fixed in all situations, and the lift and drag forces were measured. The measured lift and drag forces were converted to non-dimensional coefficients.

Figure 2.1a shows the stationary results of lift coefficients, and figure 2.1b the drag coefficients. In these figures, the differences between the different stern shapes become clear. (The varying velocity and trim angle results are shown in figures C.1 and C.2 in the appendix.)

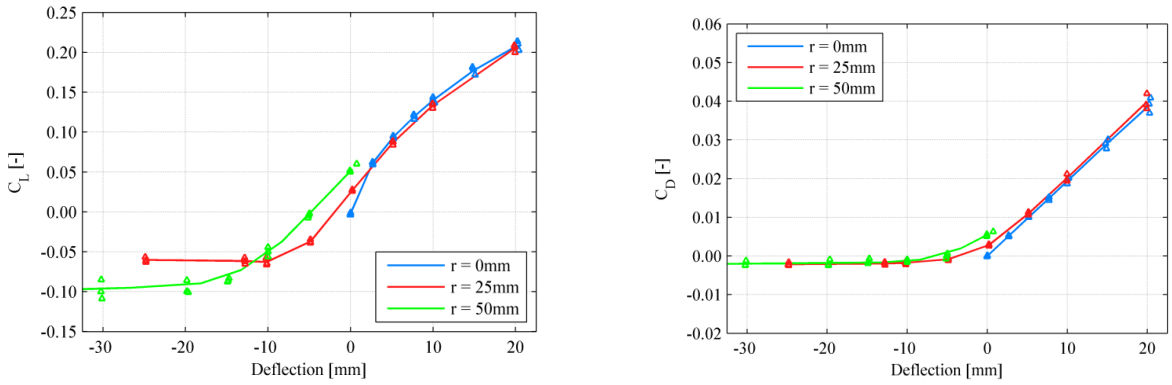

(a) Lift coefficient (b) Drag coefficient

Figure 2.1: Results of model experiments with different stern radii Rijkens et al. [2013]

The results show that the large radius of 50 mm creates a larger negative lift. The maximum negative lift ($C_L = -0.1$) is about half the amount of the maximum positive lift ($C_L = 0.2$). Knowing that the positive force created by a conventional interceptor is big enough to create a moment that changes the trim, it is reasoned that the negative lift is also big enough to create a trimming moment causing the bow to trim upwards. What can be concluded about the effect of the trim angle is that a higher trim angle leads to a slightly higher negative lift coefficient and a higher negative drag. The lift coefficient decreases with increasing the velocity, but in absolute values, the lift increases. The dynamic behavior during oscillations of the plate is close to quasi-static. At higher frequencies, there is a deviation. However, this is considered less important because motions at the highest frequencies will be small.

The lift and drag forces from the experiment were implemented in a 2D+t code called Fastship, validated for the motion prediction of fast ships in head-waves. This simulation shows that the vertical peak accelerations were reduced. Figure 2.2 shows the resulting probability of the exceedance of vertical peak accelerations at the bow. The conclusion is that the probability is decreased compared to a benchmark and conventional interceptor.

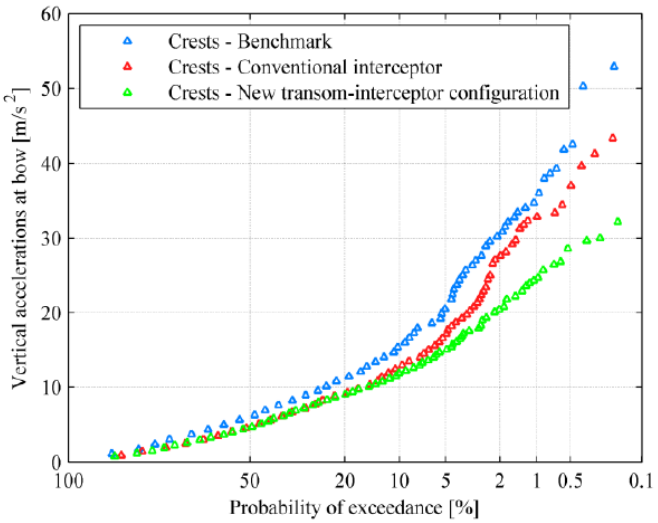

Figure 2.2: Probability of exceedance vertical peak acceleration from 2D+t simulations in Fastship (Rijkens et al. [2013])

2.1.2. Further development of the interceptor diffuser

An improvement of the interceptor-diffuser that can be made is to increase the negative lift by optimizing the stern shape. An increased lift capacity, so a wider range of lift forces, will improve the ability to influence the trim angle, and with that, the effect on the ride-control in head waves will be improved.

Noticeable is that for both radii, the negative lift reaches an asymptote (figure 2.1). For higher velocities, this asymptote is reached at a smaller deflection. An explanation for this effect could be that this is caused by early flow detachment from the stern so that the flow does not encounter the interceptor plate anymore. This asymptote has to be shifted to increase the negative lift, and therefore it is necessary to study the behavior of the flow.

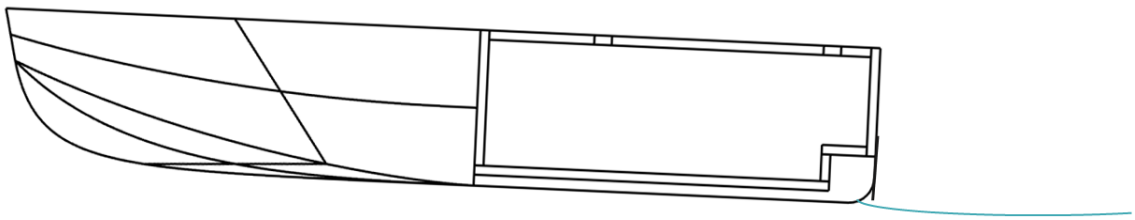

Figure 2.3: Hypothetical flow causing the asymptote in lift coefficient

In the oscillatory tests, an unstable condition was found at the highest tested frequencies. This unstable can be seen most clearly in figure C.3 in the graph for 2 Hz for negative deflections. Here the interceptor plate has oscillated. Since the plate and the ship will be oscillating, the question arises of the influence of the ship's motions on the lift. An instability is undesirable because it makes the created lift unpredictable.

The last suggestion is related to the wish to optimize the stern shape. A numerical method should be found that can predict the flow around the diffuser stern.

2.2. Contribution to the development of the interceptor diffuser

The first way to contribute to the development of the interceptor diffuser is by creating an understanding of the flow behavior. This will be done by observing the flow with particle image velocimetry. Subsection 2.2.1 is devoted to the choice for PIV and what could be observed in measurements. The focus of the study is set after analyzing the hydrodynamic case. In subsection 2.2.2, it is explained how this study contributes by making a first step in the design improvement by elaborating on the thoughts behind the improvement. The last contribution, the creation of validation data, is discussed in subsection 2.2.3. The importance of validation data is explained, and it is determined what will be compared between the experiments and CFD data.

2.2.1. Understanding the flow behavior

Motivated choice for method: PIV

Particle image velocimetry is chosen because a flow field can be captured in model experiments. Water can be made visible with seeding particles that do not disturb the flow. The flow can then be captured by illuminating the particles with a laser. Two different methods use this principle: Particle tracking velocimetry (PTV) and Particle Image velocimetry (PIV). With PTV, the particles are tracked, and streamlines can be obtained. The velocity field and pressure field can be derived from the data. PIV can capture instantaneous flow structures with an interrogation between two images of the particles.

A velocity field can be obtained from these images, and a pressure field and Reynolds stresses can be derived. Differences are that PTV has a lower seeding density, and the results are in a Lagrangian coordinate system. In contrast, PIV has a high seeding density, and the coordinate system is Eulerian. With the PIV system of the towing tank at the TU Delft, it will be possible to obtain the flow field at a high resolution, and the flow detachment will be observed.

Common methods for experimental fluid dynamics are Laser Doppler Anemometer (LDA) and Hot Wire Anemometer (HWA). However, these are point measurements not able to capture a field. Furthermore, HWA is not applicable in a towing tank, and pressure tabs are inaccurate at high velocities.

Numerical methods could also be an outcome in determining a flow field. However, for this specific case, it is questionable whether a numerical method gives a reliable outcome. Subsection 2.2.3 elaborates why this is the case and why it is chosen not fully to perform this study numerically.

Diffuser stern reduced to a hydrodynamic case

It is defined what is important to observe in the PIV measurements by looking at the factors influencing the negative lift force. Therefore the model with a diffuser stern is reduced to a hydrodynamic case. The situation can be reduced to a uniform flow under the model that tries to follow the curved stern, shown in figure 2.4. The following boundary conditions apply; no slip at the model's surface, no penetration through the model surface, and the free surface is a line of constant pressure. The water is considered to be incompressible.

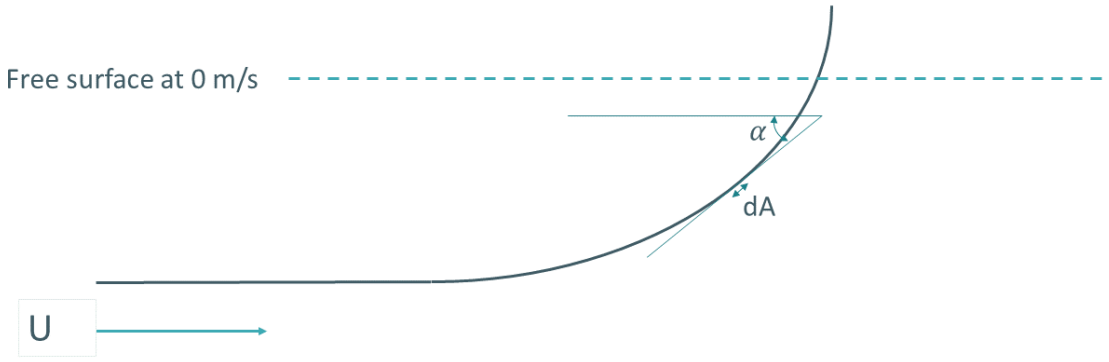

Figure 2.4: Simplified hydrodynamic problem

The diffuser stern creates an accelerated flow. The increased velocity in this area creates an underpressure. Examples of experimental and numerical studies that confirm this effect are discussed in appendix B.3. The pressure distribution is of interest because the lift force (F_L) can be determined by integrating the pressure (p) over an area (A). The angle α is the angle between the surface and the horizontal plane. The pressure scales with the velocity squared and the area with the attachment length.

$$F_L = \int pd(A \cdot cos(\alpha)) \tag{2.1}$$

The Navier Stokes equation has in this application three important terms: the pressure gradient, the viscous term, and the force term z-direction. Since these are important terms, the two dimensionless parameters, Reynolds number and Froude number are relevant. The order of the Reynolds number is estimated using the water density of the towing tank $\rho \sim 10^3 kg/m^3$, dynamic viscosity $\mu \sim 10^{-3} Ns/m^2$ and length scale $D \sim 1m$. A Reynolds number in this order of magnitude implies a turbulent flow (Kundu et al. [2016]).

$$Re = \frac{\rho V D}{\mu} \sim \frac{10^3 10^0 10^0}{10^{-3}} \sim 10^6[-] \tag{2.2}$$

The Froude number is calculated exactly because an estimation can lead to a wrong conclusion about whether the model is in its planing region or not. The lowest taken velocity is $v_m = 3m/s$ and the highest $v_m = 5m/s$. The length of the waterline of the model is $L_{wlm} = 1.52m$. This results in the range of Froude numbers between $Fn = 0.78[-]$ and $Fn = 1.29[-]$. A Froude number above one is often considered a planing condition (Faltinsen [2005]). Hence, the calculated values imply that the model is at the higher side of the velocity range in its planning region.

$$Fn = \frac{U}{\sqrt{gL}} = 0.78[-] - 1.29[-] \tag{2.3}$$

Hypothesis

What could be expected is that the flow will detach from the rounded stern. A distinction between flow separation and detachment is made here. Figure 2.5 shows a situation where flow separation occurs, and a re-circulating flow appears behind the separation point. The principle of flow separation is explained in appendix B.3. Figure 2.6 shows a situation where the flow can follow the curve and detaches at a certain point. It is the point where the free-surface ends on the model.

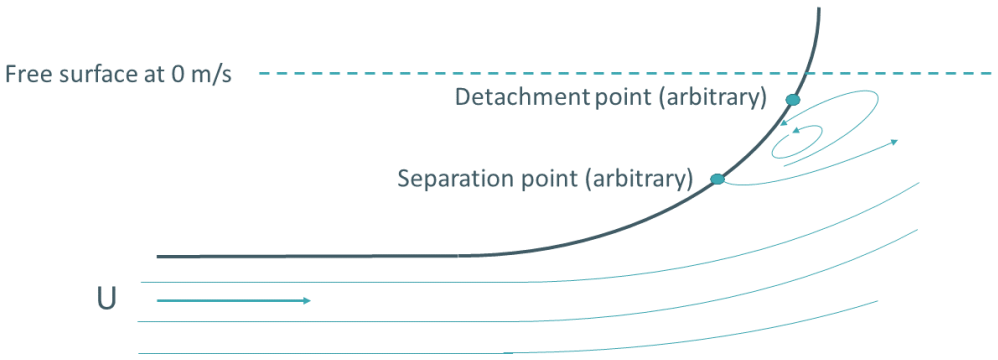

Figure 2.5: Flow separation and detachment

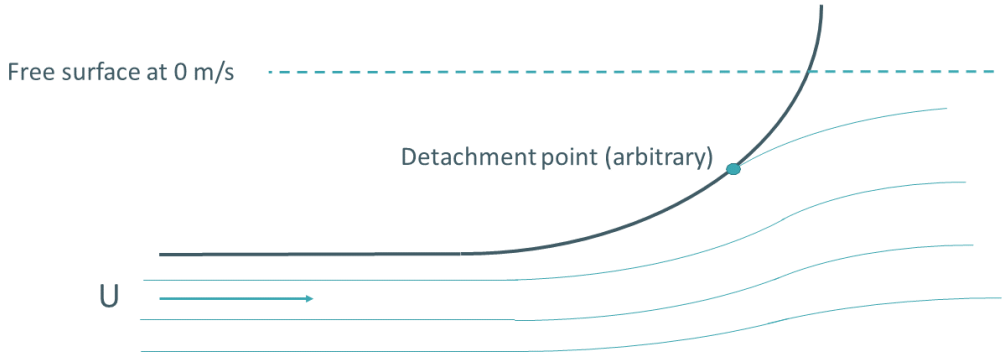

Figure 2.6: Flow detachment

Note that the streamlines, separation point, and detachment point are chosen arbitrarily. Flow separation is expected to happen at very low velocities, if the model has a very large draft, and with stern shapes with a small radius of curvature that cause a strong adverse pressure gradient. In a model experiment as performed by Rijkens et al. [2013], flow detachment is expected. If separation occurred, that would be disadvantageous for the negative lift because there is a high pressure in the recirculation area. This detachment point depends mainly on the velocity of the ship, the viscosity of the fluid, and the shape of the stern. The hypothesis is that the highest negative lift will be created in a situation with the latest detachment. Late flow detachment means that the area with a lower pressure is increased.

What to observe in the flow field

The focus of this study is on the acceleration of the flow and the flow detachment point. The flow accelerations affect the pressure, and the flow detachment point affects the area. Both are considered important factors to influence the negative lift.

2.2.2. Design improvement

Another contribution to the development while performing the experiments can be made by trying to make a first improvement in the design to increase the negative lift. The previous study found that a larger stern radius creates a larger negative lift force. If this trend continues, a larger stern radius will lead to an even larger negative lift. However, a limit is expected because a huge radius will look like the straight stern again. For the used model with a wetted length of 1.52 m, the optimum stern radius is expected to be 50 mm or larger. Therefore different stern radii are tested in the CFD study, which results are shown in section 2.3.

A design improvement that has proven its potential for the conventional interceptor is the use of side plates. In the case of the conventional interceptor, the side plates reduce the sideward flow and increase the pressure in front of the interceptor plate. The opposite effect could be obtained when the side plates are put on the sides of the diffuser stern. The side plates would prevent the flow from going from the side under the bottom, which would decrease the pressure under the stern. Different side plate designs are tested in the CFD study.

2.2.3. Creating validation data

The data obtained from PIV experiments in combination with force measurement will be used as validation data. For an optimization study, it is important to have validated numerical results to trust the outcome. The most commonly used numerical methods applied in ship hydromechanics can be categorized in BEM, RANS, and LES methods. A BEM (boundary element method) is unsuitable for applying a diffuser stern because viscosity is neglected. Nevertheless, viscosity is an important factor that will influence the lift. A BEM code can be used to calculate pressure coefficients as input for a method to calculate the flow separation point with an analytical method described in appendix section B.3.

RANS (Reynolds averaged Navier Stokes) models do take into account the viscosity. A common way to implement the viscosity in a RANS model is to replace the six Reynolds stresses with one added viscosity term. However, the six Reynolds stresses may be independent and all-important because they are necessary to calculate the shear stress. The shear stress is, in its turn, important for the determination of flow separation. Another drawback of RANS models is that they use finite volume or finite elements, so the quality of results depends on the mesh size. Accurate results require small meshes and can be very expensive in time and costs.

LES (large eddy simulation) is more expensive in terms of time and costs. These are also, so far found in literature, not validated for cases with flow separation from a rounded solid close to a free surface.

The diffuser stern is a particular case. It involves a free-surface, the flow is turbulent, and separation of detachment will occur from the rounded stern. Appendix B.3 shows several studies that predict flow separation. Most are also for a turbulent flow. However, none of them involve a free-surface.

PIV has the advantage over numerical methods that the results take into account all physical effects, and the uncertainty is known. For applying a numerical method to optimize the diffuser stern, the most important question is whether the method can predict the flow detachment. Especially because the flow detachment or separation is important for the resulting negative lift.

2.3. CFD pre-study

Damen Shipyards provided the CFD pre-study. The aim was to make a first step in the design improvement to select designs for the experimental study. Furthermore, the results of this pre-study will be validated with the experimental PIV data to see whether the code is suitable for an optimization study. This is important because, as explained in the previous section, it is questionable whether a CFD code can predict the detachment point and flow acceleration. This section will explain what code and what input is used for the CFD study. Also, the results are discussed.

2.3.1. Used code and input

The numerical study is performed with the CFD code FINE/marine v9.1. A RANS model with a wall resolved approach was used. This means that the velocity profile in the boundary layer is not estimated as a logarithmic profile but solved in the model. This is done because applying the logarithmic wall function resulted in forces significantly differing from the forces measured in the experiment of Rijkens et al. [2013]. The inaccuracy of the found flow separation point is a possible explanation for the differences.

Figure 2.7 shows the grid with a refinement close to the hull and the free surface.

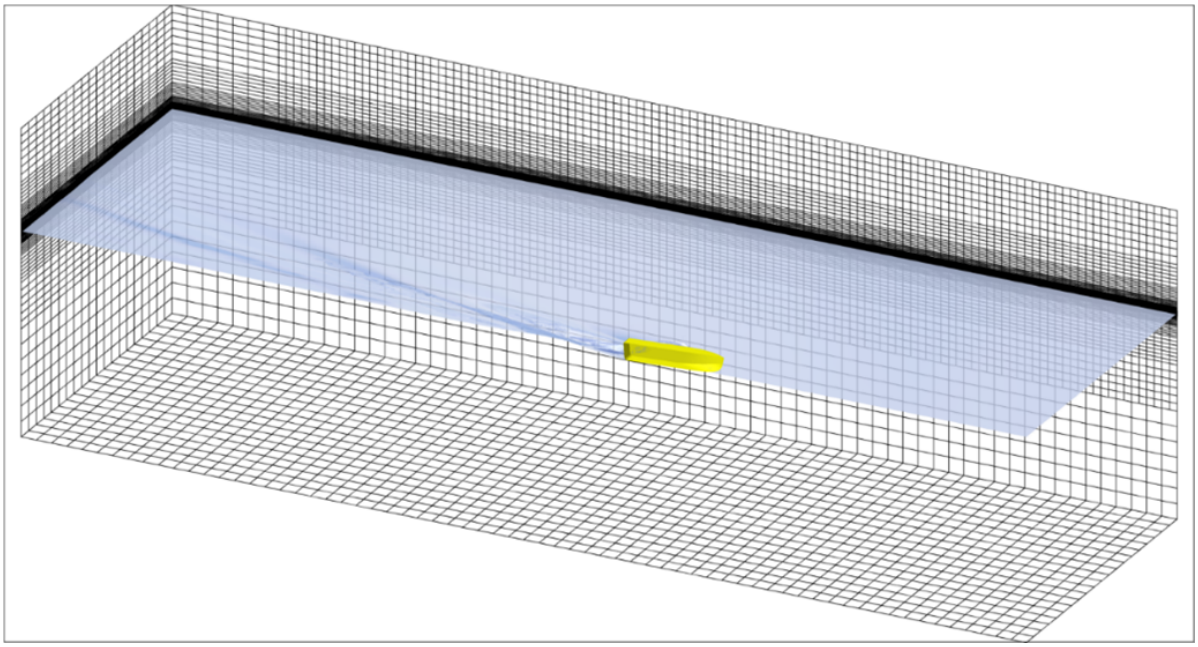

Figure 2.7: Grid of CFD

A grid convergence study was performed for the field under the rounded part of the stern. The size of the grid parallel to the hull was kept constant, and the size orthogonal to the hull was refined with a factor of 2. The refinement was done three times, so four different meshes were tested, which are shown in figure 2.8

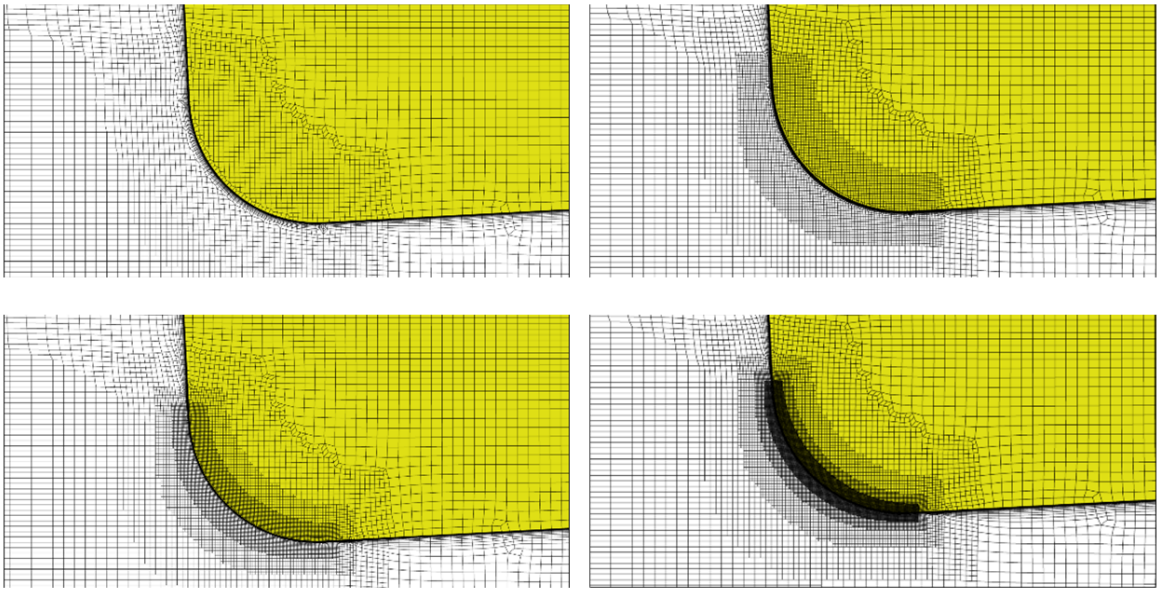

Figure 2.8: Grid refinement in the rounded stern area

A grid refinement showed a decrease in the negative lift coefficient and an increase in the drag coefficient. So the drag increased. However, the results did not converge yet. It means that a smaller grid size is necessary to find a more accurate result. A finer grid leads to a larger lift force, so a smaller

negative lift coefficient.

Four different stern shapes were tested: the straight stern, a radius of 50 mm, 60 mm, and 70 mm. Two different types of side-plates were implemented in the code. The first type covered the shape of the straight stern and the second type had a height of 2 cm over the whole stern shape.

2.3.2. Results and data processing

The increase of the stern radius showed an increase in the negative lift coefficient. The longest attachment was found for the 70 mm stern. However, the lowest pressure was found under the stern of 60 mm. This means that not simply the flow velocity or attachment length is important, but both determine the resulting lift. For the experiment, a limited number of shapes can be tested. This lead to the choice to test the straight stern as a reference, the radius of 50 to compare with previous experiments, and the radius of 70 mm that gave the highest negative lift coefficient.

Considering the side plates, the 20 mm height design is chosen to test during the experiments. The effect of the reference-shaped side plates was negligible. The larger side plates showed a negative effect, so a decrease of negative lift. The reason for the increased pressure could not be found, but an experimental result could clarify this.

The CFD data is delivered as point data in an unstructured grid. For each point, the velocity vector and mass fraction are known. A location on the hull is chosen, and data points orthogonal to the hull are determined. MATLAB's scatteredInterpolant function is used to find the velocity in all directions for the determined data points. The velocity parallel to the hull is calculated, and this results in the boundary layer velocity profile.

The flow separation point is determined by using the mass fraction along the hull. The point where the mass fraction is 0.5 is considered as the flow detachment point. From this location, the angle on the rounded part can be determined.

2.4. Conclusion

The gap of knowledge about the interceptor diffuser lies in the diffuser function of the stern. The diffuser stern can create a negative lift relative to a straight stern, but the flow behavior is difficult to predict. No validated analytical or numerical method is found for a case like the particular diffuser stern. Therefore it is chosen to perform PIV experiments. It is important to look at the flow acceleration and detachment in these experiments because those determine the negative lift. In preparation for the experiment, the CFD study performed by Damen gave two possible design improvements to test: the stern radius of 70 mm and side plates of 20 mm height. The results of this study will also be validated with the PIV data to check whether the code suffices for an optimization study of the interceptor diffuser.

3

PIV experiments

To find the answer to the asked research questions, PIV experiments are performed. The experiment is designed to obtain the flow field under the diffuser stern and measure the lift and drag forces. The test program is described in section 3.1. The designed setup and components are shown in section 3.2. Also, considerations about the setup design are discussed. Section 3.3 is devoted to data processing of the PIV and force data. Lastly, the performed experiments are evaluated, and important conclusions are drawn for what is included in the results.

3.1. Test program and substantiation

Table 3.1 shows the variables in the test program, which will be substantiated in this section. This set allows finding the effect of the stern shape, velocity, trim angle, side plates, and forced pitch oscillations. Certain combinations are left out to reduce the number of runs needed.

Table 3.1: PIV experiment variables

Variable (symbol)	Parameters	Unit
Shape: stern radius (r)	0 (reference: straight stern) , 50, 70	[mm]
Model speed (Vm)	3 , 4 , 5	[m/s]
Trim angle (θ)	3 , 6	[deg]
Oscillation frequency (f)	0.25, 0.5, 1, 1.51, 2	[Hz]
Oscillation pitch motion range	3-6	[deg]
Side plates	With , without	[-]
Measurement plane distance from the side	200 = centreline, 30	[mm]

3.1.1. Stern shapes and side plates

The three different stern shapes: a straight stern, a transom with a radius of 50 mm, and a transom with a radius of 70 mm that starts at 50 mm from the transom, are shown in figure 3.1. The 70 mm radius starts 50 mm from the transom to see the effect of the curvature without changing the hull length.

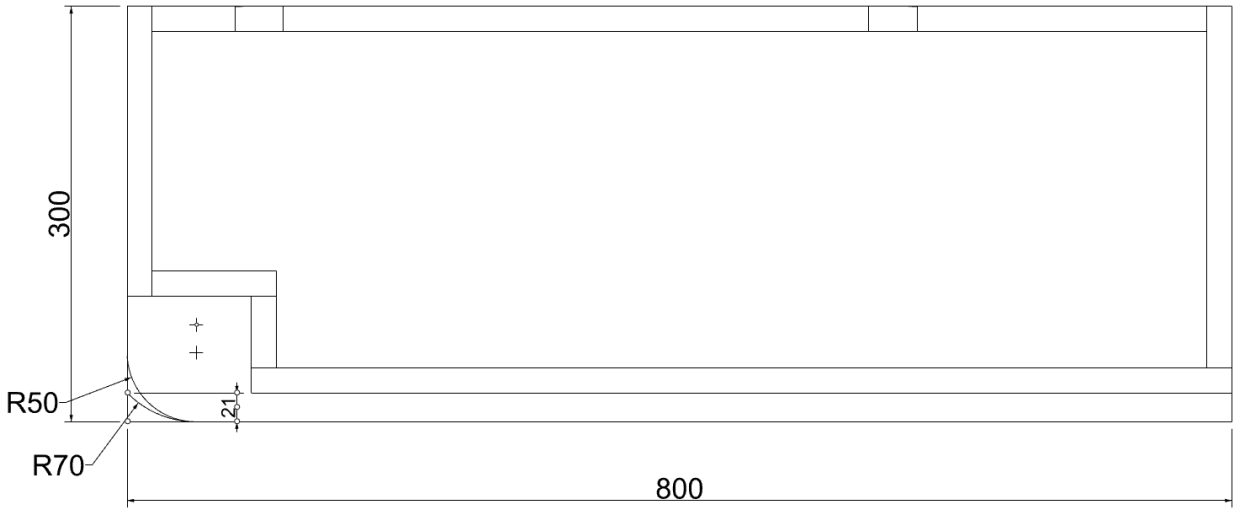

Figure 3.1: Stern shapes

The bottom part of the model is changeable to test multiple shapes with the same ship model. Because the transition from the model to the changeable part is located 800 mm from the stern, the effect of an eventual flow disturbance on the diffuser transom flow is minimized. The straight stern is used as a reference for the measured lift and drag force and the flow behavior obtained with PIV measurements. With the reference forces of the straight stern, the relative lift of the rounded shapes can be compared with previously performed experiments by Rijkens et al. [2013] by calculating the lift and drag coefficient.

Figures 3.2 and 3.3 show the dimensions of the side plates. The thickness is 2 mm.

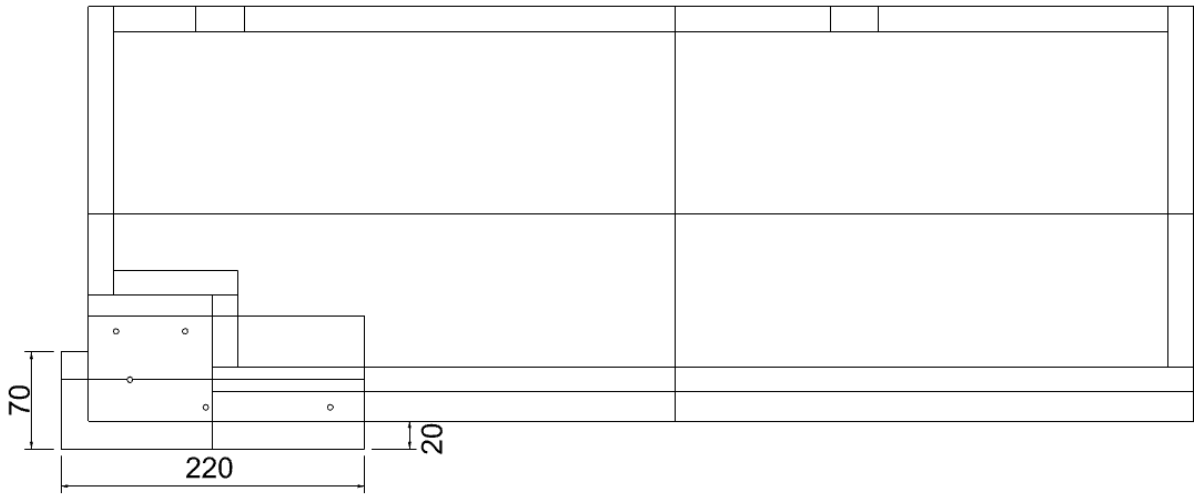

Figure 3.2: Side plate for the straight stern

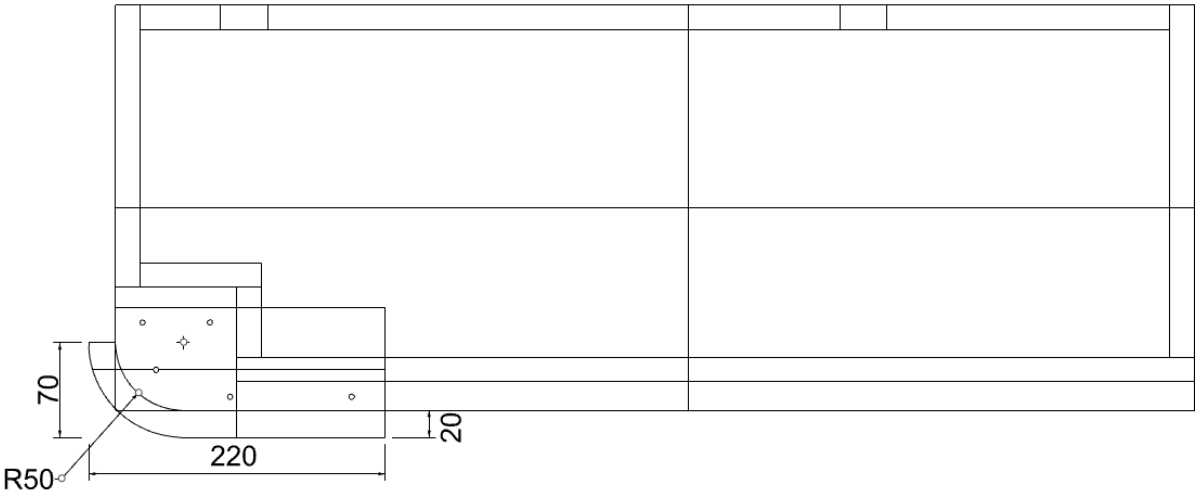

Figure 3.3: Side plate for the r=50 mm stern

3.1.2. Velocities and trim angles

For all configurations, a set of four conditions is tested. The trim angle of 6 degrees is only tested at a velocity of 4 m/s, and for the trim angle of 3 degrees, the velocity is varied from 3 to 5 m/s. The four standard test conditions are presented in table 3.2.

Table 3.2: Four standard test conditions

Model velocity v_m [m/s]	Trim angle θ [deg]
3	3
4	3
5	3
4	6

3.1.3. Measurement planes

For all configurations, the plane in the centreline is measured because there a two-dimensional flow is expected. To see a 3D effect, a plane 30 mm from the side is also measured for all stationary cases. This also allows seeing the effect of the side plate on the out-of-plane velocity that can be found with a stereo PIV setup. A distance of 30 mm is taken because the setup does not allow to displace the model further to the side than 170 mm.

3.1.4. Pitch oscillations

Since the interceptor diffuser is designed to reduce vertical accelerations when sailing in waves, a calm water test does not represent the behavior in waves. Stationary tests are necessary to look solely at the effect on the flow behavior and the resulting lift and drag. However, there is also interest in the effect of motions on the lift and flow behavior. Forced pitch motions are chosen to simulate the effect of encountering waves.

The pitch motion is performed between trim angles of 3 and 6 degrees at frequencies of 0.25, 0.5, 1, 1.51, and 2 Hz. The center of rotation is located 800 mm from the stern and 50 mm from

the keel line. The range of pitch angles is chosen so that the static runs are the reference. For the higher frequencies, the question is whether the lift will follow the sinusoidal motion, so whether the lift is predictable. The higher frequencies are chosen because they are comparable with encounter frequencies when sailing in head waves. These are calculated using full-scale reference ships and a JONSWAP spectrum representative for the North Sea. The model is not specified for one ship type, but it is a basic planing ship model. The scaling of the velocity and frequency are dependent on the full-scale ship. Therefore, five ships with their operational speeds are taken to find representative velocities and frequencies at model scale. The five chosen models are an ESC (enlarged ship concept), DAMEN ABC (axe bow concept), a SAR (search and rescue vessel), Interceptor, and a RIB (rigid inflatable boat) shown in table 3.3.

Table 3.3: Chosen fast ships for encounter frequency reference

Ship type	**Length**	**Speed**
ESC (enlarged ship concept)	Lwl = 55 m	25 knts, 35 knts, 50 knts
ABC (axe bow concept)	Lwl = 55 m	25 knts, 35 knts, 50 knts
SAR (search and rescue) 1906	Loa = 19.5 m	Up to 30 knts
Interceptor	Loa = 11-32 m	45-55 knts
RIB	Loa = 7.5-11 m	40-50 knts

A JONSWAP spectrum with a significant wave height of 1.25 m and a peak period of 6.5 seconds is taken. The encounter frequency (ω_e) is determined for ship velocities (v_s) of 25, 35 and 50 knots. The encounter frequency with the highest energy is translated to a frequency in model scale for all chosen ship lengths with the scaling factor λ. The scaling factor is the model length divided by the full-scale length. The resulting frequencies are presented in table 3.4. Not all combinations of velocities and frequencies occur, so the relevant values are determined with the Froude number and underlined in the table.

$$\omega_e = v_s \cdot \omega - v_s \cdot \frac{\omega^2}{g} \cdot cos(\mu) \tag{3.1}$$

$$f_{model} = \frac{f_{fullscale}}{(\lambda)^{0.5}} \tag{3.2}$$

Table 3.4: Encounter frequencies [Hz] for peak energy in model scale

Velocity [knts] \ **Length [m]**	**11**	**19.5**	**32**	**55**
25	0.86	1.14	1.46	1.91
35	1.05	1.39	1.79	2.34
50	1.33	1.78	2.27	2.98

The drawback of testing at high frequencies is that force sensors with a larger capacity must be taken. Therefore it is chosen to take a maximum pitch oscillation frequency of 2 Hz. Also, very low frequencies of 0.25 and 0.5 Hz are tested because a quasi-stationary result is expected, and 1 and 1.51 Hz as steps towards the highest frequency. 1.51 Hz may seem odd, but PIV images are taken with a frequency of 50 Hz, and a round number of images should fit in one oscillation to capture the flow at the same moment in the pitch oscillation. A frequency of 1.5152 Hz results in 33 pictures per oscillation.

3.2. Setup for PIV experiments

The setup is designed to obtain the flow field around the diffuser stern in a specified area with a stereo PIV system and measure the lift and drag forces. A side view of the final setup is shown in figure 3.4. The model is held by a hexapod which is used to change the trim angle of the model. Two long torpedos hold the PIV cameras, and the short torpedo guides the laser. The laser itself is placed on top of the strut. All struts are covered with wings to reduce the disturbance of the flow and splashing.

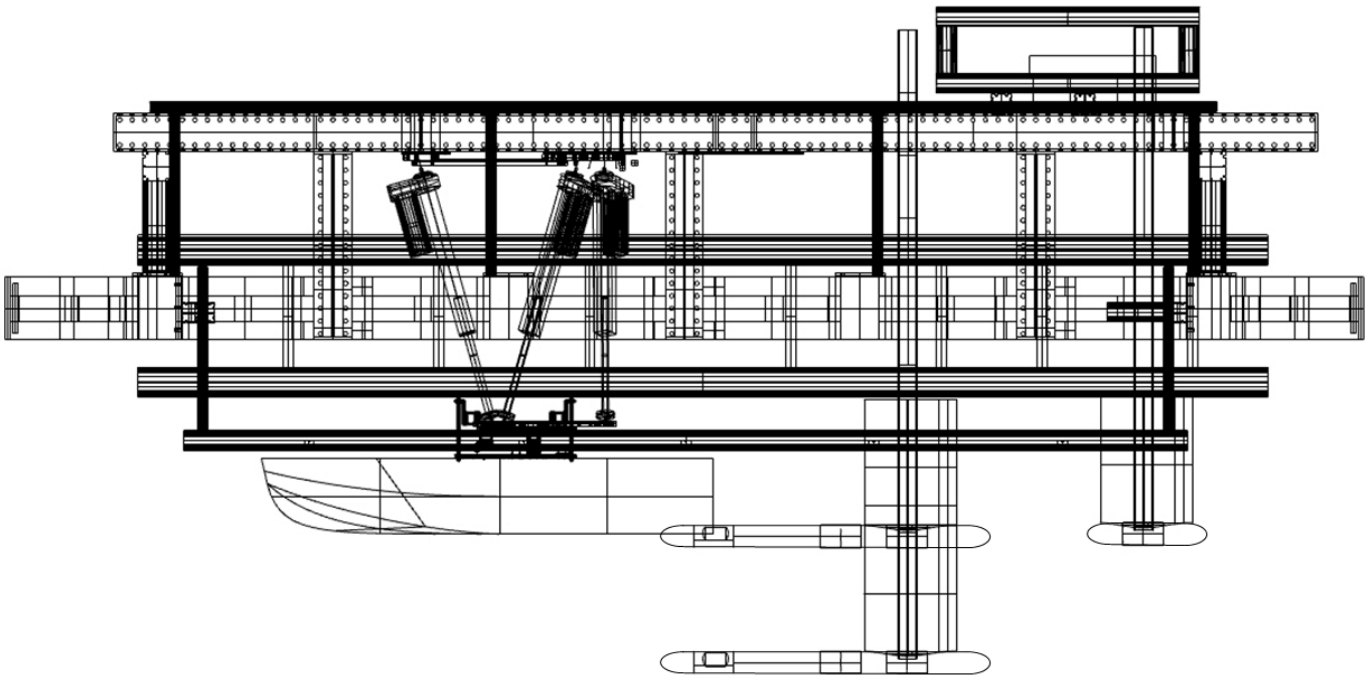

Figure 3.4: Setup side view

This setup makes it possible to capture the flow in a plane of 35 by 35 mm. Positioning the cameras and the laser was the main challenge in the design of the setup. The laser must be placed above or behind the model. For placing the laser above the model, the model bottom should be made from acrylic glass. Because the behavior of the laser sheet through curved acrylic glass is unknown, this option may have lead to a bad illumination of the particles. Therefore the laser was positioned behind the model.

The field of view is determined beforehand, using the camera specifications and locations and orientations to determine the right position of the cameras. The positions shown in table 3.5 lead to the views shown in figure 3.5. The field in the red square is the field of view. The dotted lines represent the side plates, and the dashed line is the centerline of the model. The locations in the table are defined relative to the center of the field of view.

Table 3.5: Camera positions and orientations

	Camera 1	Camera 2
X	0	0
Z	-250 mm	-600 mm
Y	950 mm	750 mm
Roll	10 deg	35 deg

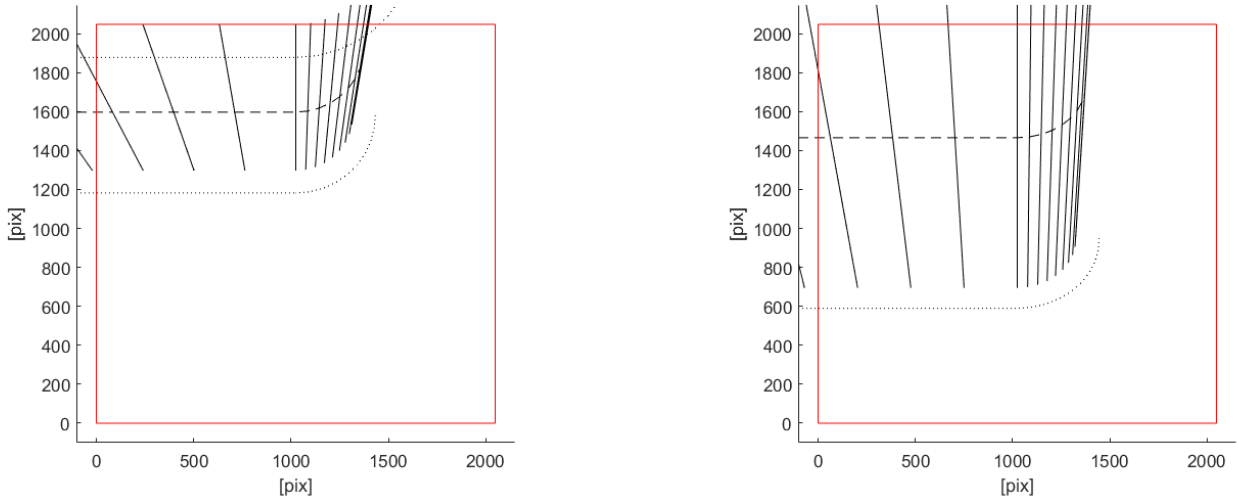

(a) Camera 1 (upper)

(b) Camera 2 (lower)

Figure 3.5: View of both PIV cameras

The image view was calculated by translating the world coordinates $[XYZ]$ to camera coordinates $[uv]$ with the location and orientation of the cameras are represented in the extrinsic matrix and the specifications of the camera represented in the intrinsics matrix. $[c_x, c_y]$ is the principle point used as image center and $[f_x, f_y]$ the focal lengths.

$$\begin{bmatrix} u \\ v \\ 1 \end{bmatrix} = [intrinsics][extrinsics] \begin{bmatrix} X \\ Y \\ X \\ 1 \end{bmatrix} \tag{3.3}$$

$$\begin{bmatrix} r_{11} & r_{12} & r_{13} & t_1 \\ r_{21} & r_{22} & r_{23} & t_2 \\ r_{31} & r_{32} & r_{33} & t_3 \end{bmatrix} \tag{3.4}$$

$$\begin{bmatrix} f_x & 0 & c_x \\ 0 & f_y & c_y \\ 0 & 0 & 1 \end{bmatrix} \tag{3.5}$$

An important factor for the quality of the results is the cross-correlation that can be found between one time step and the next. Between the two frames, the particles have to move far enough to see the

displacement but not too far to have enough same particles in the interrogation area. The time step can be calculated starting with a chosen velocity. The velocities of the model will be 3, 4, and $5m/s$. It is assumed that the maximum velocity of the flow is almost the same and the maximum distance that may be traveled in one time step is a quarter of an interrogation area. This leads to the maximum time steps of 244, 183, and $146\mu s$ if the size of an interrogation area is taken 24x24 pixels. However, the processing of the PIV data has improved. By starting with a larger interrogation area, an initial velocity vector is used to help to find the correlation in smaller interrogation areas. Therefore timesteps of 380, 285, and $228\mu s$ could be used. With the size of the field of view and the interrogation areas, the resolution of the vectors can be determined. Interrogation areas of 24x24 pixels and an overlap of 75% result in a vector each 7 mm.

Details of the towing tank, the model, the 6 degrees of freedom force measurement frame, a laser distance measurer, the PIV laser, the PIV cameras, and the seeding can be found in appendix D. Additional drawings from other views and a photo of the final setup can be found in the last section of this appendix.

3.3. Data processing

As defined in chapter 2, the focus of the experiments is on the negative lift force and the flow acceleration and detachment induced by the diffuser stern. The negative lift is obtained from the measured forces with processing steps explained in 3.3.2. With the obtained PIV images, several processing steps must be taken to obtain the resulting velocity field and flow detachment. In subsection 3.3.1 the pre-processing, processing and post-processing are explained. All processing steps are performed with MATLAB (R2019b) and DaVis (10.2.0.74211) Flowmaster.

3.3.1. PIV data

Pre-processing

In preparation for processing the PIV program DaVis, several steps must be taken to prepare the images. The model covered a part of the field of view. For processing the data, it is beneficial for the processing time to mask the model. Additionally, it is necessary to know the exact location of the model to determine the distance and orientation of a velocity vector relative to the model. Therefore the model has to be detected. The model is clearly visible for the runs with a straight stern and a trim angle of 3 degrees. When the same model has a trim angle of 6 degrees, the bottom is not visible because the stern blocks the laser light. For the rounded shapes, the curved part is clearly visible, but the bottom is not. Figures 3.6,3.7 and 3.8 show images that are the sum of all images over time, and both camera's images added up in world coordinates. The average position of the model is assumed to be the most intense line. The particles are not visible because it is the sum of all images in a run, and the particles move.

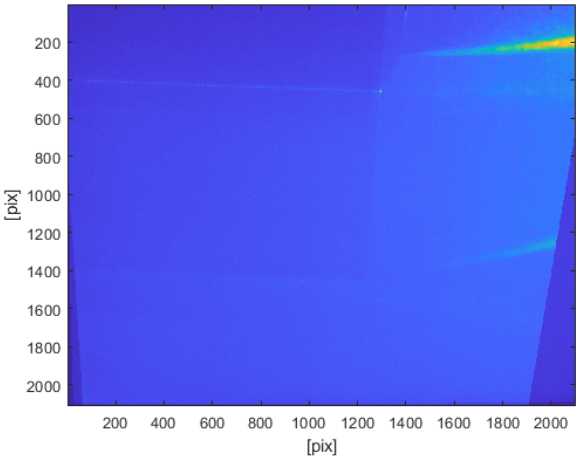

Figure 3.6: Sum image of cameras 1 and 2 in world coordinates for stern shape r=0

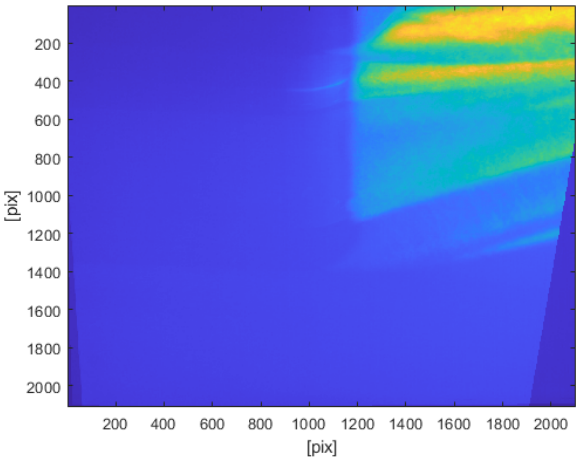

Figure 3.7: Sum image of cameras 1 and 2 in world coordinates for stern shape r=50

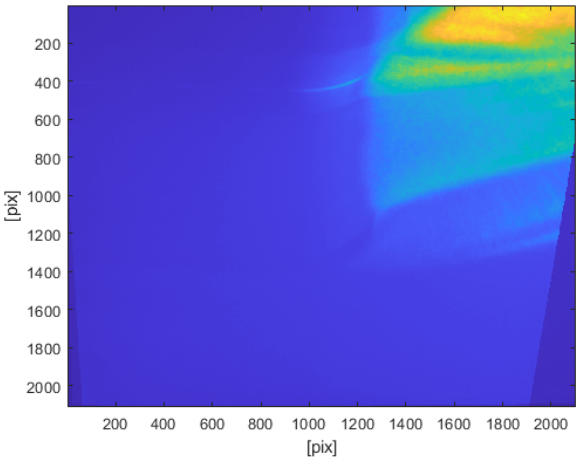

Figure 3.8: Sum image of cameras 1 and 2 in world coordinates for stern shape r=70

For the detection of the straight stern, two methods were used to define the mask. For the trim angle of 3 degrees, a bottom line is drawn through 2 points found by clicking on a plotted zoomed image. For the trim angle of 6 degrees, the corner is found by clicking in a zoomed-in image, and a line of 6 degrees is defined from there. The bottom of the figure is also masked because only a minimal velocity gradient is expected in the lowest part of the image. For 3 degrees, a cut-off height from pixel 1200 is chosen. Similarly, for the trim angle of 6 degrees, the image was cut off at pixel 1600. Due to the reflections behind the stern caused by the free surface, it was chosen to also cut off the part of the image behind the stern. Figure 3.9 shows an example of the mask. The part of the image in the red lines is what is leftover from the original images.

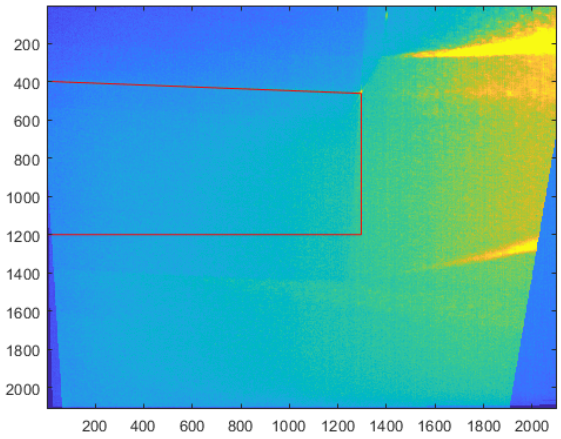

Figure 3.9: Example of the mask of r=0 stern shape

The rounded stern is detected by converting the sum image part with the rounded stern part to a binary image and afterward applying a least square root's detection. The binary image gives coordinates of the high-intensity pixels on the rounded stern. A circle with a fixed radius is varied in position, and the position with the least square root error related to the found coordinates is chosen as the position for the circle. Figure 3.10 shows the red small dots indicating the found coordinates in the binary images, the red circle indicating the found circle center, the yellow line indicating the mask, and the yellow star indicating the start of the straight bottom line.

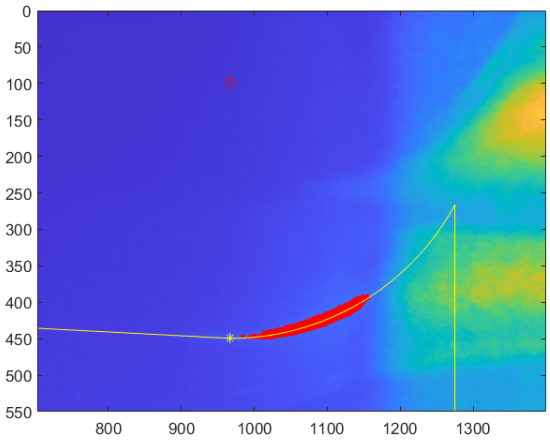

Figure 3.10: Example of least square circle detection

Because the bottom is not visible, a line is drawn with the given trim angle touching the circle. At last, the right side of the image is cut off at pixel 1275 because this is clearly after the free surface starts in all cases but before the end of the circular part of the model. This results in a mask shown in figure 3.11.

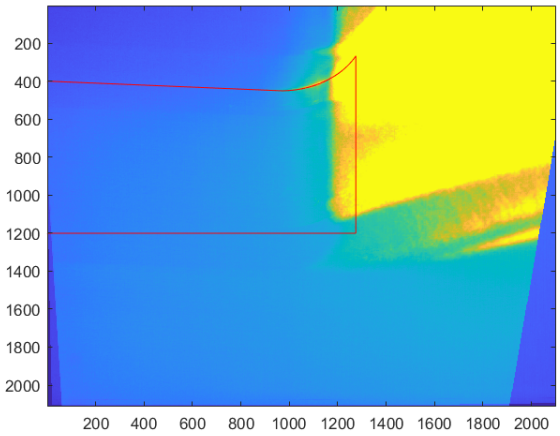

Figure 3.11: Intensity image with mask for stern r=50

Processing

Two different types of processing will be done. The first is only with camera 1, looking from the side, for planar PIV to find the 2D flow fields. This is done to eliminate the effects of reflection in camera 2, discussed in section 3.4.2. The second type is stereo PIV that gives 3 components of the velocity field in a 2D plane. This is used for obtaining the out-of-plane velocity to find the effect of the side plates.

An interrogation area size of 24x24 pixels and an overlap of 75% is used, which will result in a resolution of 7.01 mm for the velocity vectors. The program starts with interrogation areas of 64x64 to improve outlier detection. 500 sets of photos are taken, so 500 velocity fields are found. In some photo sets, there is no vector found in some interrogation areas. For the resulting velocity field, only if more than 50 vectors are found and only if the standard deviation is smaller than 2.

Post-processing

The result of the processing is a velocity field below the model. From the field, the boundary layer and its development will be found. This is done by setting a location on the model's edge and determining data points orthogonal to the hull from the chosen location. Here the masks play a role again in the location of the model. For these chosen boundary layer locations, the velocity parallel to the hull is calculated. The same applies to the uncertainty.

Flow detachment determination

The flow detachment point can be determined using the raw images in world coordinates. The intensity increases immensely when the free surface starts because it is reflecting the laser light. Figure 3.12 shows the method for determining the flow detachment point that is explained below.

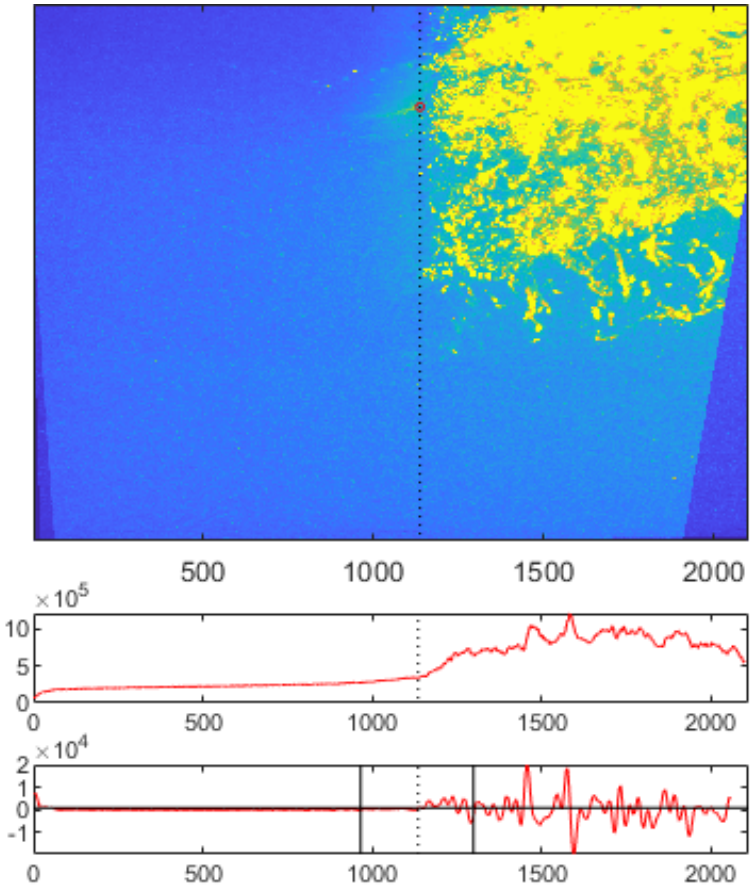

Figure 3.12: Method for finding flow detachment point: intensity image, sum of intensity, gradient of sum intensity

For each x-position, the intensities of all pixels in the y-direction are added up. The sum of the intensity counts is plotted in the middle graph. The gradient of the intensity sum is determined and plotted in the lowest graph. The location on the round part of the stern where the intensity increases is defined as the flow detachment point. The threshold that is chosen for the intensity gradient is 1000, indicated by the horizontal black line. The determined point must be located somewhere on the rounded stern, between the vertical black lines. The dotted black line indicated the found flow detachment point for this specific picture. For this detachment location, the angle relative to the start of the rounding and distance of attachment are calculated with the earlier defined mask.

The threshold is specifically for the images in this experimental setup because the intensity depends on many setup parts and settings. For example, the camera settings, the distance between the imaged particles and the laser, and the angle between the laser sheet and the free surface. The threshold is based on what is seen as the transition from water to air by the human eye. It may not be the exact point, but it seems to be a very accurate prediction in the results. The same threshold is applied in all detachment point determinations of this experiment. Therefore it is possible to compare the outcomes for different runs.

3.3.2. Force data

The force data consists of measurements during the runs, reference runs above the water, and reference runs in the design draft and trim angle. Parts of the data where the model was not in the right position at the right velocity were cut off. This is done by reading the laser distance measurement data

for the position and the measured velocity of the carriage. For the stationary runs, the average forces over time are taken. Subtracting the reference run in the design draft gives the hydrodynamic force in the boat coordinates. Subtracting the reference run above the water corrected for the trim angle gives the total force of the water. The lift and drag forces are calculated in the world frame using the forces in x and z-direction and the trim angle.

$$F_L = F_z \cdot cos(\theta) + F_x \cdot sin(\theta) \tag{3.6}$$

$$F_D = -F_x \cdot cos(\theta) + F_z \cdot sin(\theta) \tag{3.7}$$

Next, the lift and drag coefficient can be determined as follows:

$$C_L = \frac{F_L - F_{Lreference}}{0.5\rho v^2 B^2} \tag{3.8}$$

$$C_D = \frac{F_D - F_{Dreference}}{0.5\rho v^2 B^2} \tag{3.9}$$

For the oscillations, the hydrodynamic force is calculated the same way as the hydrodynamic force in stationary runs, but with the instantaneous trim angle obtained from the laser distance measurer.

3.4. Evaluation of performed PIV experiments

The quality of the obtained PIV data is good enough to obtain a velocity field in 2D under the model. The development of the boundary layer and the flow detachment point could be found. The seeding density was high enough, and the disparity between the cameras shows no unexpected values. However, there were also four factors hindering the processing of the PIV images. The first is that the free surface in the field of view led to reflections with high intensity. The consequences are discussed in subsection 3.4.1. Reflections in the background, mainly in the images of the lower camera, are causing problems described in subsection 3.4.2. The model covered a part of the field of view. Detecting the model led to difficulties which are discussed in subsection 3.4.3. When detecting the model, the third problem, vibrations and static displacement of the model arose. This is discussed in subsection 3.4.4.

3.4.1. Reflections of the free-surface

All PIV images have clear reflections of the free surfaces. These reflections have a high intensity and overrule the particles in those areas. Furthermore, the free surface is not visible. Therefore it becomes hard to detect the flow detachment point from the velocity field. The relative intensities shown in 3.13 make clear how dominant the reflections in the images are. The picture is unusable from the start of the free surface because the reflections are also severe underwater. Different filtering methods have been tried without success. For example, the procedure of Dussol et al. [2016] did not allow to find the free surface because too much of the pictures was removed when subtracting the reflection blobs.

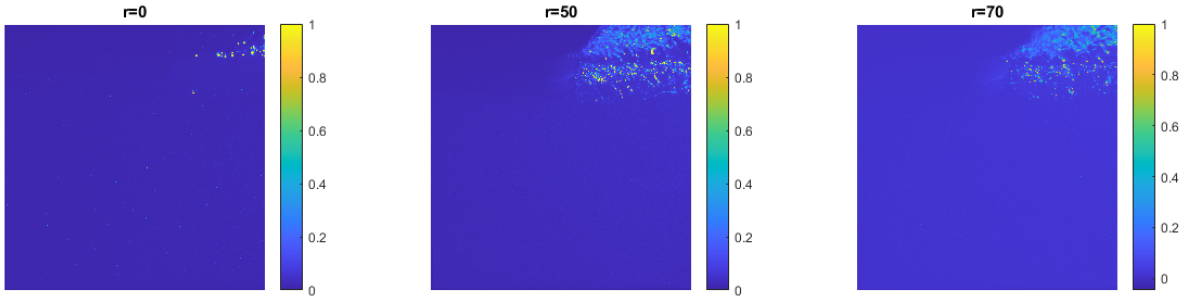

Figure 3.13: Relative intensity

3.4.2. Reflections in the background

In the field of view of camera 2, the lower camera under an angle, reflections in the background were seen. The Kelvin wake waves cause these reflections. Figure 3.14 shows pictures made by camera 2 in the centreline and the side plane measurement at 4 m/s. For 3 and 5 m/s, the wake reflection seems less present, but it still hinders the processing.

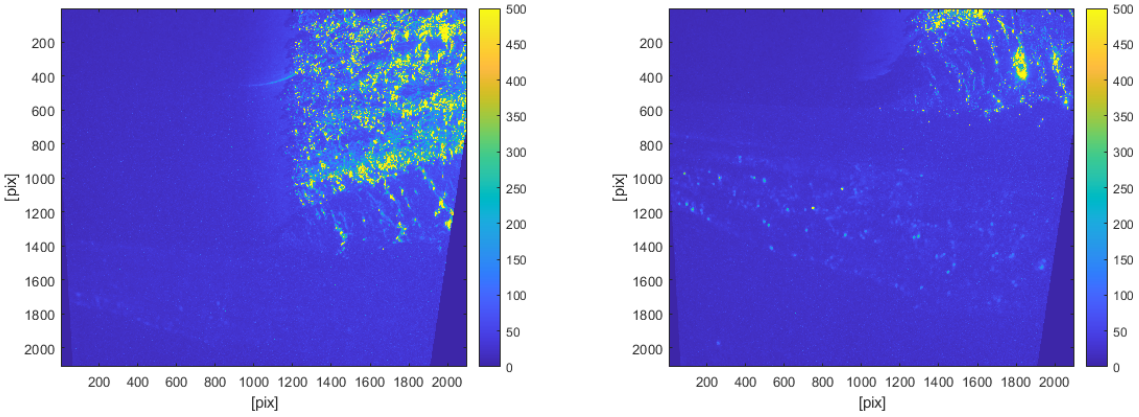

(a) Centreline (b) Side plane

Figure 3.14: Reflections in the background of camera 2 at vm=4 m/s

Because of these reflections, only the first camera can be used. Since the reflections only occurred in the pictures of camera 2, a planar PIV processing with only camera 1 was done. Using one camera has the drawback that the out-of-plane velocity cannot be found.

The reflections of the wake and the side plates were giving reflections in the background. The reflection of the side plate could not be filtered with a sliding background filter. This was partly caused by the bubbles originating from the side plates' front, but the matt black painted side plates also seem to cause some reflection. Figure 3.15 shows the results of 2D PIV with strange lines where it is not clear what is caused by bubbles and the results of reflections of the side plates and the stereo PIV result. None of these results can be used to conclude the effect of side plates on the flow.

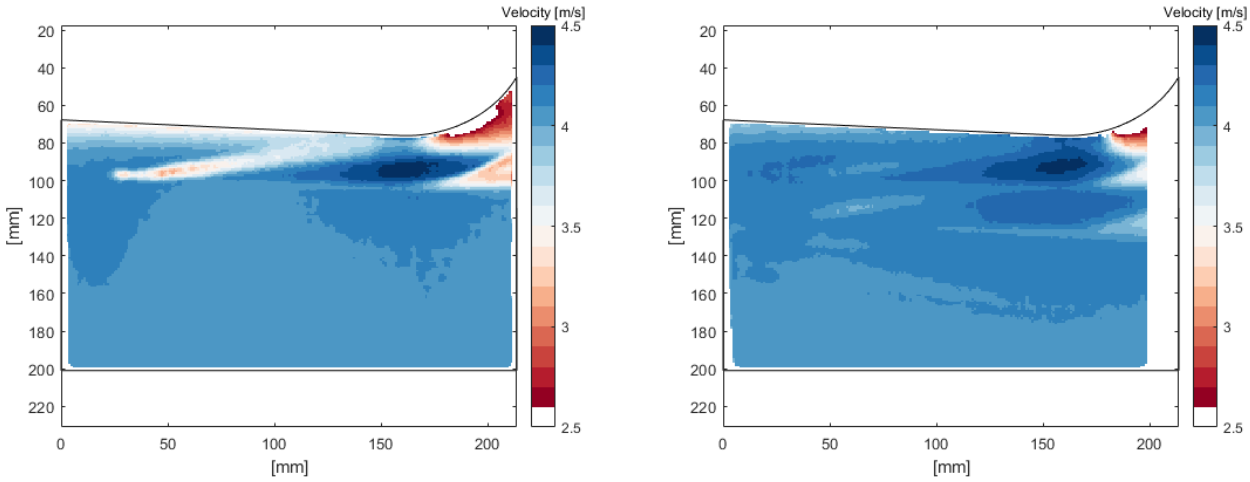

(a) Camera 1 planar PIV

(b) Stereo PIV

Figure 3.15: Measurement in side plane r=50 stern with side plate

3.4.3. Detecting and masking the model

An accurate model detection is important because when obtaining a velocity field or profile, one wants to know the exact position related to the model. Mainly in the boundary layer where a high velocity gradient will be found, a displacement of the model can lead to big mistakes in the velocity. The risk of cutting too much of the model is that a part of the flow field is cut off, and a too-high velocity close to the model is found. The risk of leaving a part f the model is that vectors are found in an area where the model is located, and wrong or no velocity vectors are found close to the hull.

For the straight stern with a trim angle of 3 degrees, the bottom seemed to have a trim angle slightly smaller than 3 degrees, namely 2.75 degrees. That the model position varies per run is confirmed with the laser distance measurer. In all other figures where the bottom was not visible, the trim angle had to be chosen, so there is a slight deviation between the actual location of the model and the mask location. However, the detected trim angle of 2.75 degrees is not necessarily a better estimation of the model location because this is based on clicks on intensity peaks in a sum image.

The detection of the rounded part caused the most trouble, although the reflection made it clearly visible. A smaller radius than the actual model was found using circle detection methods like a Hough transform and seemed to fit very well. Finally, a least-squares fit for a circle with a fixed radius is used to detect the rounded part. This fit seemed to fit less accurately, but since it is certain that the model has the design radius, the fixed radius mask is considered the most accurate.

Markings on the model would have helped out with finding the exact location. Nevertheless, in the final masks, a maximum deviation of 9 pixels between the start points of the rounding is found. This corresponds to 1.3 mm.

3.4.4. Vibrations

When detecting the model for making masks, it was found that the model vibrated and has an average displacement dependent on the velocity and trim angle. The average displacement is caused by the hydrodynamic force and the consequent elastic deformation of the force sensors. The displacement relative to the static trimmed position could be found with measurements from the laser distance measurer. As shown in figure 3.16, the higher the velocity, the bigger the average displacement. Also, for

a trim angle of 6 degrees, the average displacement is bigger than for 3 degrees trim angle because the lift force is higher. This results from the higher hydrodynamic force, leading to a larger elastic deformation of the force sensors.

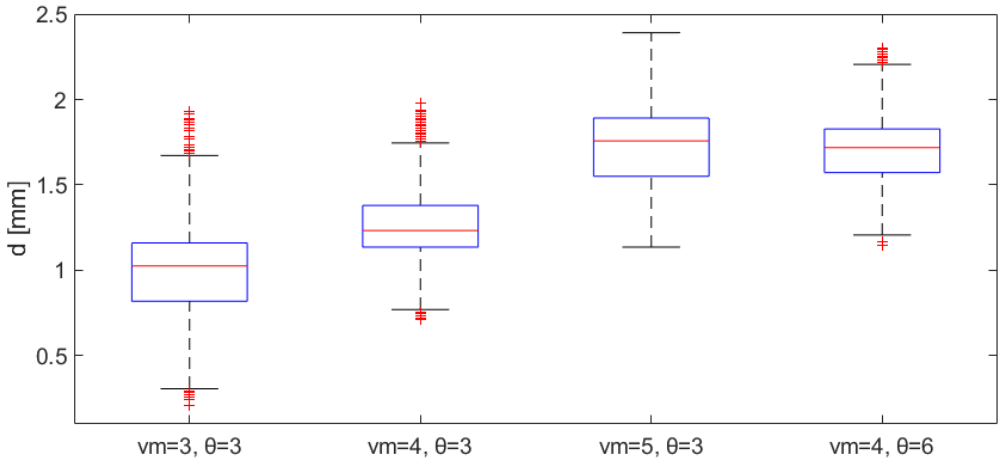

Figure 3.16: Displacement relative to static trimmed position measured with laser distance measurer

Table 3.6: Displacement relative to static trimmed position measured with laser distance measurer

	Mean displacement [mm]	**Standard deviation [mm]**
v_m=3, θ=3	1.00	0.24
v_m=3, θ=3	1.25	0.17
v_m=5, θ=3	1.74	0.22
v_m=4, θ=6	1.71	0.16

The laser distance measurer was positioned 5 cm from the stern, and there was no second measurer used, so it cannot deviate how much the model is trimmed and how much the model is displaced in the z-direction. For the runs with the straight stern, velocities of 3, 4, and 5 m/s, and a trim angle of 3 degrees, the bottom is detected in the PIV images, and the vibration in pixels is converted to mm. The resulting distribution of positions is similar.

4

Results and discussion: effects of tested factors on lift force

The effects of the stern shape, velocity, trim angle, side plates, and pitch oscillations on the negative lift force were examined. This chapter shows the results of the measured forces, and the results are discussed. In the first section, the results of the basic runs with varying shape velocity and trim angle are presented. A comparison with the previous interceptor diffuser study is made. Then, the effect of the side plates is shown in section 4.2. In section 4.3, the lift forces during forces pitch oscillations are presented.

4.1. Effect of stern shape, velocity, and trim angle

The measured total lift force depending on the velocity for the different stern shapes is shown in figure 4.1. For each combination of shape velocity and trim angle, there were two runs since a PIV measurement in the centreline and the plane on the side was done. The presented force is the average of both runs and the average over the run time. Figure 4.2 shows the measured total drag force depending on the velocity.

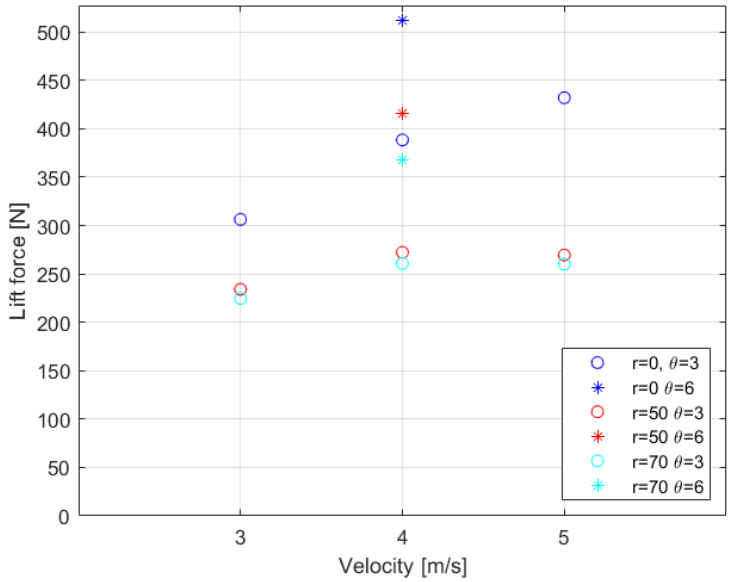

Figure 4.1: Total lift force

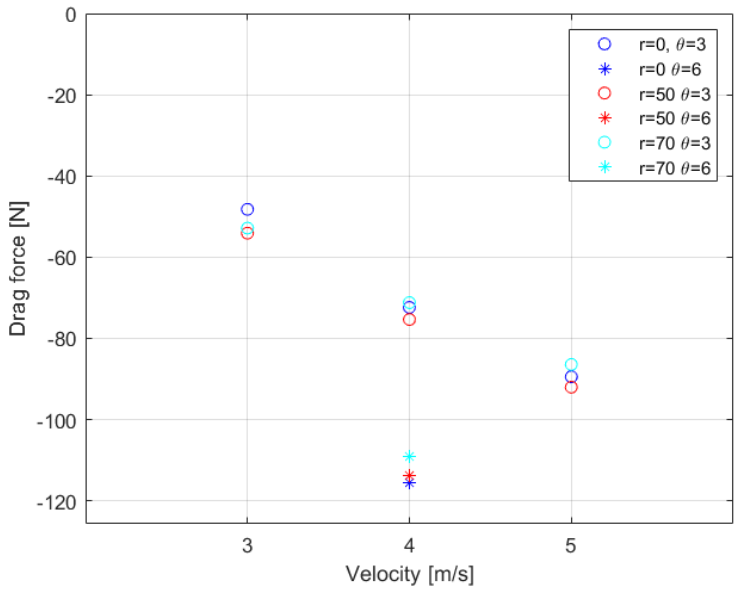

Figure 4.2: Total drag force

The lift and drag increase with velocity and with trim angle. The lift force decreases with increasing stern radius. This means that the negative lift created by the 70 mm stern is larger than by the 50 mm stern, increasing the range of lift that an interceptor diffuser combination can create.

The negative lift force created by the rounded sterns is related to the reference stern by calculating the lift coefficient (equation 3.8). The same is done for the drag forces. Table 4.2 presents the dimensionless lift and drag coefficients.

Table 4.2: Lift and drag coefficients

		C_L	C_D
r=50	v_m=3,θ=3	-0.1004	-0.0082
	v_m=4,θ=3	-0.0908	-0.0023
	v_m=5,θ=3	-0.0813	-0.0013
	v_m=4,θ=6	-0.0756	0.0015
r=70	v_m=3,θ=3	-0.1136	-0.0064
	v_m=4,θ=3	-0.0999	0.0009
	v_m=5,θ=3	-0.0859	0.0015
	v_m=4,θ=6	-0.1127	0.0052

There is a difference found between these measurements in the centreline plane and side plane. It differs whether the lift force measured in the centreline or the side plane is higher. Tables 4.3 and 4.4 show the relive increase in lift and drag force at the side plane relative to the centreline plane. In general, the side plane measurements give a slightly higher lift and drag force. An explanation could be that there is a difference in model depth when displacing it in y-direction due to a misalignment in the setup.

Table 4.3: Relative lift force difference [%]

	r=0	**r=50**	**r=70**
$v_m = 3$, θ=3	5.9	2.3	0.8
$v_m = 4$, θ=3	0.8	3.6	0.8
$v_m = 5$, θ=3	1.7	4.8	2.3
$v_m = 4$, θ=6	2.0	0.9	1.4

Table 4.4: Relative drag force difference [%]

	r=0	**r=50**	**r=70**
$v_m = 3$, θ=3	12.4	6.2	0.1
$v_m = 4$, θ=3	0.8	2.2	0.1
$v_m = 5$, θ=3	0.7	0.9	0.6
$v_m = 4$, θ=6	-0.2	0.2	-0.4

The lift and drag coefficients are compared to the values found in the previous experiments from Rijkens et al. [2013]. These are shown in figures 4.3 and 4.4. The red and black data points are the ones to compare.

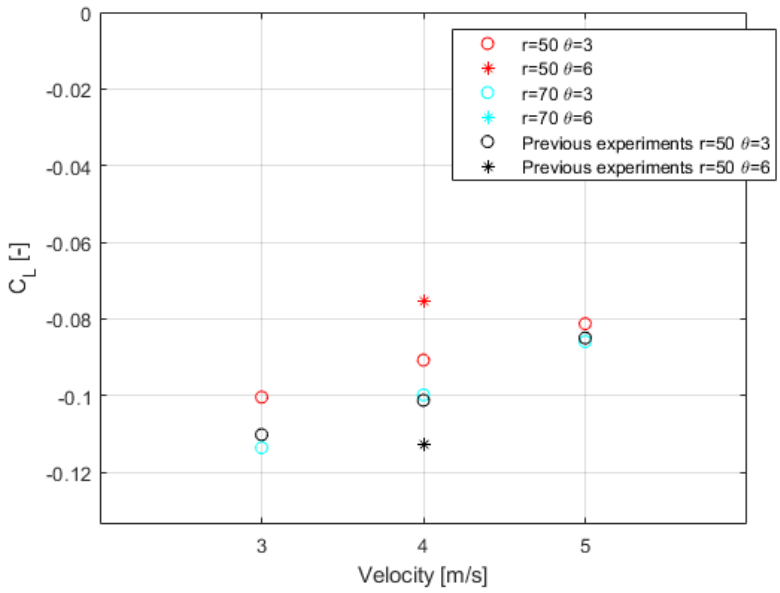

Figure 4.3: Lift coefficients compared to previous experiments

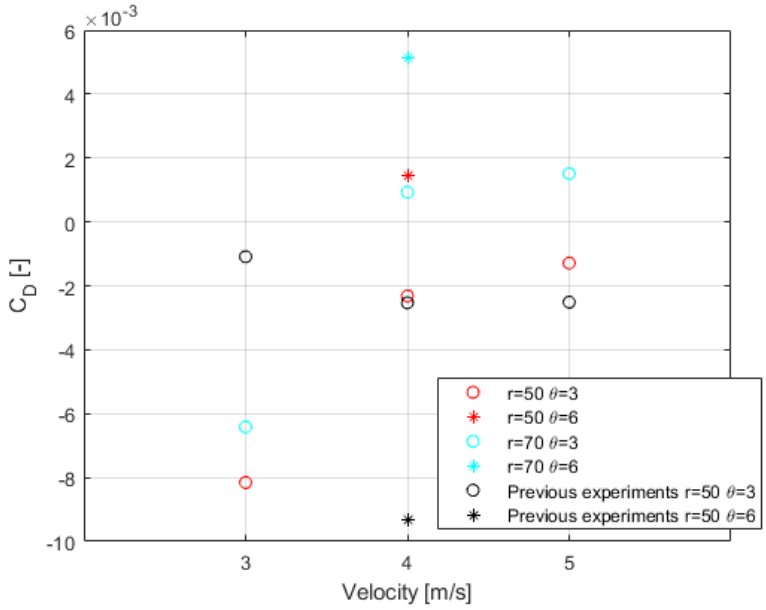

Figure 4.4: Drag coefficients compared to previous experiments

For all velocities, the negative lift found in the PIV experiments was smaller than measured in the previous experiments. The trend of a decreasing lift coefficient with velocity is similar for the trim angle of 3 degrees. For 6 degrees, the opposite is observed. This increase in lift coefficient with trim angle could be caused by high lift forces measured for the stern radius of 50 mm. Bubbles have been observed in the PIV images, so the transition in the bottom with the tape may have caused this high force in the specific case of the 6 degrees trim angle.

The transition position to the changeable stern part is a difference between the models that have to be drawn attention. In the previous experiments, the transition to the changeable stern part was located at the start of the rounding, so 50 mm from the transom. While in the PIV experiments,

the transition was 800 mm from the random. The transition right before the rounded part may have led to a more turbulent flow, leading to a longer attachment. This could explain the larger negative lift coefficient, but it is impossible to check this hypothesis because no flow observations were made in the previous experiments.

The drag coefficients seem to show big differences. However, it has to be noted that the differences in the measured drag forces were really small. The drag may in both experiments also be affected by the transition to the stern part. When the interceptor diffuser was tested before by Rijkens et al. [2013], the interceptor plate was implemented. The maximum height of the interceptor plate was 30 mm relative to the original bottom height. Therefore it was questioned whether the flow was disturbed and the radius of 50 mm could obtain higher lift negative lift. The results show that this was not the case because the lift measured without an interceptor plate was even slightly smaller.

4.2. Effect of side-plates

Table 4.5 shows the relative increase in lift force with the side plate relative to the situation without the side plate. A negative relative lift force means that the effect of the side plate is beneficial because the negative lift is increased. It is found that the side plates increase lift force for the straight stern. For the radius of 50 mm for the higher velocities, the side plates have the wanted effect of increasing the negative lift. However, there is a large difference between the effect at 3 m/s and the higher velocities. Also, for the straight stern, there is no trend to observe. The effect on the out-of-plane velocity could not be checked because reflections in the background severely hindered the processing of PIV images from the lower camera. So no explanation for the effects could be found in the PIV results.

Table 4.5: Relative dynamic lift and drag force increase by side plate in %

		Dynamic lift force increase [%]	**Dynamic drag force increase [%]**
r=0	$v_m = 3$, θ=3	13.0	-0.6
	$v_m = 4$, θ=3	3.1	-0.1
	$v_m = 5$, θ=3	11.7	7.6
	$v_m = 4$, θ=6	5.2	-0.8
r=50	$v_m = 3$, θ=3	9.8	4.2
	$v_m = 4$, θ=3	-5.2	1.6
	$v_m = 5$, θ=3	-6.2	-1.7

4.3. Effect of oscillations

Forced pitch oscillations have been performed to see whether the lift force would be predictable at higher frequencies. The resulting lift force for each frequency is plotted in figure 4.5.

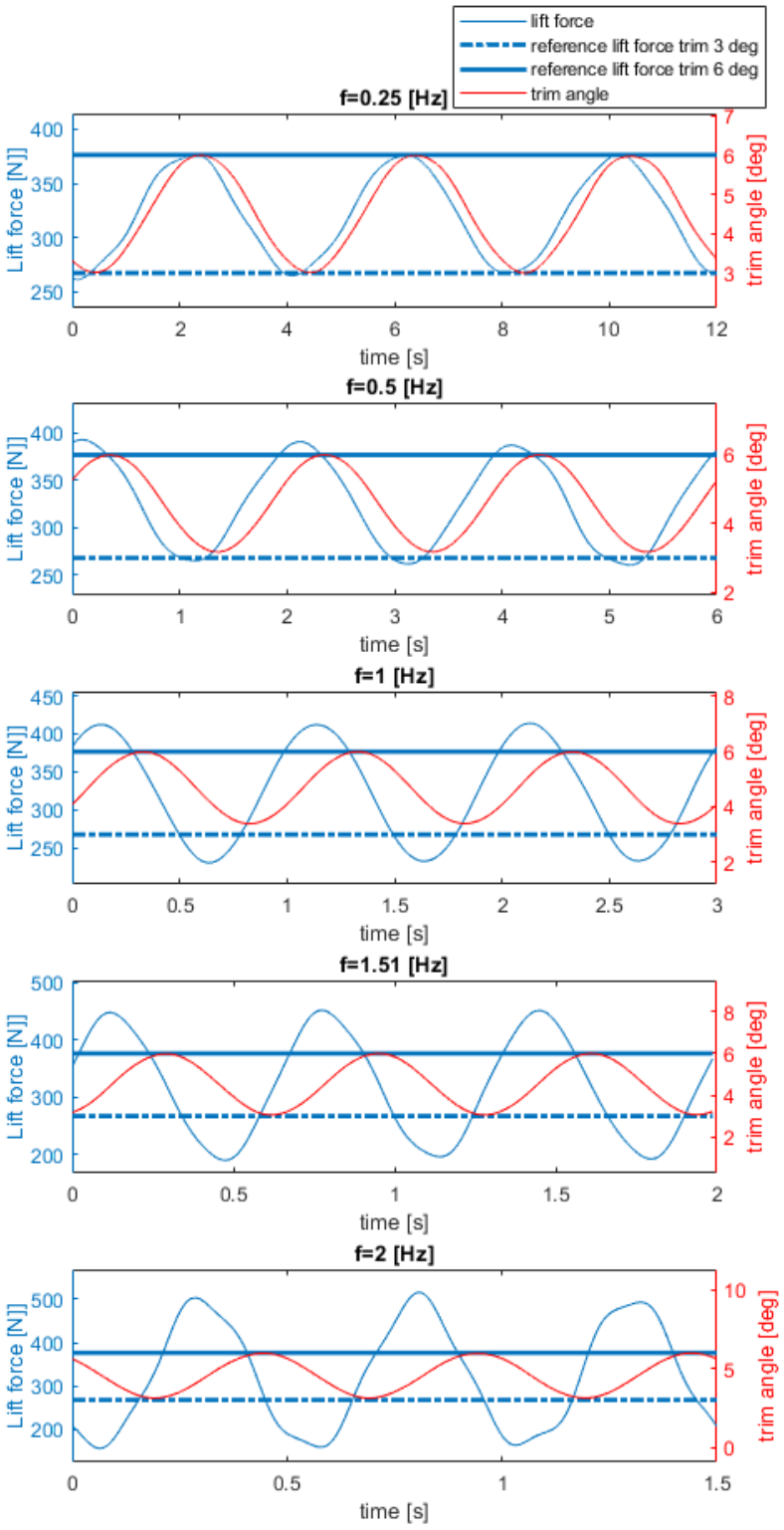

Figure 4.5: Lift force during forced pitch oscillations

A phase difference can be observed between the trim angle and the lift force. This effect can be attributed to the fact that it is a forced oscillation. The forced motion from 3 to 6 degrees trim angle induces an extra lift force due to the pitch velocity and acceleration. The same happens when the trim is changed from 6 to 3 degrees. The phase difference increases with increasing frequency, which is logical since the pitch velocity and acceleration increase. An opposite effect in the phase difference would be expected as a result of the moment of inertia. Oscillating the model above the water would have resulted in a delay of the lift force relative to the trim angle. The contribution of both effects is not distinguished. However, the added lift caused by the pitch velocity and acceleration is dominant over the moment of inertia since the lift force is ahead of the trim angle.

For the higher frequencies, more fluctuation in the lift force is seen compared to the sinusoidal motion. The measured force is filtered by applying a low pass filter. The cut-off frequency was four times the oscillation frequency.

In the explanations above, the flow detachment is not taken into account. The effect of oscillations of the flow detachment point is examined and presented in the last section of chapter 5 after the flow detachment in stationary runs is presented.

5

Results of PIV measurements and the effect of flow acceleration and detachment on lift force

In this chapter, the flow under the diffuser stern obtained with the PIV measurements is presented. Attention to the acceleration and detachment of the flow will be drawn since these are the important factors influencing the lift force. The boundary layers found in the PIV experiments are compared with a theoretical boundary layer profile. Moreover, the boundary layer development over the hulls and a comparison between the shapes and velocities are shown. With this information, a relation between the acceleration of the flow and the lift force is presented at the end of section 5.1. In section 5.2, the relation between the flow detachment point and the lift force is presented. Lastly, the flow detachment during forces pitch oscillations is shown in section 5.3.

5.1. Development of boundary layers

The velocity fields under the hull are obtained from the PIV data. Figures E.1, E.2, and E.3 show the obtained flow fields for 4 m/s for the different hull shapes. In appendix E.1, the flow fields for 3 and 5 m/s runs of all stern shapes can be found.

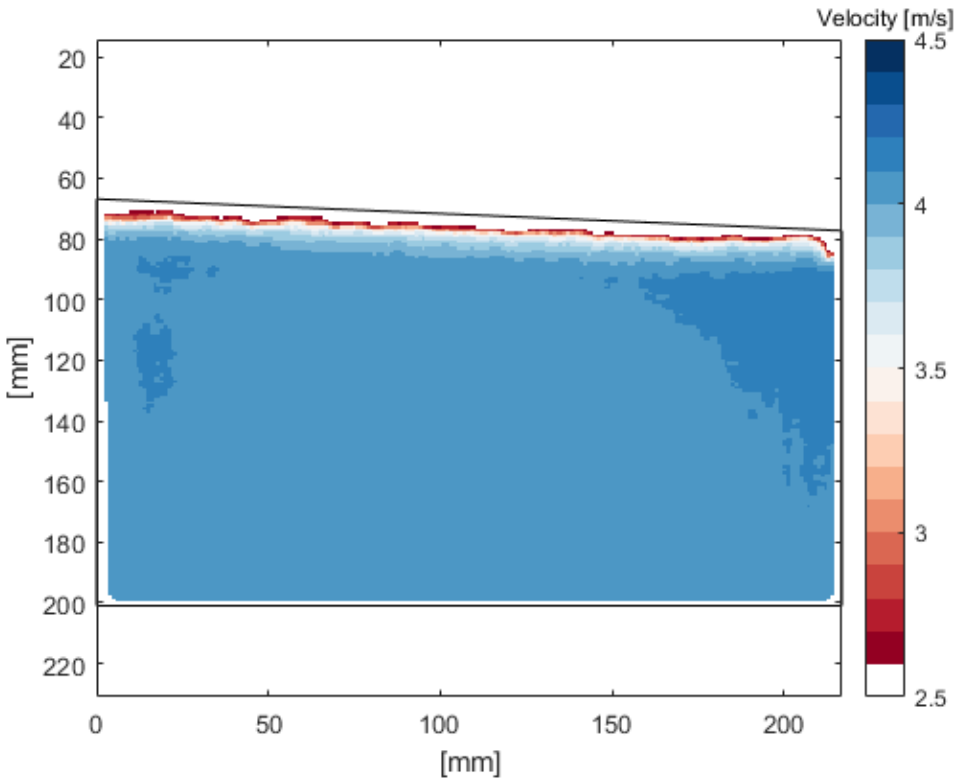

Figure 5.1: Flow field for straight stern, vm=4, $\theta = 3$

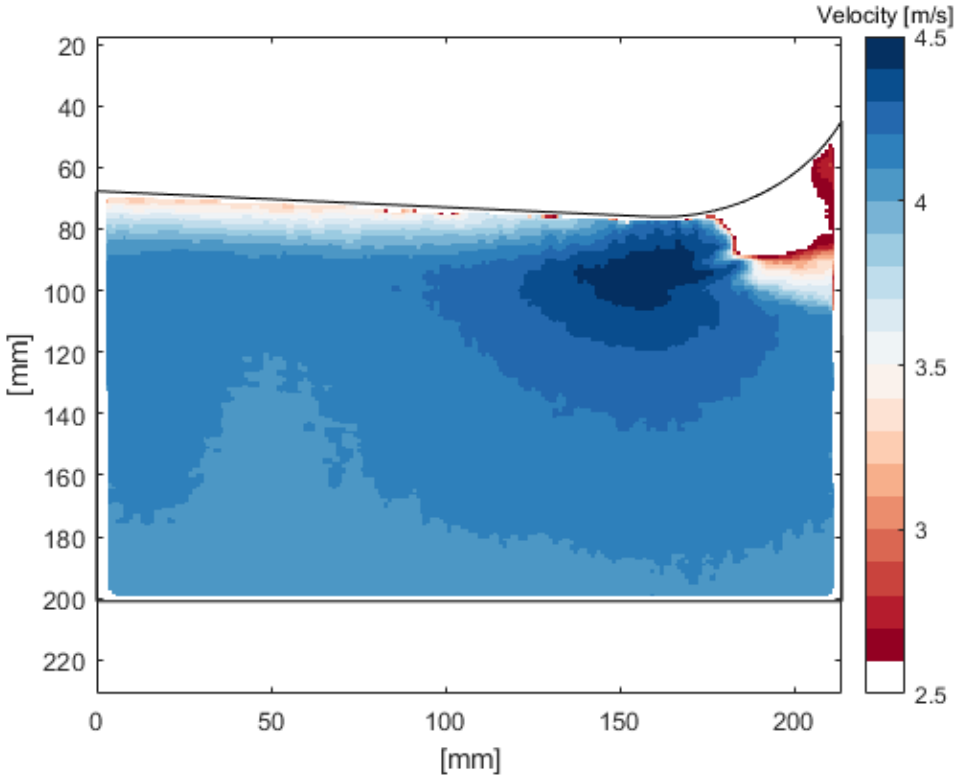

Figure 5.2: Flow field for r=50 stern, vm=4, $\theta = 3$

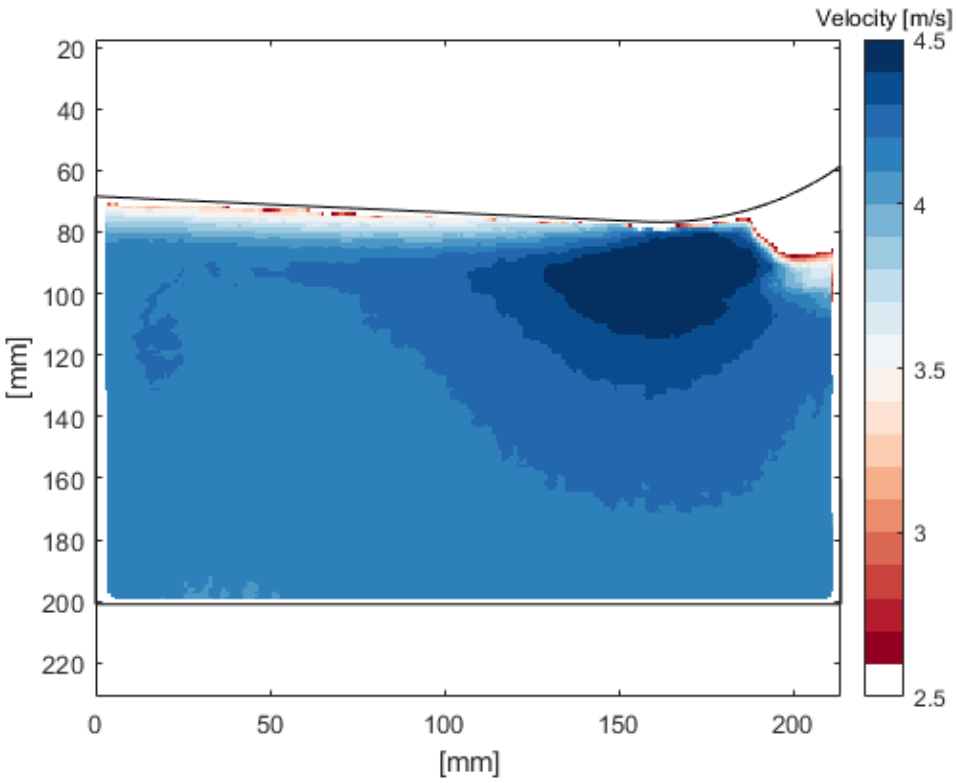

Figure 5.3: Flow field for r=70 stern, vm=4, $\theta = 3$

In all flow fields can be observed that the flow accelerates along the hull. Under the round of stern, the acceleration is more obvious. The high velocity will induce a low pressure. From these fields, the boundary layer profiles are found and presented in appendix E.2.

Figure 5.4 shows the velocity profiles for the different velocities and shapes 150 mm from the stern, so 100 mm from the point where the rounded part starts. At 150 mm from the stern, the influence of the shape is expected to be negligible. In figure 5.5, the influence of the shape is visible. It shows the velocity profile 50 mm from the stern at the start of the rounded part for the rounded stern shapes.

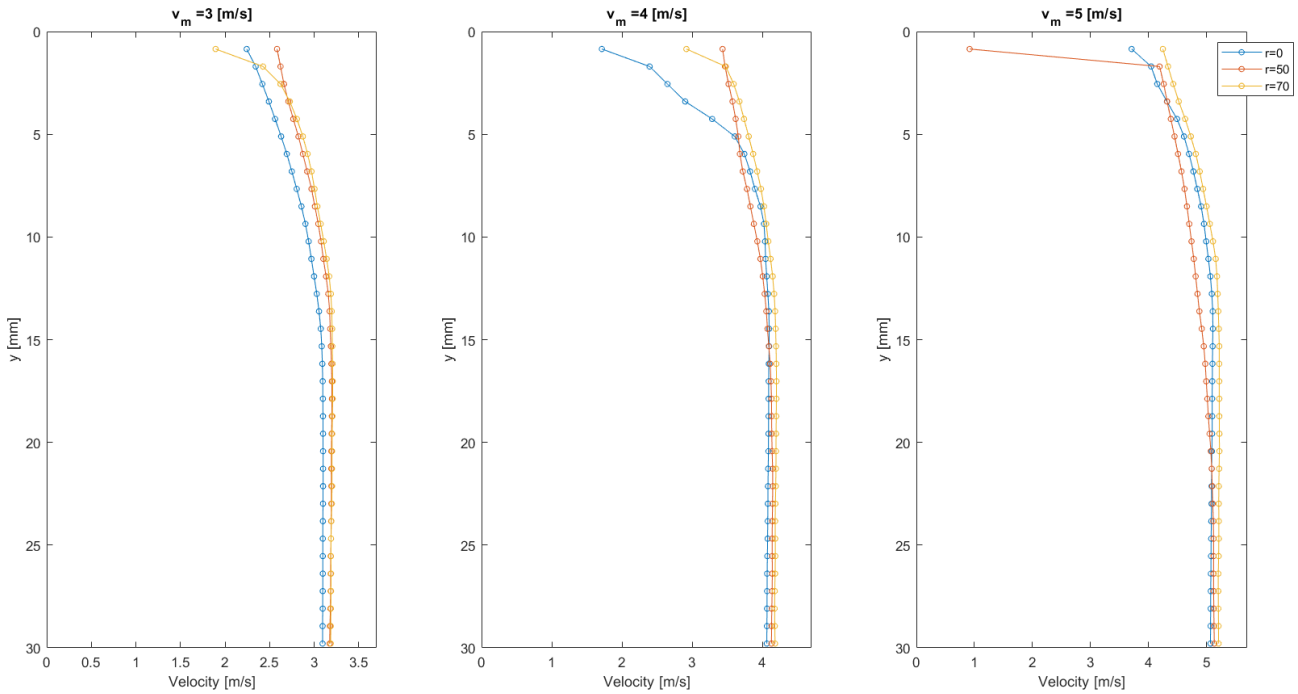

Figure 5.4: Velocity profiles under the hull 150 mm from the stern

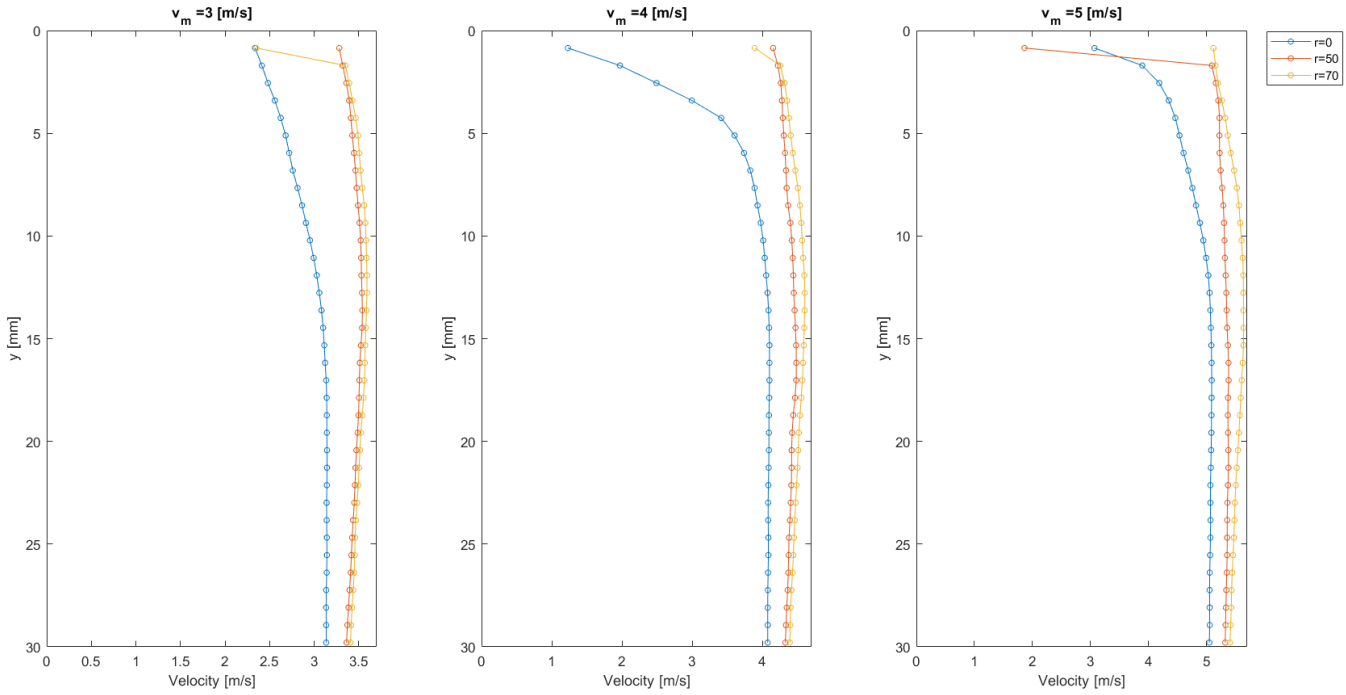

Figure 5.5: Velocity profiles under the hull 50 mm from the stern

The points indicate the PIV data points, so the resolution results from the chosen interrogation area sizes and the overlap. Except for the deviations in the 5 mm closest to the hull, the velocity profiles

look similar at the position 150 mm from the stern. This can be explained by the high uncertainty close to the hull. The high uncertainty is caused by fewer vectors resulting in an average vector because vectors are thrown away in the processing when the standard deviation is bigger than 2. Vectors with a larger standard deviation can be found because the correlation between two images gives a wrong result. This can be caused by the fact that the displacement of the particles is very low close to the hull. Also, the vibration of the model, discussed in section 3.4.4, can influence the reduced number of vectors close to the hull. If the actual model is below the mask, the model is present in the interrogation area closest to the mask and not the particles, so there can not be a correlation.

At 50 mm from the stern, it is clear that the rounded sterns induce a higher velocity. The velocity at the start of the 50 and 70 mm radius curve is higher than the velocity under the straight stern at the same location. The relative acceleration decreases with the model velocity, and the acceleration by the 70 mm stern is slightly higher than the acceleration by the 50 mm stern.

The boundary layer under the straight stern shape at 150 mm from the transom compared to theoretical profiles is shown in figure 5.6 to validate the PIV results.

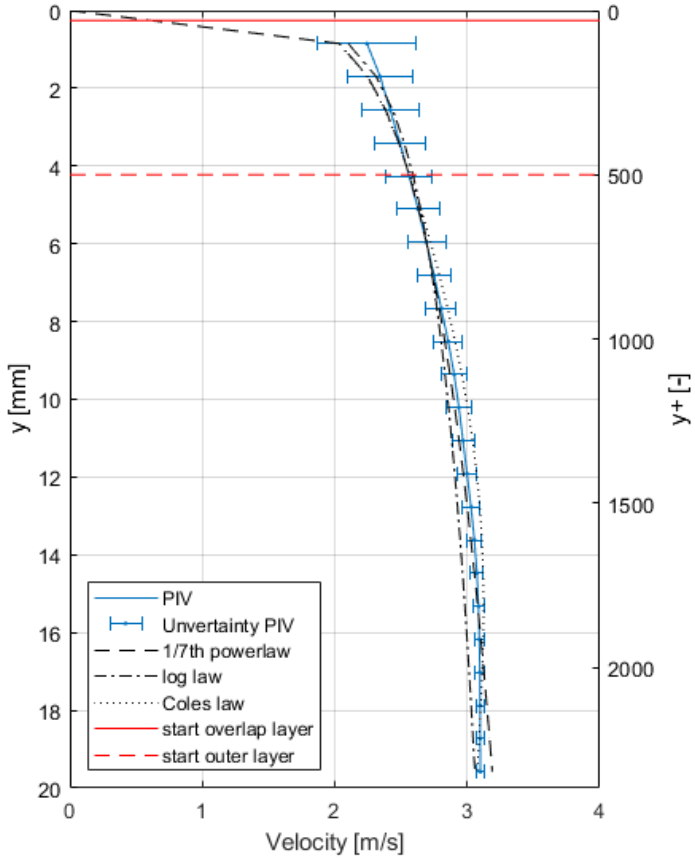

Figure 5.6: Velocity profile 150 mm from the stern at for $v_m = 3m/s$ compared to theoretical models

The used theoretical methods were described in appendix B. The difficulty in comparing these theories to experimental data is that the model is not a flat plate. The bow shape and its inducing effects on the flow make it hard to define the actual wetted length. Furthermore, the model was towed under an angle that influences the pressure gradient. Therefore the shown comparison was made by

taking the boundary layer thickness found in the experiment and applying the theories with the found thickness as input. It shows that the profile shape is very similar. The found boundary layer thickness corresponds with a theoretical wetted length of 58 cm which is shorter than the length that one would observe.

For examining the effect of the acceleration on the lift, the maximum flow velocity is divided by the model velocity. Table 5.1 shows the resulting dimensionless factors. It is found that the stern radius of 70 mm induces a higher velocity under the stern than the radius of 50 mm. At the same time, a higher negative lift coefficient was found for the 70 mm stern radius. (Table 4.2). The velocity relative to the velocity measured under the straight stern decreased with increasing velocity for both stern radii. This is a similar trend as the negative lift coefficient showed that it also decreases with velocity.

Table 5.1: Maximum flow velocity divided by the model velocity (v_{max}/v_m)

	r=0	**r=50**	**r=70**
v_m = 3	1.08	1.19	1.22
v_m = 4	1.05	1.13	1.16
v_m = 5	1.03	1.08	1.14

5.2. Effect of flow detachment on lift force

With the method described in section 3.3, the flow separation point is determined for both rounded sterns. Ten random examples of the detected location are shown in figures 5.7 and 5.8. The white lines indicate the stern shape, and the small red circles indicate the determined detachment points.

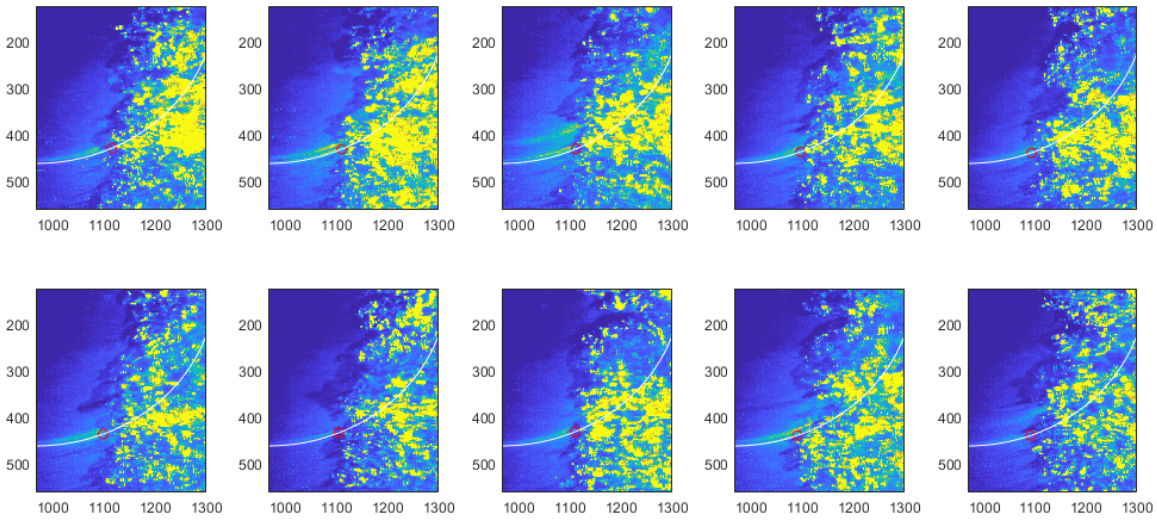

Figure 5.7: Examples of the flow separation detection in 10 images of the r=50 stern

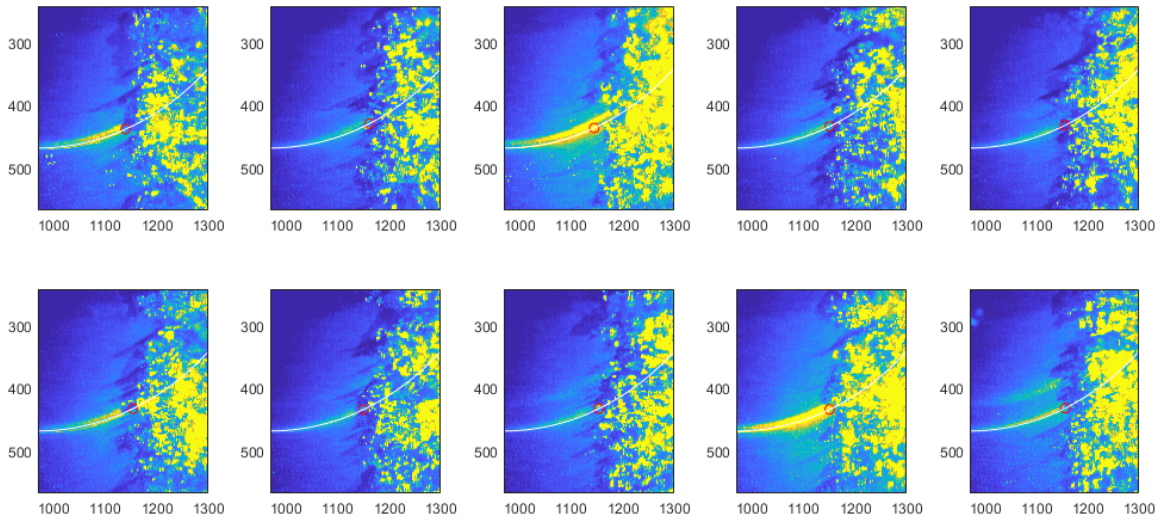

Figure 5.8: Examples of the flow separation detection in 10 images of the r=70 stern

The pictures show that this method defines flow detachment point as accurately as one can observe by eye. However, it is one method with one threshold applied to all images. So it is much more reliable, and conclusions can be drawn from the differences between the runs. Outliers in the detected locations are found because reflecting bubbles cause high intensities in the image before the flow detaches. The x positions of these bubbles are found as detachment points because the method is based on the gradient of intensity in the x-direction. The bubbles can give an intensity increase as high as the free surface reflection. The outliers are filtered out by using the *rmoutlier* function of MATLAB. It removes values that deviate more than three times the standard deviation from the mean.

After removing the outliers, the following values are found for the angle until the point where flow stays attached to the rounded stern. (Figures 5.9 and 5.10)

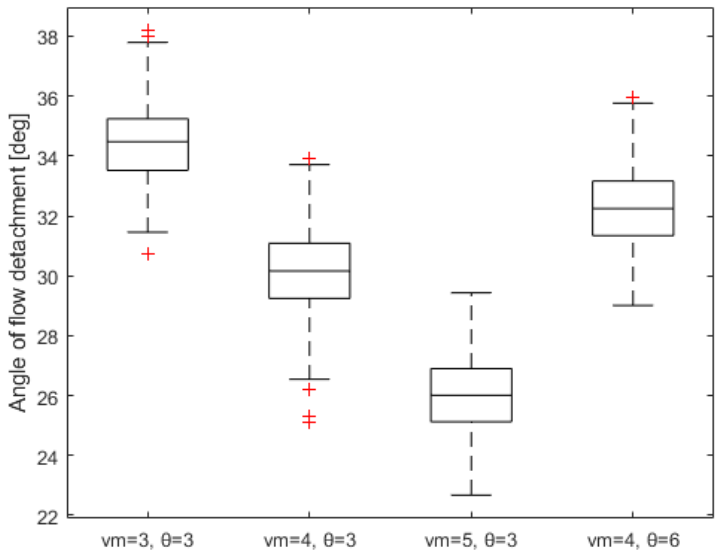

Figure 5.9: Angle of flow detachment on stern radius **50** mm measured from start curvature

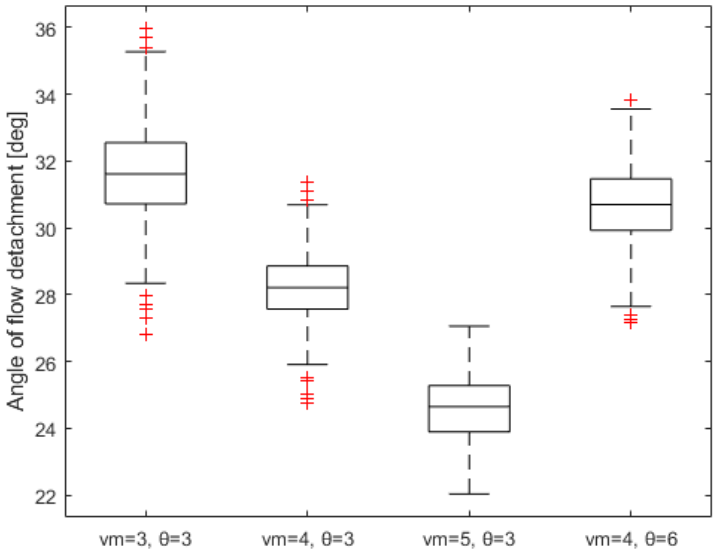

Figure 5.10: Angle of flow detachment on stern radius **70** mm measured from start curvature

Figures 5.11 and 5.12 give a visual representation of the determined flow detachment points. The angles can be intuitively misleading because the same angle means a longer attachment length for 70 mm than a 50 mm radius. Therefore table (5.2) includes both the angles and attachment lengths.

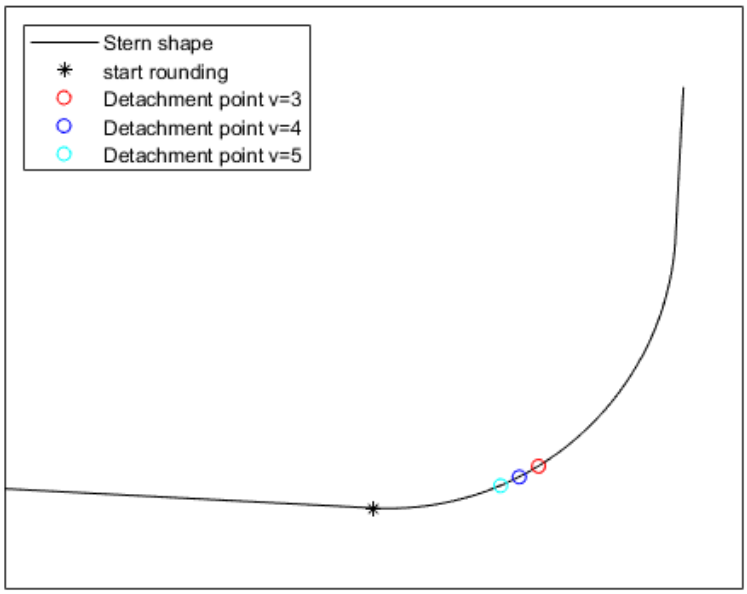

Figure 5.11: Average flow detachment points for different velocities on the stern with radius 50 mm

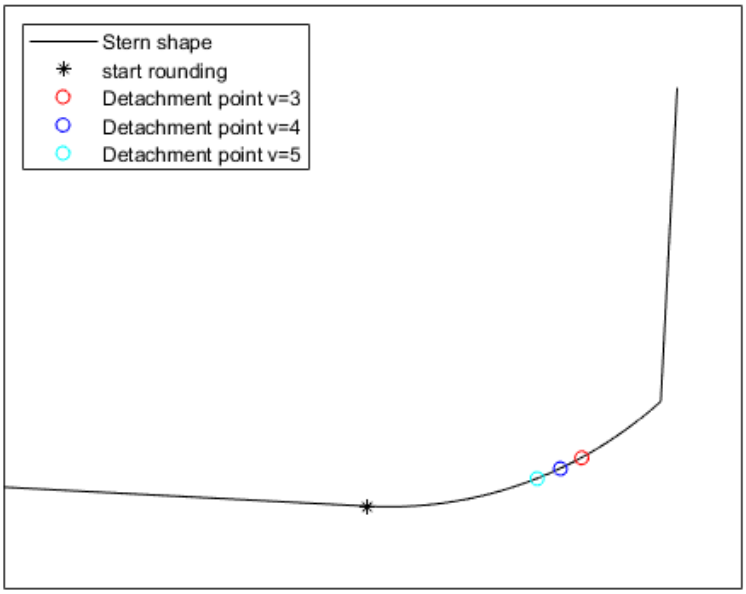

Figure 5.12: Average flow detachment points for different velocities on the stern with radius 50 mm

Table 5.2: Mean detected flow detachment angle and attachment length

		angle [deg]	standard deviation [deg]	length [mm]	standard deviation [mm]
r=50	$v_m = 3$	34.5	1.3	30.1	1.2
	$v_m = 4$	30.1	1.4	26.3	1.2
	$v_m = 5$	26.0	1.3	22.7	1.1
r=70	$v_m = 3$	31.6	1.5	38.6	1.8
	$v_m = 4$	28.2	1.1	34.4	1.3
	$v_m = 5$	24.6	0.9	30.1	1.1

The negative lift is expected to decrease with a decreasing attachment length because the lift depends on the area over which the pressure of the water acts. This corresponds with the found lift coefficient and the found attachment length. The negative lift coefficient decreases with velocity, and so does the attachment length. This holds for both stern radii. The attachment length for the 70 mm stern is longer than for the 50 mm stern. This correlated with the negative lift coefficient that increases with stern radius, but it can not be seen separately from the flow acceleration.

5.3. Flow detachment during oscillations

The flow detachment angle during forced pitch oscillations is shown in figure 5.13.

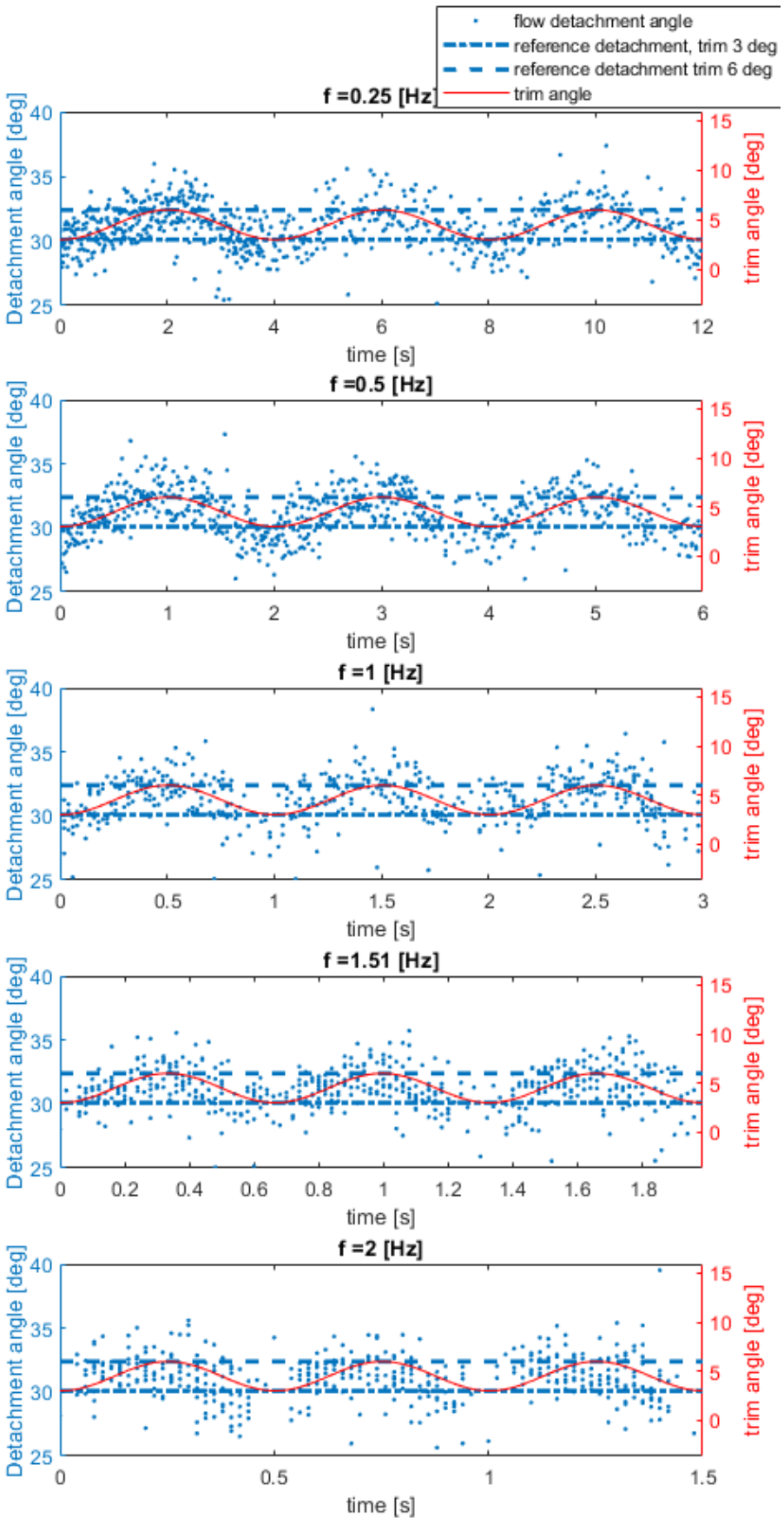

Figure 5.13: Degree of detachment in oscillations for stern shape r=50 mm

It is important to mention that the reference line for the detachment angle is an average angle obtained in stationary runs. During the stationary runs, the standard deviation of the detachment angle was 1.4 degrees for the trim angle of 3 degrees and 1.3 degrees for the trim angle of 6 degrees. Flow detachment angles below 25 and above 40 degrees were removed because these are considered to be unrealistic. The figure shows fewer points for the higher frequencies and a trim angle close to 3 degrees, so these must have been removed because of the applied limits. Probably reflections were causing an early flow detachment detection. After removing the unreliable angles, it was found that all detachment angles during the oscillation are in the range of the standard deviation.

6

Validation of numerical pre-study

An important step in the development of the interceptor diffuser will be a shape optimization. Therefore a suitable numerical method has to be found. This chapter shows the similarities and differences between the results of the numerical pre-study and the results of the PIV experiments. Therefore the measured forces, the development of the boundary layer, and the flow detachment point will be compared. Section 6.1 starts with the forces, in section 6.2 the boundary layer profiles are compared, and in section 6.3 the flow detachment is compared.

6.1. Forces

Figures 6.1 and 6.2 show the total lift and drag forces of the numerical and experimental study. The lift and drag forces measured in the experiment are higher than the found results in the CFD study. Looking at the lift force for the stern radius of 50 mm, the deviation is minimal. The deviation of the lift forces for the 70 mm stern is significant, keeping in mind the difference it makes in the lift coefficient.

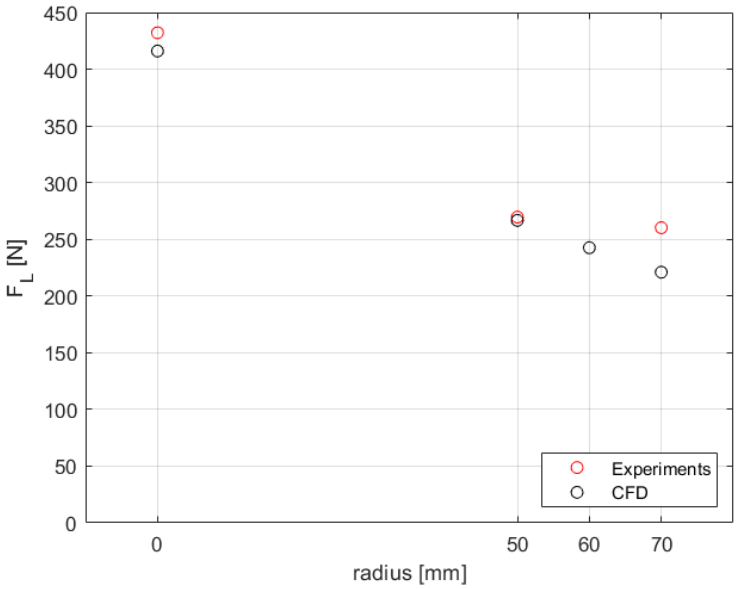

Figure 6.1: Comparison of total lift forces experiments and CFD study

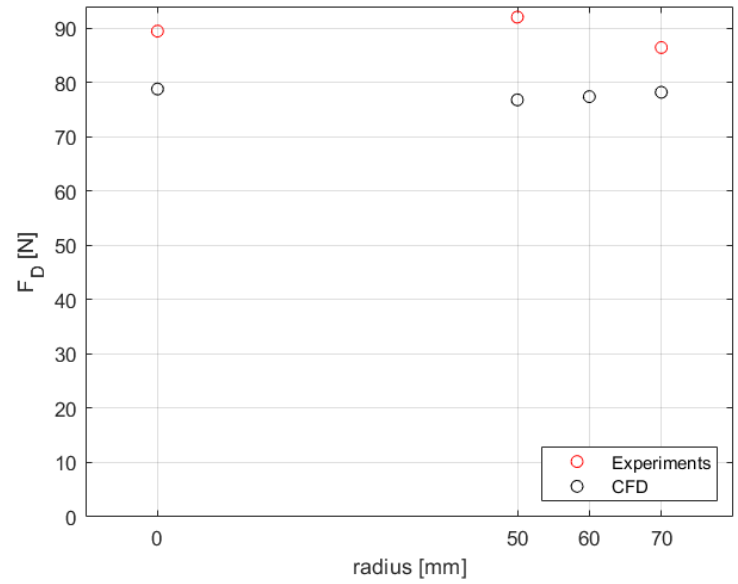

Figure 6.2: Comparison of total drag forces from experiments and CFD study

The model used in the experiments was equipped with a changeable bottom part to test the different stern shapes. The transition from the bow to the changeable bottom part was located underwater. Adhesive tape was used to make the transition as smooth as possible, but this is a distinguishable difference between the experiment and the smooth model in the numerical study that could explain the difference in drag. The difference in lift can not be attributed to this difference. The velocity profiles and flow detachment points presented in the next sections may answer the cause of the difference in lift force.

6.2. Boundary layer velocity profiles

The boundary layer development obtained by the PIV experiments and numerical study is laid on top of each other and showed in figures 6.4 and 6.5. The chosen locations to compare are visualized in figure 6.3. The presented values indicate the distance in mm relative to the start of the rounded stern. The dotted lines correspond with the plotted 25 mm.

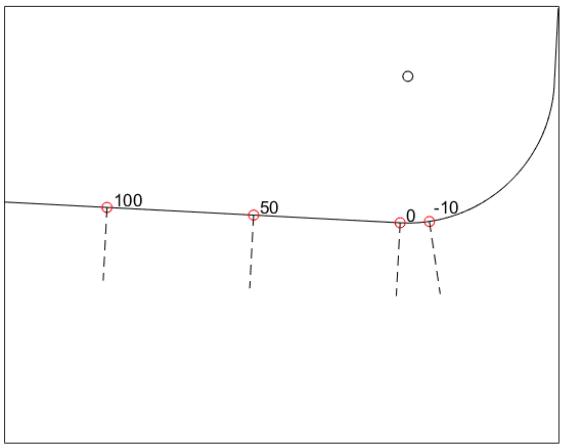

Figure 6.3: Locations for boundary layer comparison in mm relative to the start of rounded stern

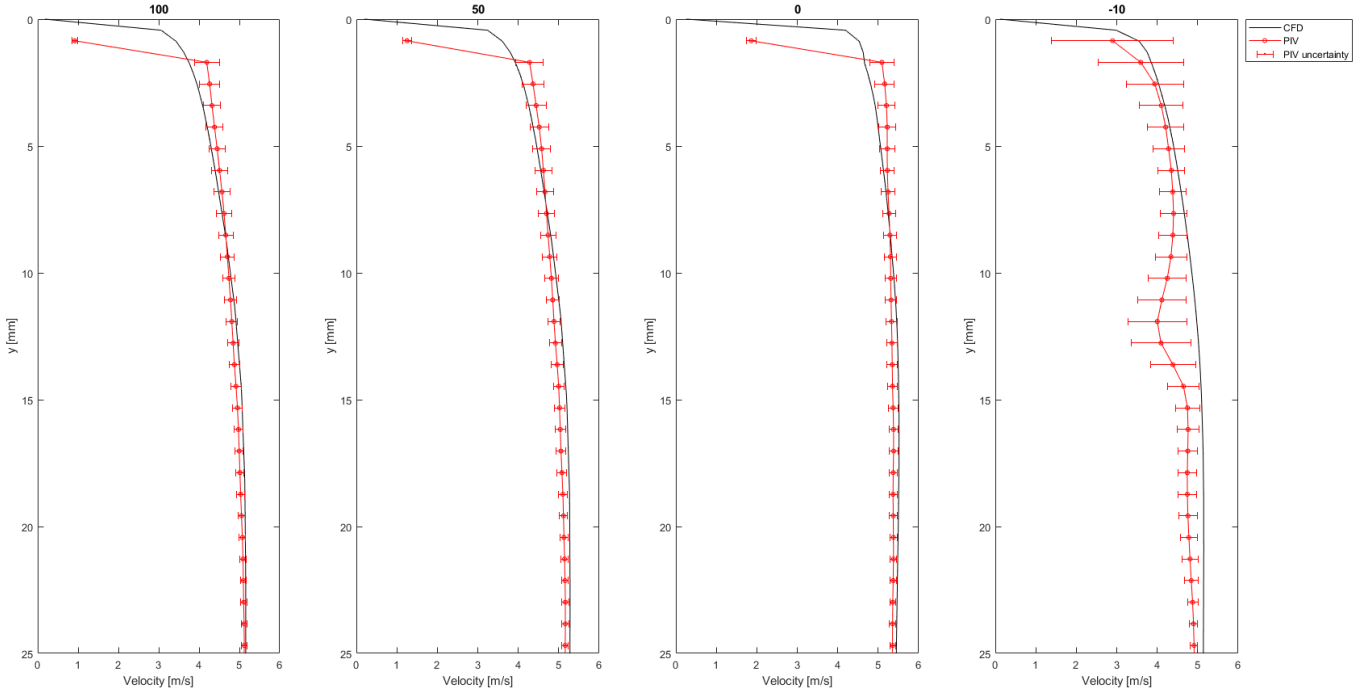

Figure 6.4: Comparison of velocity profile for stern radius 50 mm and a velocity of 5 m/s

These boundary layers show comparable profiles. The first 5 mm is different, but the uncertainty

is high. For the boundary layer 10 mm on the rounded stern, the right plot, another deviation is seen. The reflections cause this in the area under the rounded stern where no velocity field could be found.

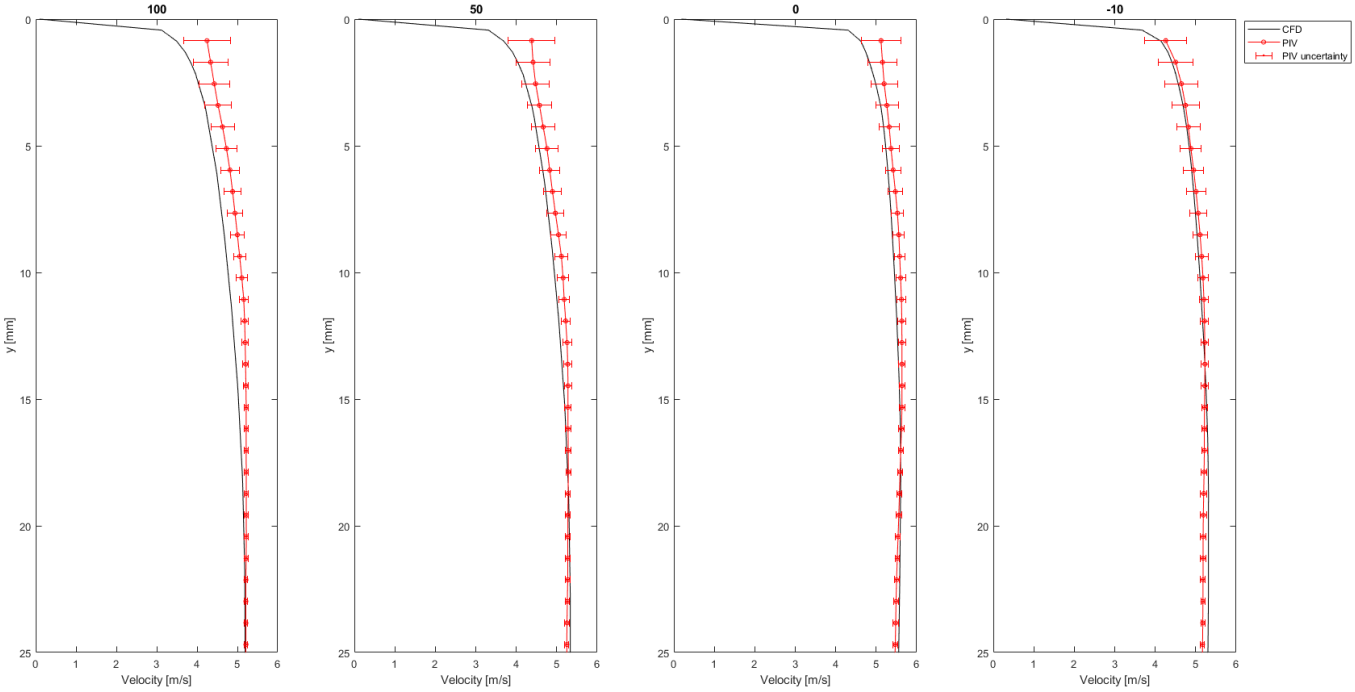

Figure 6.5: Comparison of velocity profile for stern radius 70 mm and a velocity of 5 m/s

The velocity profiles for the 70 mm stern agree better. Only the first 5 mm shows a deviation, but surprisingly, the agreement is the best at the rounded part.

6.3. Flow detachment

The flow separation is determined as described in the method the section 3.3. Tables 6.1 and 6.2 show the determined flow separation points in the CFD and PIV results for the cases with a trim angle of 3 degrees and a velocity of 5 m/s.

Table 6.1: Detachment angles for $v_m = 5$ and $\theta = 3$

	PIV **detachment angle [deg]**	**standard deviation[deg]**	CFD **detachment angle [deg]**
r=50	26.0	1.3	26.6
r=70	24.6	0.9	22.0

Table 6.2: Attachment distance for $v_m = 5$ and $\theta = 3$

	PIV **attachment length [mm]**	**standard deviation [mm]**	CFD **attachment length [mm]]**
r=50	22.7	1.1	23.2
r=70	30.1	1.1	26.9

For the stern radius of 50 mm, there is only a 0.5 mm difference in the detected flow detachment

points, which is smaller than the standard deviation of the detected points in the PIV images. The detachment, according to the CFD, is slightly later. For the radius of 70 mm, there is a difference of 3.2 mm, but in this case the detachment according to CFD is slightly earlier.

7

Conclusions

In this chapter, the research questions will be answered based on the results presented in the previous chapters. The first question is: What is the influence of the following factors on the lift created by a fast ship's diffuser stern?

- Stern shape radius
- Velocity
- Trim angle
- Side-plates
- Oscillations

The highest negative lift is found for the radius of 70 mm, so the negative lift increases with radius. This is beneficial for the total range of lift forces obtained with the interceptor diffuser configuration. It can be concluded that a first improvement in the design of the interceptor diffuser has been made.

The lift coefficient (C_l) decreased with velocity, but the absolute negative lift increases. The absolute drag force obviously also increases with velocity. The drag coefficients showed that the rounded stern of 50 mm slightly reduced that drag for a trim angle of 3 degrees. A drag reduction by the 70 mm stern was only seen for a velocity of 3 m/s, and for the higher velocities only slightly increased the drag.

The other attempt to improve the design was by adding side plates. The side plates decreased the negative lift, so the effect was opposite of the aimed effect. The side plates increase the negative lift for the stern with a 50 mm radius for the higher velocities, so that effect is promising.

The second question to answer is: What are the influence of the flow acceleration and flow detachment on the lift? The resulting flow fields from the PIV measurements show that the flow accelerates due to the rounded stern. The flow accelerates the most under a radius of 70 mm. When looking at the relation between the acceleration and the lift coefficient, it is seen that a higher acceleration correlates with an increase of the negative lift coefficient. But this effect is not to disconnect from the effect of the attachment length.

The flow attachment length decreases with velocity for both stern radii. There is no re-circulation in the flow field close to the rounded stern, so the flow detaches instead of separates. This is beneficial for the negative lift force because a re-circulation area increases the pressure and therewith the resulting lift. The decrease of attachment length with velocity also mean that the effect of the adverse pressure gradient is stronger than the momentum diffusion when the velocity increases. The attachment length is longer for the larger stern radius of 70 mm than for the 50 mm radius. This means that the wetted surface of the 70 mm radius is larger than the wetted surface of the 50 mm radius. A longer attachment length is related to an increase of the negative lift coefficient.

”Suffices the numerical method used for the pre-study in an optimization study of the interceptor diffuser?” is the last question to answer. For the stern of 50 mm, the data of the PIV experiments and numerical study give a good agreement for the lift force and the determined flow detachment points. The velocity profile shows a good agreement from 5 mm from the model, but closest to the hull, the deviation can be attributed to the uncertainty in the PIV results.

For the stern of 70 mm, the determined lift force in the numerical study is significantly lower than the lift force measured in the experiments. This means that according to the numerical method, the stern creates a larger negative lift. A logical explanation would be that the flow’s acceleration in the CFD data is higher or the detachment is later. However, the velocity found in the numerical study is even slightly smaller. The point of flow detachment in the numerical study is earlier than the found separation point in the PIV study. So both findings lead to the opposite conclusion that the found negative lift in the CFD should be smaller than the measured lift. This questions which velocity is relevant for the negative lift. The local velocities of the PIV and CFD results are compared, but the resulting pressure determines the lift. The pressure fields were not examined in this study. Most importantly, the difference in lift force questions the numerical result. The CFD code with the current settings does not suffice for an optimization study since it overpredicts the negative lift. However, the grid convergence study showed no convergence, so a smaller grid may give more accurate results because the lift coefficient decreased with grid refinement. The first step would be to continue reducing the grid size or otherwise tune the settings of the CFD code.

8

Recommendations

Studying the diffuser stern of a fast ship with PIV measurements not only gave insight into the flow field and lift created. The data acquisition during the PIV measurements in combination with force measurements also countered several difficulties, as described in the evaluation in section 3.4. The lessons learned from this experiment lead to the recommendations written in section 8.1. Recommendations regarding further research on a diffuser stern, in general, are described in section 8.2. The last section, section 8.3, makes recommendations for further developing the interceptor diffuser stern configuration.

8.1. Regarding PIV experiments

A first and straightforward recommendation for PIV experiments in the towing tank is to put three clear markings on the model to define its position. Multiple points are needed to distinguish possible vibrations in all directions. The processing is easier if the marking is not in the background of the flowfield in any measuring position because it prevents unnecessary background filtering in the data processing. It is recommended to use more than one laser distance measurer to check the position and motions of the model or use another method to measure the position.

It would be even better to prevent or decrease the displacement and vibrations caused by the elastic deformation of the force sensors. The force measurements could be done separately from the PIV measurements to eliminate the displacement and reduce the vibrations of the model. However, this brings the uncertainty that it is unknown whether the circumstances were the same. Decreasing the displacement and vibrations can also be achieved by using force sensors with a higher capacity. The force sensors work elastically, and in this study, the force sensors' total capacity is used. The consequence is that the full elastic deformation range of the force sensor is used. A force sensor with a higher capacity will deform less, so the model's displacement would be smaller. Also, the force measurement frame could be mounted further to the stern to decrease the pitch moment on the force frame.

The most severe limitations in using the data were caused by the reflections, leading to large areas in pictures that were unusable. The angle between the laser light and the free surface was small, which leads to total internal reflection. The turbulent behavior makes the reflection even worse because bubbles reflections give very high-intensity areas where the particles are not visible.

For measuring an x-z plane, theoretically seen it is also possible to place the PIV laser below or above the measurement plane. Placing the laser below the model has the practical limitation that the laser must be towed, so mounting the laser to the towing carriage seems impossible. Placing the laser above the measurement plane means that an acrylic model bottom is needed. This is a solution that has proven to give data of good quality. However, for a rounded stern, the acrylic glass should have been bend. A high angle of incidence of the laser light on the bend acrylic glass also causes reflections. The reflection of the laser light on a bend acrylic glass, or acrylic glass under an angle, could be tested in a test- setup to research the option.

Another option would be to use fluorescent particles, which are much easier to distinguish from bubbles. However, the drawbacks regarding the price and environmental and health consequences have to be taken into account.

8.2. Regarding further research

A first recommendation is to make a pressure reconstruction from the obtained velocity fields. The local velocities were known, but the resulting pressure is what finally determines the negative lift force. That will give the possibility to distinguish the effect of the flow acceleration and attachment.

A more fundamental approach can be taken by comparing the found detachment point to flow separation point predictions in other experimental studies. As described in the literature chapter, several coefficients have been used to determine a flow separation point.

Also, a basic setup could be used. The tested situation made it difficult to predict theoretical boundary layer development. The situation with the model's bow, transition in the bottom, and trim angle is far from ideal, making it difficult to distinguish effects from each other. Comparing a theoretical boundary layer and an observed boundary layer is complex when the theoretical boundary layer can not be predicted accurately. The effect of the free surface on the flow detachment can be distinguished better if the situation is similar to a flat plate with a rounded end. Also, the stern depth could have its influence but was out of the scope of this study.

8.3. Regarding the development of the interceptor diffuser

The recommended first step is to improve the agreement between the resulting lift force found in the measurements and the CFD study to develop the interceptor diffuser. As mentioned before, the grid convergence study showed that the resulting force did not converge yet. So a finer grid may give a more accurate result. Eventually, another method could be tried as well.

Optimizing the diffuser shape is next if a good agreement between the numerical method and the measured forces is found. This can be done from a hydrodynamical perspective, optimizing for the maximum negative lift. Two variables recommended to vary are the stern radius and the start point of the curvature. The optimum stern radius for the current model is expected to be 70 mm or larger. Also, a varying curvature like a parabolic shape could be tried. For the radius of 70 mm, the curvature was started 50 mm from the transom. Since the flow detachment was always earlier than the transom, the start point of the curvature could be closer to the transom. A larger stern radius may need an earlier start point of the curvature to fully use the low-pressure area because the flow attachment length is expected to be larger.

Another addition to the design could be a turbulence-increasing device, like vortex generators. This idea comes from the differences between the measurements of Rijkens et al. [2013] and the measurements of this study. The transition in the bottom close to the rounded part in the previous

measurements may have lead to the higher negative lift coefficient. Vortex generators could have a similar effect.

The consequences for the implementation in the entire ship design can also be taken into account. Different shapes result in differences in the space for systems in the stern, like the propulsion system.

A

Introduction into Particle image velocimetry (PIV) in a towing tank

This appendix introduces the chosen method. In section A.1, it is explained what PIV is and which steps are taken in a PIV experiment. The aim is to make it possible to understand the choices made for the design of the experiments for someone who is not familiar with PIV yet. Because it will finally be applied in a towing tank, previously performed PIV experiments in towing tanks outside and at the TU Delft are discussed (A.2). Using PIV in the towing tank comes with several difficulties in the application. With an eye on the experimental setup that has to be designed, the difficulties are explained.

A.1. PIV principles

Particle image velocimetry is a method to obtain the velocity field of a flow. With images of particles in a fluid, the velocity of the fluid at a time instant can be found. The particles are captured on an image by seeding the flow with the particles and illuminating them with a laser sheet. The images are split into so-called interrogation areas. The velocity is determined with the displacement of the particles in an interrogation area between instant t and $t + dt$. The velocity vectors of the interrogation areas together give the flow field. Figure A.1 gives an overview of this principle.

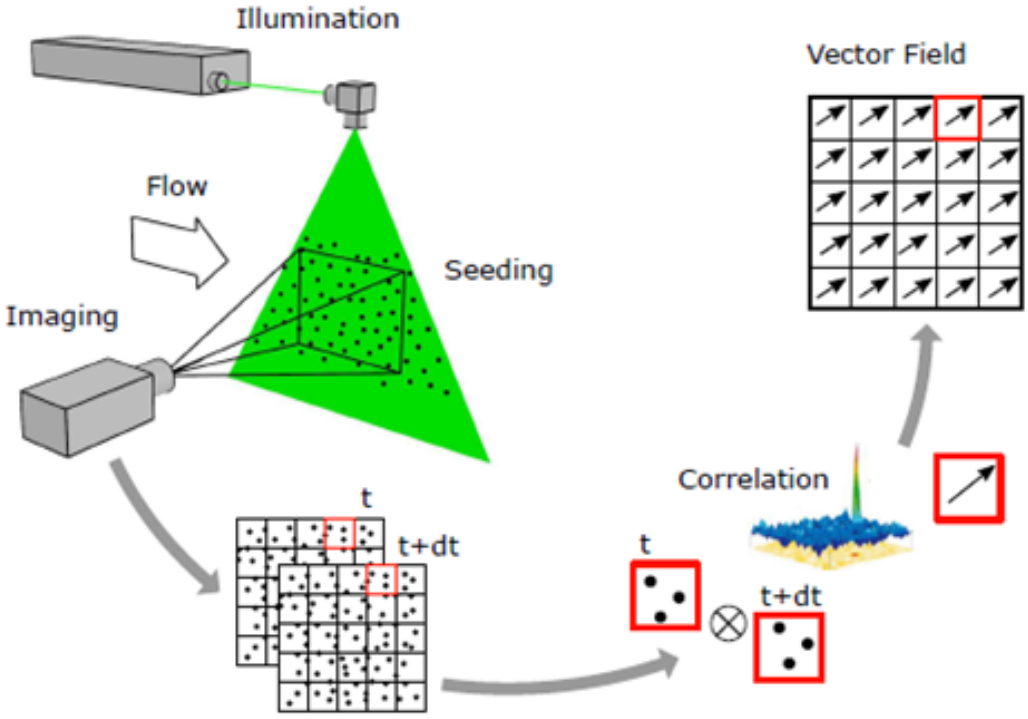

Figure A.1: Overview of PIV principle

Statistical analysis can be done to a set of images for unsteady flows. Enough pictures have to be taken to get a good flow field. The flow field can be used to reconstruct the pressure distribution.

Steps in PIV experiments

1. Configuration

At first, the configuration has to be designed. This depends mainly on the part of the flow that will be visualized and the main flow direction. In the case of a 2D flow, it is obvious to take the 2D plane. In the case of a 3D flow, the chosen plane depends on the two most important velocity components to measure. For the positioning of lasers and cameras, there will always be multiple options. All have their advantages and drawbacks regarding reflections, the accuracy of the out-of-plane velocity, and the field of view, so a trade-off must be made.

2. Calibration and the use of disparity

The system has to be calibrated by putting the cameras in the right position, at the right angle, and making the mapping functions. This translates the object plane to the image plane, as shown in figure A.2. This is done by using a calibration plate. The goal is to make sure both cameras make the same image after applying a mapping function as in figure A.3. If both cameras do not make the same image, the mapping function has to be corrected.

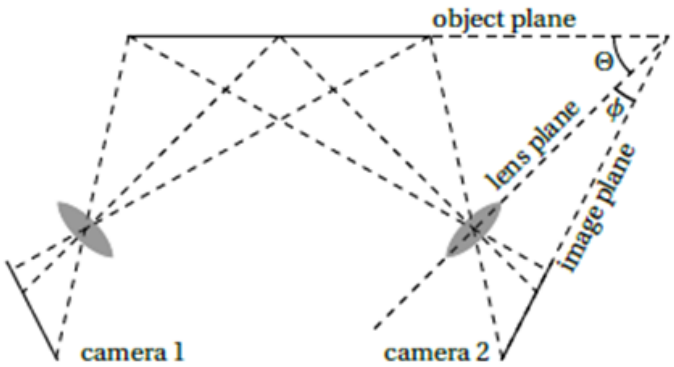

Figure A.2: From object to image plane in stereo PIV setup Jacobi [2020]

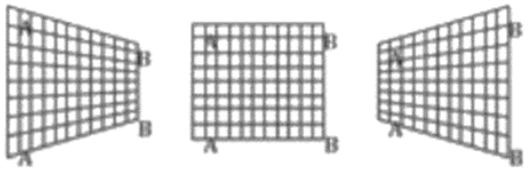

Figure A.3: Visualized goal of the mapping function

The calibration is done by placing a calibration board in the position of the plane to measure. Depending on the camera positions, a 1 or 2-sided calibration board is used. A disparity map is used if the calibration board is not perfectly aligned with the laser sheet (at the top of figure A.4). A disparity map uses the cross-correlation between the two images to correct for the registration error.

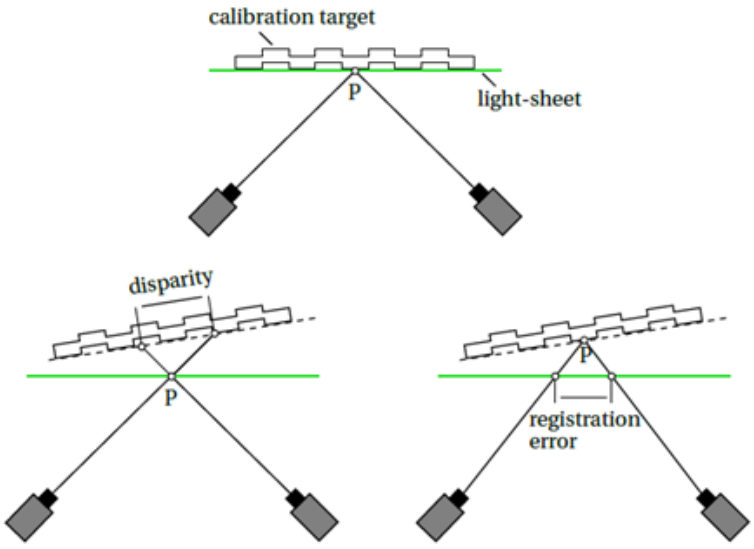

Figure A.4: Disparity and registration error in calibration Jacobi [2020]

3.Obtaining the images

a. Seeding:

The water is seeded with particles that scatter the laser's light, which will be captured in the pictures. The particles have to be mixed well with the fluid to get particles distributed. The type and size of the particles have to be chosen. Different types have different buoyancy properties and scattering properties that depend on size, shape, and orientation. Too big particles have the disadvantage that they do not follow the flow well. Too small particles have the disadvantage of being visible because they do not scatter enough light.

b. Illumination

A laser sheet illuminates the seeding particles. The reason for using laser light is that chromatic aberrations cannot occur when directing the source to a sheet. The laser gives double pulses. One pulse must be such short that the image is frozen. The time between the pulses is determining the quality of the results. If the time step is too short, the displacement of the particles is too small to determine the displacement. If the time step is too long, too many particles may have moved out of the illuminated sheet. A maximum of 1/3 of the particles may be lost when comparing one picture to the next (Adrian et al. [2011]). When the flow velocity component perpendicular to the laser sheet is big, this is a challenge. A higher flow velocity requires a shorter illumination and shorter time between pulses. The intensity of the laser is also important because a higher energy per pulse makes it possible to use smaller particles that still scatter enough light.

c. Imaging

For stereo PIV, two cameras are used. The frequency is important because it determines how many captures can be taken in one run. A higher frequency (till a limit) increases the efficiency of the experimental time. The cameras' specifications and the distance of the cameras to the illuminated plane determine the field of view size. This determines how detailed the flow visualization is and must be known for choosing the seeding particle size.

4. Process data

a. Image processing

The hull shape and free surface must be excluded, so only the particles are left on the image.

b. Displacement interrogation

The field is divided into interrogation areas which size can be optimized for the best results. Per interrogation area, a cross-correlation is obtained to find the displacement. With this displacement, the velocity can be determined using the time step between the images:

$$v = \frac{ds}{dt} \tag{A.1}$$

The result is an instantaneous velocity vector per interrogation area. Stereo imaging makes it possible to visualize 3 velocity components in a plane. The principle is shown in figure A.5. With the velocities captured by both cameras at one position and the exact angle of the cameras, the out-of-plane velocity component can be calculated. The accuracy of this velocity depends on the camera angles.

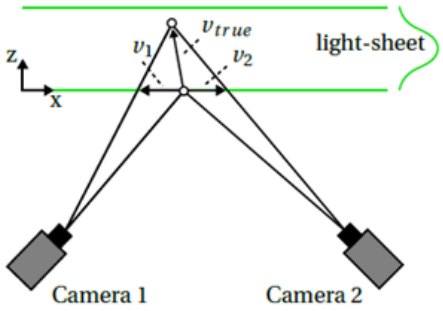

Figure A.5: Obtaining the out of plane velocity component in stereo PIV Jacobi [2020]

A.2. PIV in a towing tank: state of the art

The first time PIV was applied in a towing tank, the structure of a bow wave was researched by Dong et al. [1997]. His findings of seeding were directly applied by Pogozelski et al. [1997] to look at the flow structure around a surface piercing strut. 2D vectors could be obtained in the illuminated plane because 1 camera was used. In these experiments, the PIV system was moved with the system. 2D measurements with one camera have also been applied stationary by Tukker et al. [2000].

From 2003, it became evident to use a second camera to obtain 3 velocity components in a 2D plane. Pereira et al. [2003] is the first example and focuses on the design of the probe for holding the two cameras. With a few exceptions, a probe for holding the cameras has become the standard. For a 3D flow field, a third (and fourth) camera can be used. Egeberg et al. [2014] has applied such a tomographic setup.

PIV experiments in towing tanks are mainly used to look at wakefields. Examples are the experiments of Gui et al. [2001], Pereira et al. [2003], Anschau and Mach [2007], Longo et al. [2007], Seo et al. [2016] and Guo et al. [2018]. Examples of maneuvering tests are the study of Falchi et al. [2013] about the steady drift of catamaran and a similar one by Falchi et al. [2014].

At the TU Delft towing tank facility, Jacobi [2020] applied PIV for investigating the hydrodynamics of fast ships. While all other mentioned experiments were done at low speeds, this research is focused on fast ships. The main new challenges due to the velocity were the structural vibrations and large out-of-plane velocities.

The PIV system is applied for the analysis of the hydrodynamics of a conventional interceptor. There were two different setups shown in figure A.6 and A.7.

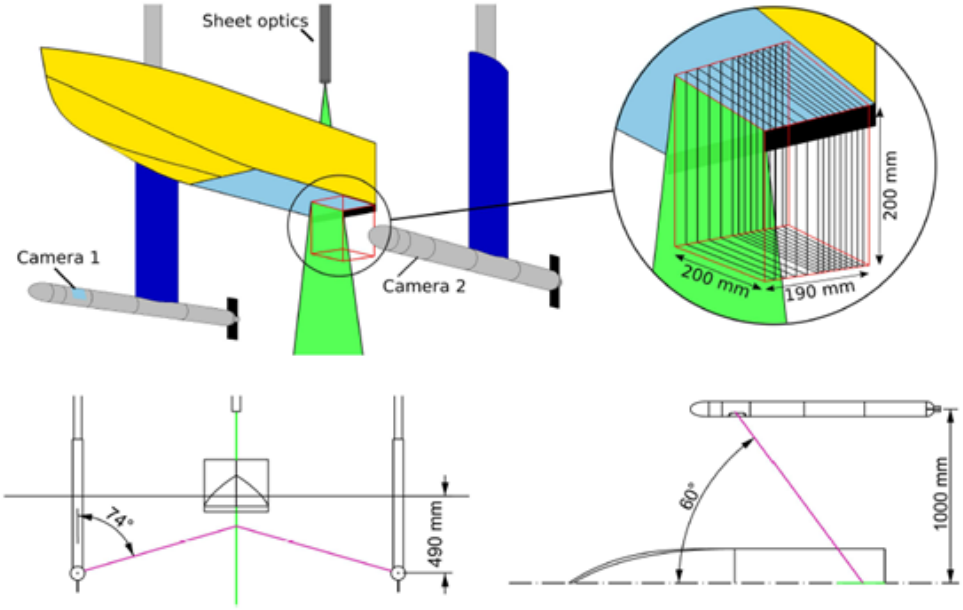

Figure A.6: Setup 1A

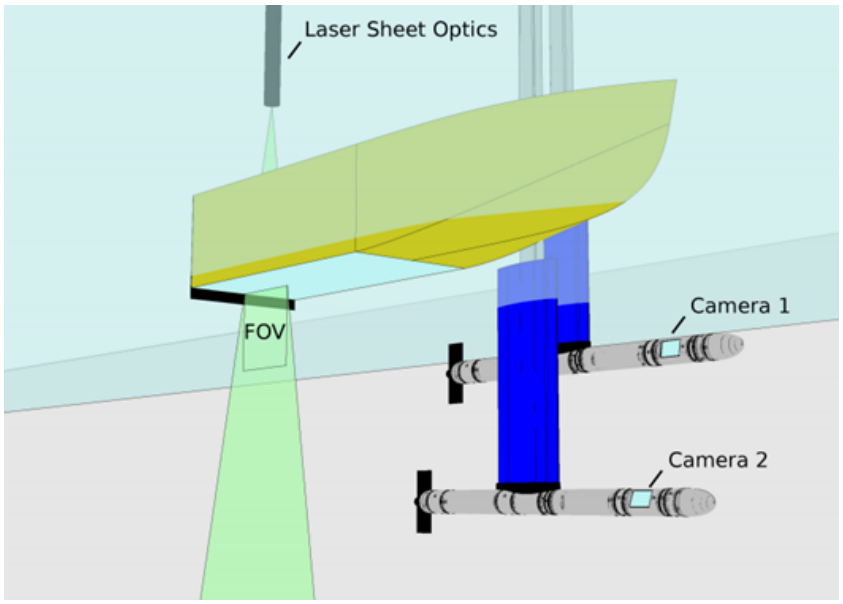

Figure A.7: Setup 1B

Another application was to find the pressure in the bow region of a fast ship. The measurement plane was perpendicular to the main flow direction, as in the setup shown in figure A.8. The large out-of-plane velocity was a new challenge. The setup succeeded in obtaining results similar to the results of RANS simulations. The difficulty was the analysis of the images because of the reflections. Besides knowledge about the flow around an interceptor, there were two other goals. Namely to find to what extend the images are affected by vibrations and if a correction procedure is necessary, and to compare the results to RANS simulation results to study the potential of the pressure reconstruction of PIV measurements. A correction procedure is proposed, which starts with self-calibration. The

individual cameras are corrected by comparing the images with respect to the first image of a data set. Afterward, the data of both cameras are recombined, and the common disparity correction is done. About the pressure reconstruction is concluded that there is a good agreement with RANS results, but peak pressures are overestimated.

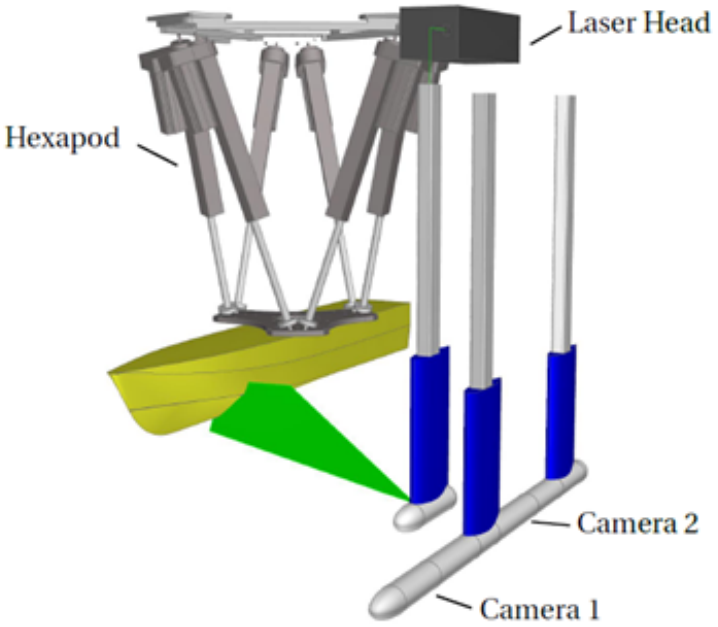

Figure A.8: Setup 2

An overview of the specifications of the used equipment is added in table A.1.

	setup 1	Setup 2
Laser type	Litron Bernoulli Nd:YAG laser 200mJ/pulse 532 nm	Litrion Nano PIV Nd:YAG laser 50 mJ/pulse 532 nm
Camera's	2x La Vision Imager Pro SX 2448x2050 pixels, 12 bit colour depth	2x La Vision Imager MX 4M 2048x2048 pixels, 10 bit colour depth
Field of view	200x200 mm2 XZ plane Forward scatter, 2 torpedo's	250x250 mm2 YZ plane Backscatter, 1 torpedo
Resolution	About 10 pixels/mm	About 7x7 pixels mm2
Images	Double frame acquisition rate 7Hz 120-210 per run (depending on speed)	Double frame acquisition rate 75Hz But due to laser 50 Hz max
Seeding particles	50 μm polymer (Vestosint)	50 μm polymer (Vestosint)
Calibration		320x320 mm2 calibration plate

Table A.1: Overview of specifications of used equipment

A seeding system is placed at the front of the carriage, shown in figure A.9. This is used to mix the particles and seed the water in between test runs. Preferred types of particles in the towing tank

are slightly negatively buoyant, so they sink, and the bottom can be cleaned.

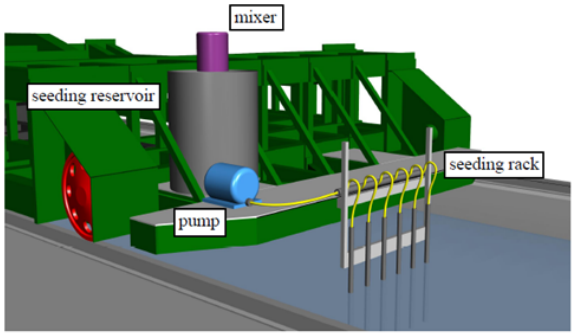

Figure A.9: Seeding system in TU towing tankJacobi [2020]

A.3. Difficulties in applying PIV in a towing tank

1. Calibration and alignment

There are two difficulties related to calibration and alignment: the alignment of the light sheet with the model and the alignment of the calibration plate.

2. Vibrations

Vibrations of the measuring system and/or model increase at higher velocities can lead to images that differ because of the camera's movement with respect to the measurement plane instead of the movement of the particles. Differences between the two cameras can be reduced by putting both cameras in one strut so that if the cameras move, they both move. Another way to reduce the vibrations is to reduce the length of the camera holding torpedo hull(s). The influence of vibrations that still occur can be reduced by the correction procedure proposed by Jacobi [2020].

3. Reflections

a. Reflection of the model

When the laser is projected on the flow from outside the model onto the model, the model will reflect the light. When the laser is placed on the inside, acrylic glass can be used. However, it has to be taken into account that acrylic glass also can reflect the light depending on the angle of incidence. When the laser is placed outside the model, there are different ways to reduce the reflections. Matt black and fluorescent painted models have been used to absorb the full spectrum or reflect a specific wavelength by using a narrow band-pass filter. The results with fluorescent paint in the towing tank so far have not been satisfying. Matt black is currently the best option for measurements with the laser from the outside, but there will still be reflections that hinder the visibility of the particles.

b. Bubbles

Bubbles reflect the laser light. They have to be distinguished from the scattering particles. Fluorescent particles can be easier distinguished from bubbles, but these are usually expensive and can cause health problems. Pedocchi et al. [2008] proposed a fluorescent seeding particle type that is cheap enough to use in large facilities like a towing tank.

c. Free Surface

Finding the free surface will be important in this research because it is expected that the point where the free surface detaches influences the amount of negative lift. However, it is not easy to find the free surfaces in the images because of reflections. A solution used by Pogozelski et al. [1997] is to add aluminum powder to make it easier to detect the free surface. However, it is questionable whether

it is allowed to use this in the TU Delft facility due to possible problems with cleaning the water or health issues.

4. Time for experiments

The experiments are time-consuming. Building the setup costs more time than an average towing tank experiment because of all the extra components. The calibration needs to be done extensively. Also, between every run, a waiting time of 25 minutes is required. This has to be taken into account in the planning.

B

Fundamental theory and literature about boundary layers and flow separation

B.1. Turbulent boundary layer theory

A turbulent boundary layer can be divided into an inner - and outer layer. The inner layer can be subdivided into the viscous sublayer, the buffer layer, and the overlap layer. The overlap layer is also part of the outer layer together with the wake region. A visual representation of the layers is given in figure B.1. The velocity profile in the boundary layer depends on the free stream velocity and the shear stress with a laminar and turbulent part. The viscous shear stress is dominant in the viscous sublayer, and the turbulent shear stress can be neglected. From the buffer layer both parts become important. The same holds for the overlap layer, but the turbulent shear stress becomes dominant. In the outer layer, the laminar shear stress is negligible.

		Shear stress	Y+	Law
Inner layer	Viscous sublayer	τ_turbulent negligible	Y+<5	Law of the wall
	Buffer layer	τ_laminar and τ_turbulent both important	5<y+<30	
	Overlap layer	τ_laminar and τ_turbulent both important but τ_turbulent is dominant	30<y+<500	Logarithmic law
Outer layer		τ_laminar negligible	500<y+<10000	Velocity defect law

Figure B.1: Overview of the boundary layer structure

There are multiple analytical approaches for the velocity profile that give a good representation of real boundary layers. Three of them will be shortly explained. The logarithmic law gives a good representation of the velocity profile in the overlap layer. The following steps are used to calculate the velocities (Newman [2018], Khademi et al. [2010]).

$$Cf_x = \frac{0.0577}{Re^{(1/5)}} \tag{B.1}$$

$$\tau_w = Cf_x \cdot 0.5 \cdot \rho \cdot u0^2 \tag{B.2}$$

$$u* = \sqrt{\frac{\tau_w}{\rho}} \tag{B.3}$$

$$y+ = \frac{y \cdot u*}{\nu} \tag{B.4}$$

$$u = (\frac{1}{k} ln(y+) + 5) \cdot u0 \tag{B.5}$$

The one-seventh power law is an empirical model with less scientific support. Still, it is a simple model that shows a good agreement with measured velocities in the overlap layer.

$$\delta = 0.373 \cdot xL \cdot Rex^{-\frac{1}{5}} \tag{B.6}$$

$$u = (\frac{y}{\delta})^{\frac{1}{7}} u0 \tag{B.7}$$

Coles law is a modified version of the logarithmic law for the defect layer Coles [1956]. Coles wake parameter Π is a function of the pressure gradient. It corrects for the underprediction of the

logarithmic law in the defect layer, although that is still a proper estimation.

$$\eta = \frac{y}{\delta} \tag{B.8}$$

$$f(\eta) = sin^2\frac{\pi}{2}\eta \tag{B.9}$$

$$u = ((\frac{1}{k}ln(y+) + 5)\frac{2\Pi}{k}f(y/\delta))u0 \tag{B.10}$$

B.2. Principle of flow separation

At a sharp edge, the flow is forced to separate, but in the case of a curve, the flow tries to follow it. However, it encounters a positive (so adverse) pressure gradient, as shown at the right side of figure B.2 ($dp/dx > 0$), which can also lead to flow separation. In this section, it will be explained how.

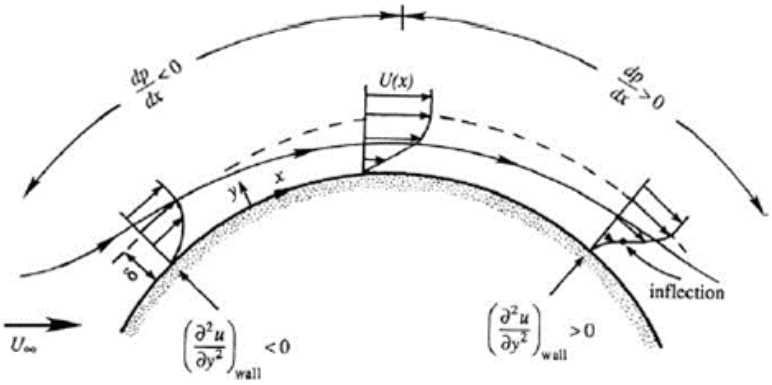

Figure B.2: Velocity profile in the boundary layer with pressure gradient Kundu et al. [2016]

The adverse pressure gradient slows the flow down, but the momentum diffusion from the free stream gives a streamwise momentum, so these forces work against each other. How big the free stream's momentum is, depends on the viscosity, the velocity of the free stream, and whether the flow is turbulent. An inflection point in the velocity profile occurs when the flow at the surface is slowed down, as shown in figure B.3. When the velocity gradient perpendicular to the wall is 0 at $y = 0$, the flow separates (So $dp/dy_{@y=0} = 0$). Behind this separation point, a reverse flow occurs. This effect is important because the pressure increases after the separation point, and an early flow separation reduces the surface area on which a lower pressure acts.

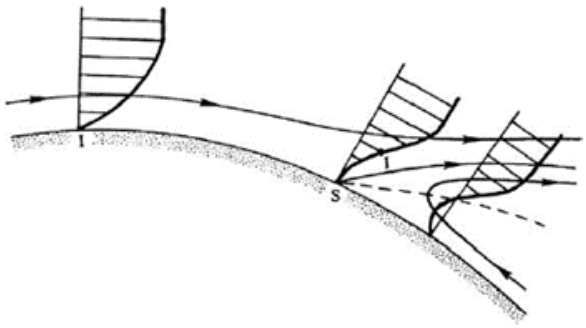

Figure B.3: Flow separation principle Kundu et al. [2016]

A turbulent flow delays the flow separation because the velocity at the surface is higher, so

the momentum is bigger. The difference in the velocity profile between a laminar and turbulent flow is shown in figure B.4. Although this increases the viscous drag, it is an advantage because it takes longer to slow the flow down until an inflection point occurs and the flow separates.

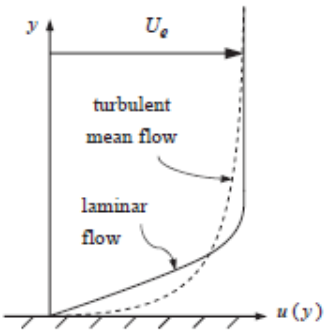

Figure B.4: Laminar and turbulent boundary layer velocity profile Kundu et al. [2016]

Besides making the flow turbulent, there are several other ways to delay flow separation, such as applying vortex creators to help the flow stay attached, jets to increase the momentum of the flow, or suction to decrease the pressure gradient.

B.3. Determining flow separation points

A general applied rule is that flow separation occurs at the point where the wall shear stress is zero. To calculate the wall shear stress, the velocity distribution in the boundary layer has to be known. A basis for many theories to predict flow separation is the momentum equation derived by Von Karman, with which the wall shear can be calculated. (equation B.11). This equation is valid for laminar and time-averaged turbulent boundary layers.

$$\frac{1}{\rho}\tau_w = \frac{d}{dx}(u^2\theta) + \delta^* u\frac{du}{dx} \tag{B.11}$$

The following parameters have to be known. The thickness of the boundary layer is named δ. At the edge, the velocity is equal to the free-stream velocity. This parameter is necessary to calculate the parameters displacement thickness (δ^*) and the momentum thickness (θ). Equations B.12 and B.13, respectively, show how these values are defined. The displacement thickness is the distance that the boundary has to be displaced to have the same resulting mass flux if the velocity was u_0 over the whole layer. The momentum thickness is the distance that the boundary has to be displaced to have the same momentum flux if the velocity was u_0 over the whole layer.

$$\delta_* = \int_0^\delta (1 - \frac{u}{u_0})dy \tag{B.12}$$

$$\theta = \int_0^\delta \frac{u}{u_0}(1 - \frac{u}{u_0})dy \tag{B.13}$$

Theoretically seen, these could be found analytically with the expressions for velocity profiles.

Granvlle [1951] describes in his paper different methods to better predict the variation of the pressure gradient with the Von Karman momentum equation as a basis. Different approaches for

determining the wall shear stress are used in these methods, resulting in different criteria for the separation point. A list of separation criteria is shown in figure B.5. In the period where these criteria were determined, all work was based on experimental data.

Summary of Methods for Calculating the Turbulent Boundary Layer in a Pressure Gradient

Investigator	Criterion for Separation	Auxiliary Equation (for use with von Kármán Momentum Equation)	Remarks
Buri, 1931 Reference 9	$\Gamma = -0.06$	None explicitly; von Kármán momentum equation modified to $\frac{d}{dx}(R_\theta^{\frac{1}{4}}\theta) = a - b\Gamma$ [19]	Γ is not proper parameter for shape of velocity profile; no allowance in method for effect of previous development of flow in boundary layer
Gruschwitz, 1931 Reference 5	$\eta \geq 0.8$	$-\frac{\theta}{U^2}\frac{d(U^2\eta)}{dx} = 0.00894\eta - 0.00461$ [20]	No Reynolds-number effect included; based on test data, $1 \times 10^3 < R_\theta < 4 \times 10^3$
Kehl, 1943 Reference 6		$-\frac{\theta}{U^2}\frac{d(U^2\eta)}{dx} = 0.00894\eta - \frac{0.0164}{\log_{10} R_\theta} + \frac{0.85}{(R_\theta - 300)}$ [21]	Gruschwitz method extended to include effects of Reynolds number; based on test data $1 \times 10^3 \leq R_\theta \leq 3.5 \times 10^4$
von Doenhoff and Tetervin, 1943, Reference 7	$1.8 < H < 2.6$	$\theta\frac{dH}{dx} = \left[-2.035(H - 1.286) + \frac{2}{\rho U^2}\left(\theta\frac{dU}{dx}\right)\right]e^{4.655(H-2.975)}$ [22] $\frac{\tau_w}{\rho U^2} = \left[\frac{1}{5.890\log_{10}(4.075 R_\theta)}\right]^2$ [23]	Empirical; based on test data, $1 \times 10^3 < R_\theta < 7 \times 10^4$
Garner, 1944 Reference 12	$H = 2.6$	$\theta\frac{dH}{dx} = \left[\frac{0.0135(H-1.4)}{R_\theta^{1/6}} - \frac{\theta}{U}\frac{dU}{dx}\right]e^{5(H-1.4)}$ [24]	Based mostly on same data as von Doenhoff and Tetervin
Tetervin and Lin, 1950, Reference 15		$\theta\frac{dH}{dx} = \frac{H(H+1)(H^2-1)}{2}\frac{\theta}{U}\frac{dU}{dx} + H(H^2-1)\frac{\tau_w}{\rho U^2} - (H+1)(H^2-1)\int_0^1 \frac{\tau}{\rho U^2} d\left(\frac{y}{\delta}\right)$ [27]	Theoretically derived but lacking in shearing-stress information required for numerical solution

Figure B.5: Listed methods for turbulent boundary layer calculation by Granvlle [1951]

Chang [2014] describes in his book multiple criteria for flow separation in an incompressible external turbulent flow. He distinguishes between internal and external flow because, for internal flows, the wall has a stabilizing effect, although the differences between internal and external flows are not well understood. Some criteria described by Granvlle [1951] come back in this book, namely Buri's, Gruschwitz's, Doenhof and Tetervin's, and Garner's criteria. Two described new methods, Rotta's and Ross. Rotta [1951] uses a refinement of the law of the wall. An initial shape factor H has to be chosen and iteratively the separation point can be found. Ross [1953] use the 3 zones of the boundary layer. He developed a relatively simple procedure with an algebraic equation. A parameter often comes up is the dimensionless number H, the shape parameter.

$$H = \frac{\delta}{\theta} \tag{B.14}$$

Since all cases were in situations without a free surface, a parameter like this makes it interesting to determine whether existing criteria also apply for a case with a free surface.

What becomes clear in all methods is that experimental data is used, and a prediction without any pressure data will become inaccurate. In the case of a turbulent flow, it just isn't possible to solve the boundary layer equations analytically. Cebeci et al. [1972] compare four different methods for the calculation of separation points in incompressible turbulent flow: Head's, Stratford's Goldschmied's and the CS(Cebeci-Smith) method. All of them require numerical pre-calculations for the pressure coefficient. A BEM code can be used to obtain these pressure coefficients. They compare the outcomes with experimental results for different geometric shapes.

The conclusion is that Goldschmied's method is inconclusive; the CS method predicts the point in some cases better than Head's method, and Stratford's method can be conservative. However, Stratford's method is the most user-friendly method for calculations.

Patel [2014] used the pressure coefficients of a panel method as input for Stratford's turbulent method to find the flow separation point. The following procedure was implemented in MATLAB.

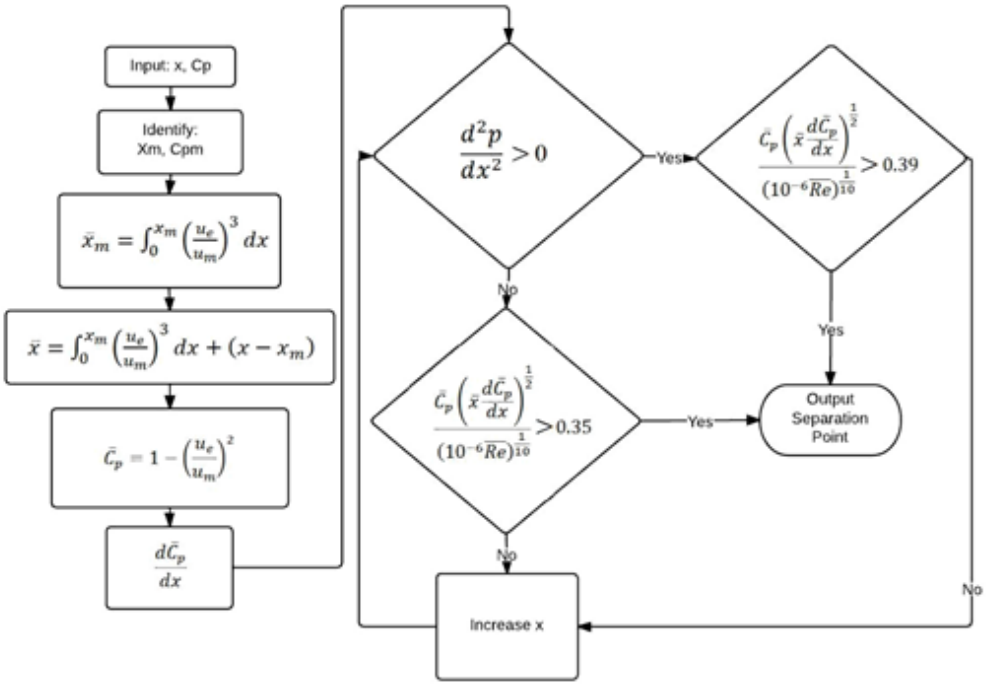

Figure B.6: Matlab procedure for Stratford's turbulent method to determine the flow separation point

C

Additional results of previous interceptor diffuser study

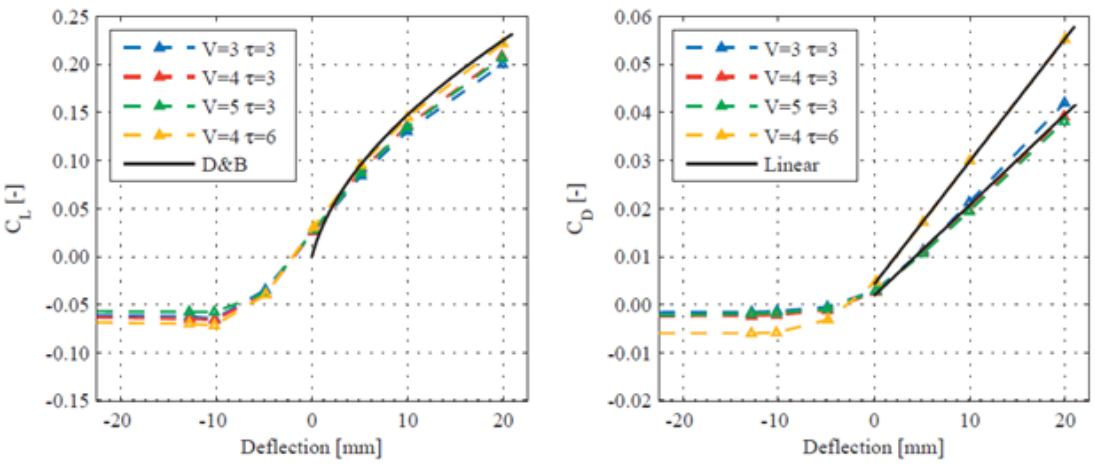

Figure C.1: Results of full span interceptor diffuser r=25 mm Cleijsen [2013]

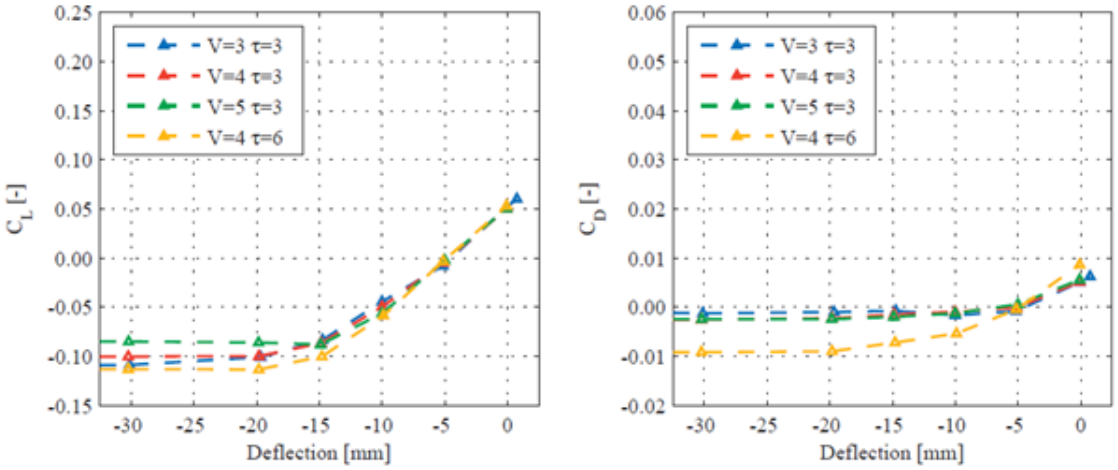

Figure C.2: Results of full span interceptor diffuser r=50 mm Cleijsen [2013]

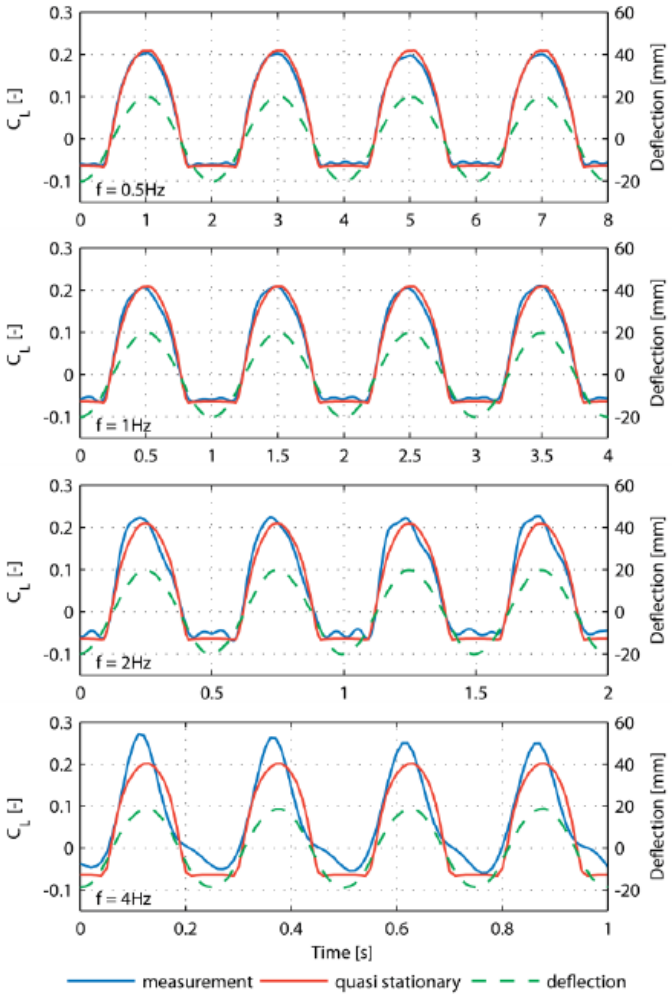

Figure C.3: Results of harmonic oscillation experiments at frequencies 0.5, 1.0, 2.0 and 4.0 Hz with the interceptor diffuser Rijkens et al. [2013]

D

Specifications of setup components

D.1. Towing tank

Width	4.22 m
Depth	2.5 m
Length	142 m
max speed	7 m/s
NOTUS hexapod	linear travel range +- 250 mm

D.2. Model

Loa	1.75 m
Draft	50 mm
Trim	3 deg
Lwl	1.52 m

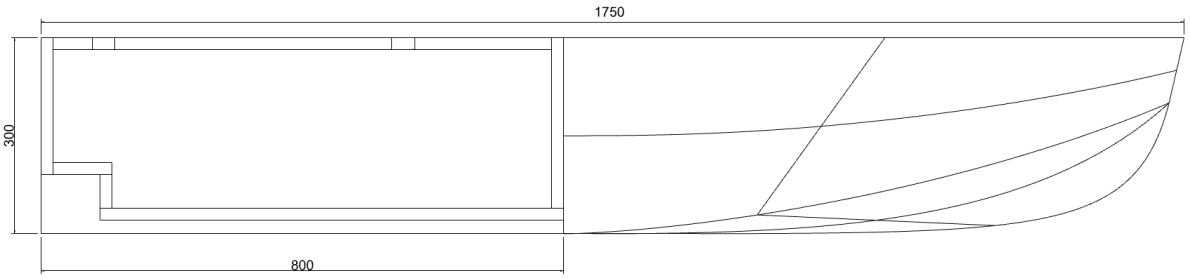

Figure D.1: Side view of model

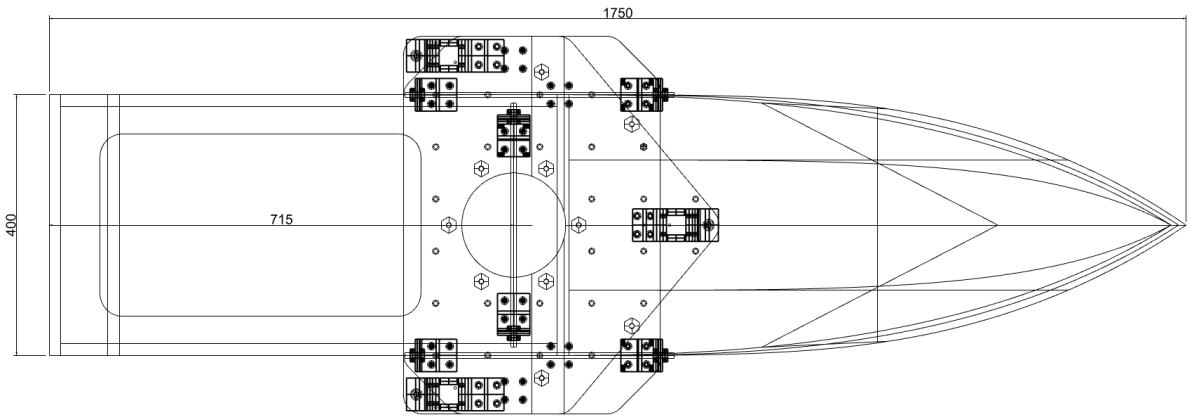

Figure D.2: Top view of model with force frame

D.3. Force measurement frame

The 6 degree of freedom force frame (figure D.3) uses 2 force sensors for the x-direction, 1 for the y-direction and 3 for the z-direction. Each force sensor is calibrated individually and the alignment of the total frame is checked. With the measured forces, the resulting hydrodynamic lift and drag force on the model can be calculated. Using the measured moments, the point of engagement can be calculated as well.

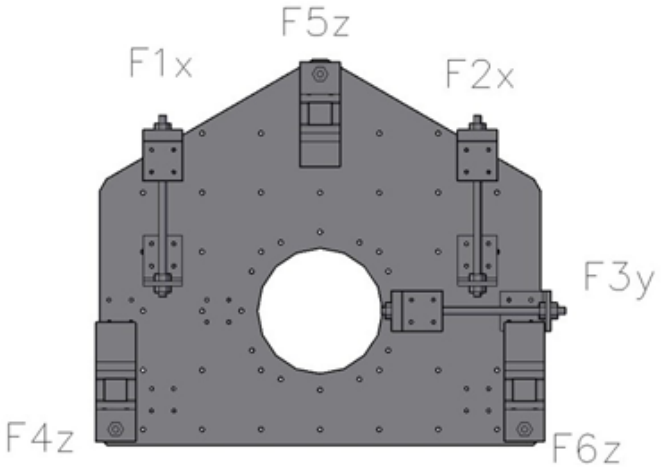

Figure D.3: 6DOF force measurement frame

D.4. Hexapod

To place the model in the right draft and trim angle, move it in y-direction and to make the pitch motions, the model with the 6DOF frame was mounted to a NOTUS hexapod.

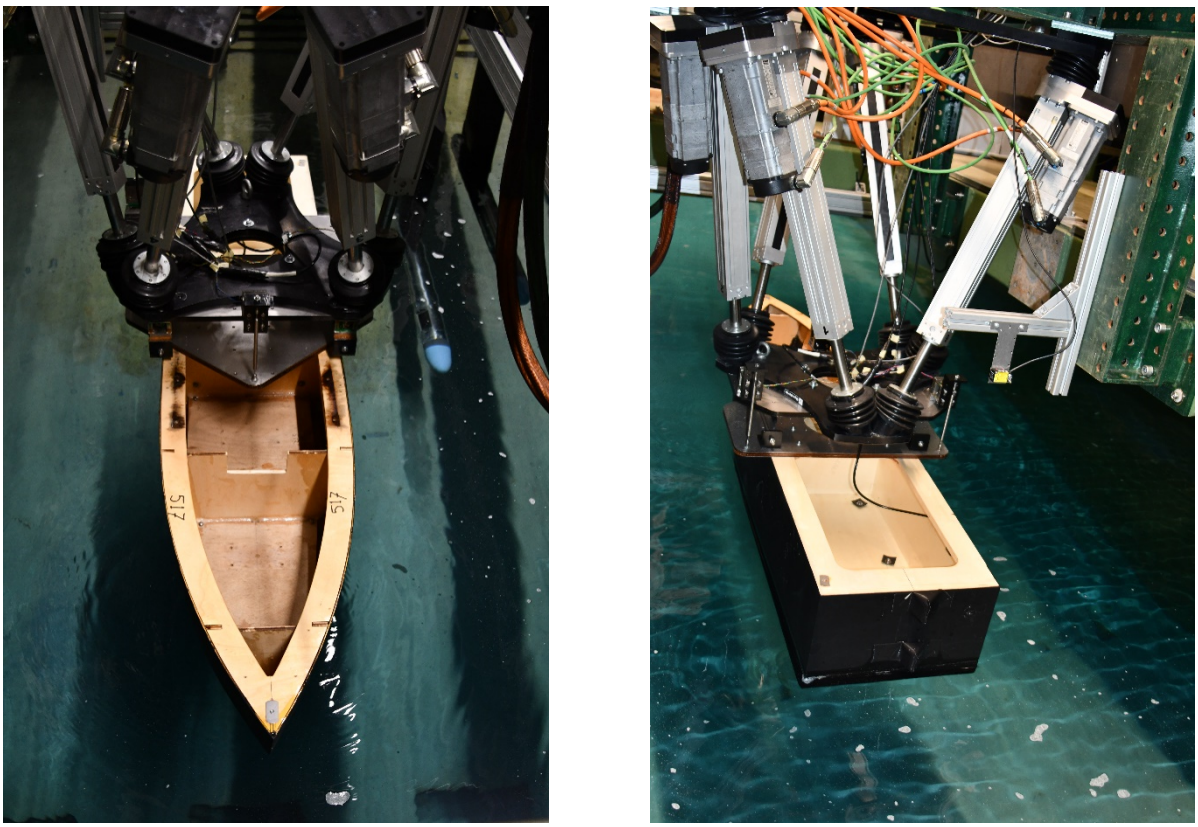

(a) (b)

Figure D.4: Photo model with force frame, hexapod and laser distance measurer

D.5. Cameras specifications

2048*2048 pixels
10 bit color depth
75 Hz double frame acquisition rate (due to laser 50 Hz)
28 mm f/1.8 lenses
1:2 aperture ratio
65 $\mathtt{deg}$ horizontal viewing angle
46 $\mathtt{deg}$ vertical viewing angle

Table D.1: Camera specifications

D.6. Seeding

The same seeding rack as shown in section A.2 is used. For the chosen time step there has to be a seeding density of about $8.1677e+06$ particles per cubic meter. This corresponds with $4.3gram$ of the $50\mu m$ Vestosint particles. In practice, 1 liter of particles was seeded in the begin of the day and 250 ml of particles were added after every run.

D.7. Final setup additional drawings and photos

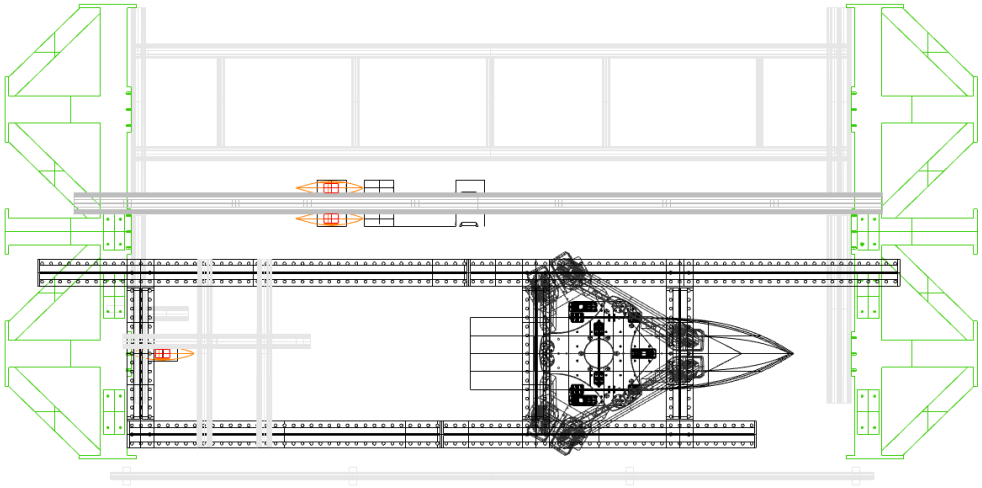

Figure D.5: Setup top view

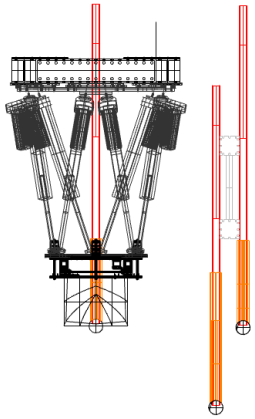

Figure D.6: Setup back view

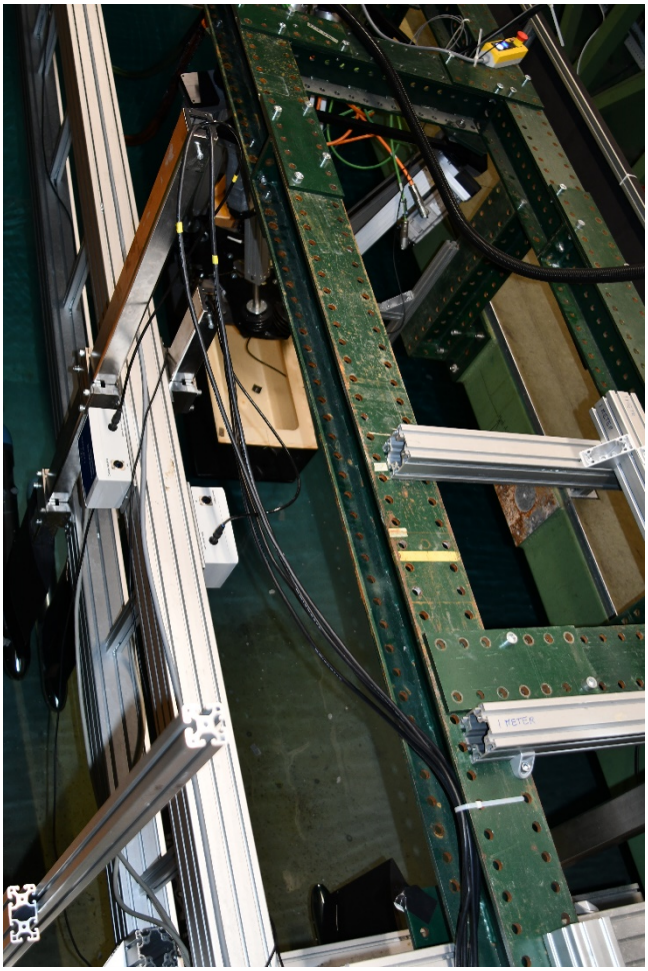

Figure D.7: Photo of PIV setup: model, camera struts, laser tube

E

Additional results: flow fields and boundary layer

E.1. Flow fields

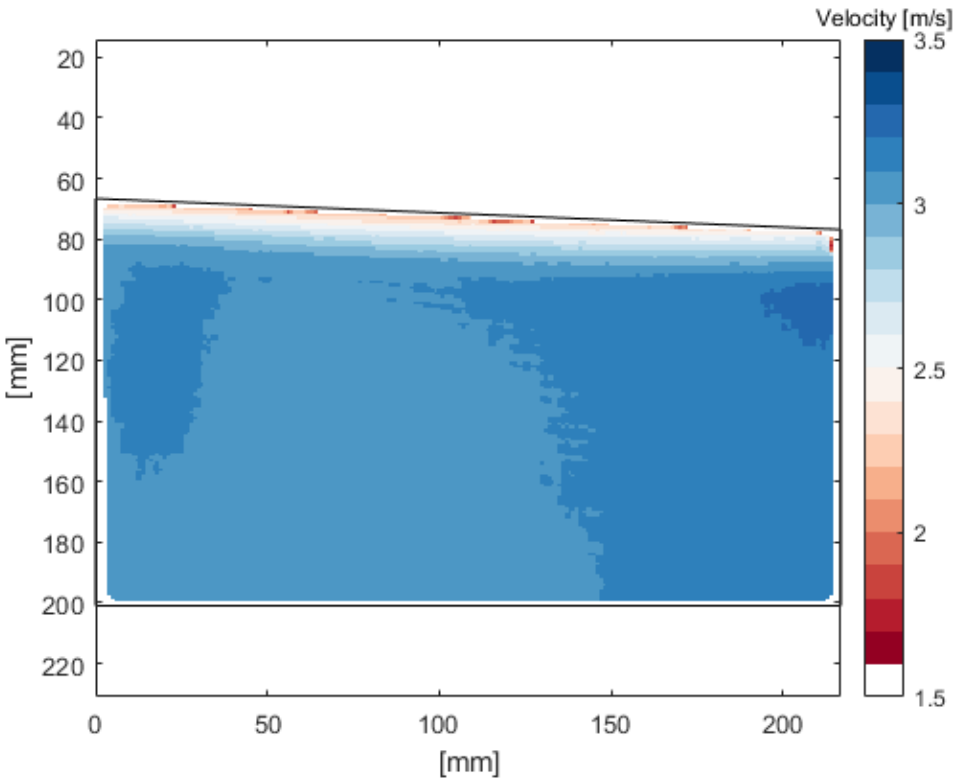

Figure E.1: Flow field for straight stern, v=3, $\theta = 3$

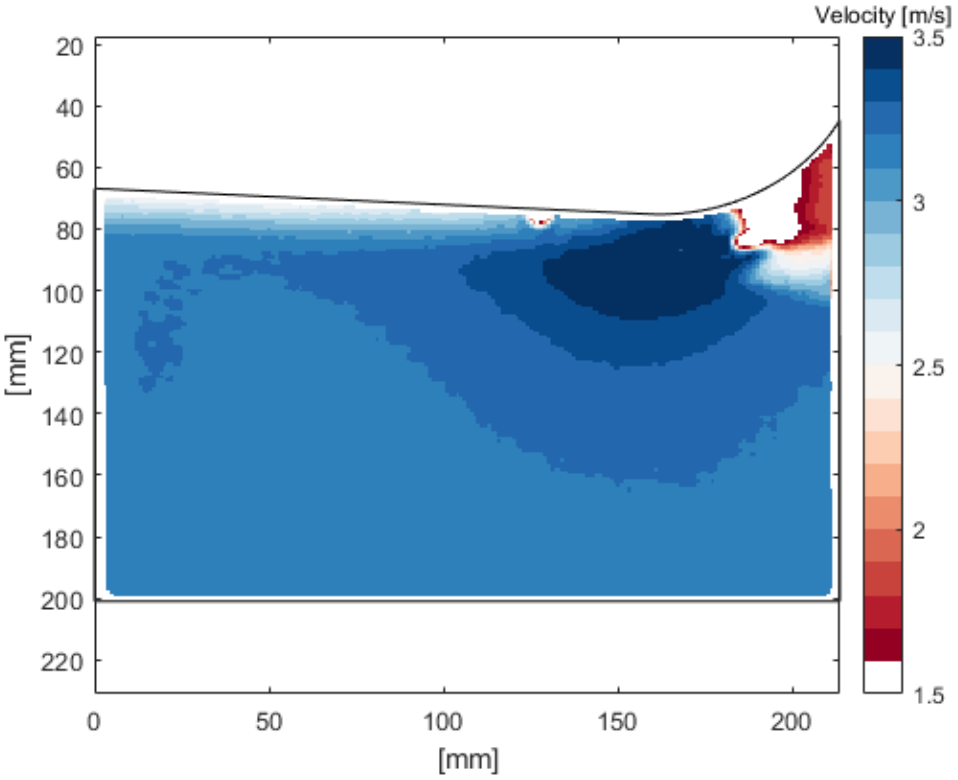

Figure E.2: Flow field for r=50 stern, v=3, $\theta = 3$

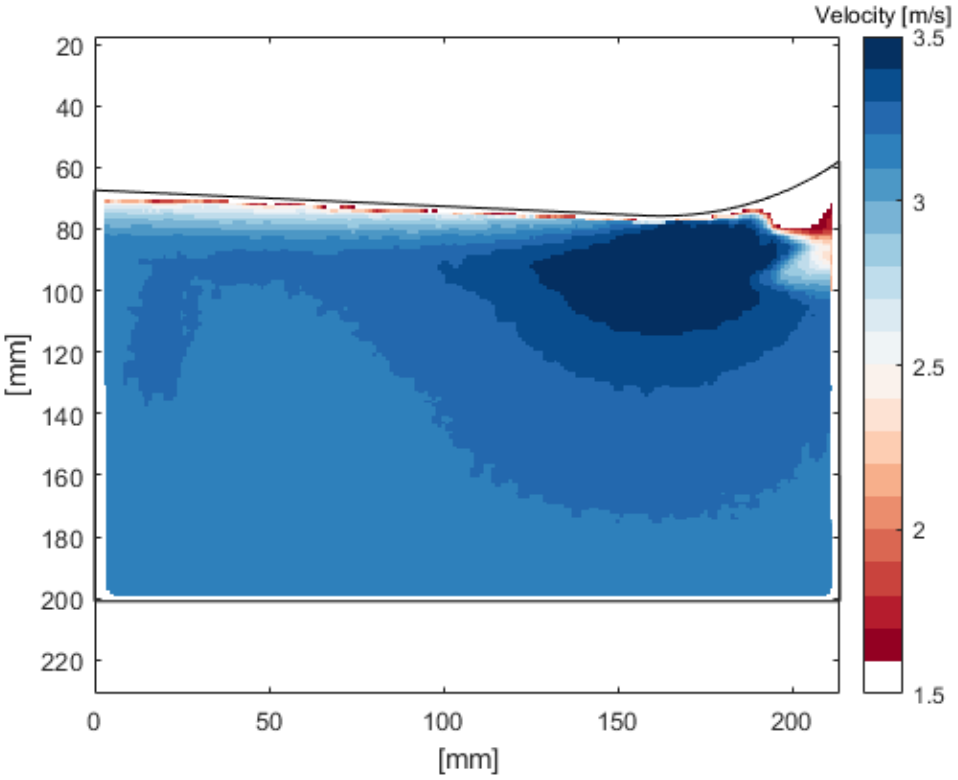

Figure E.3: Flow field for r=70 stern, vm=3, $\theta = 3$

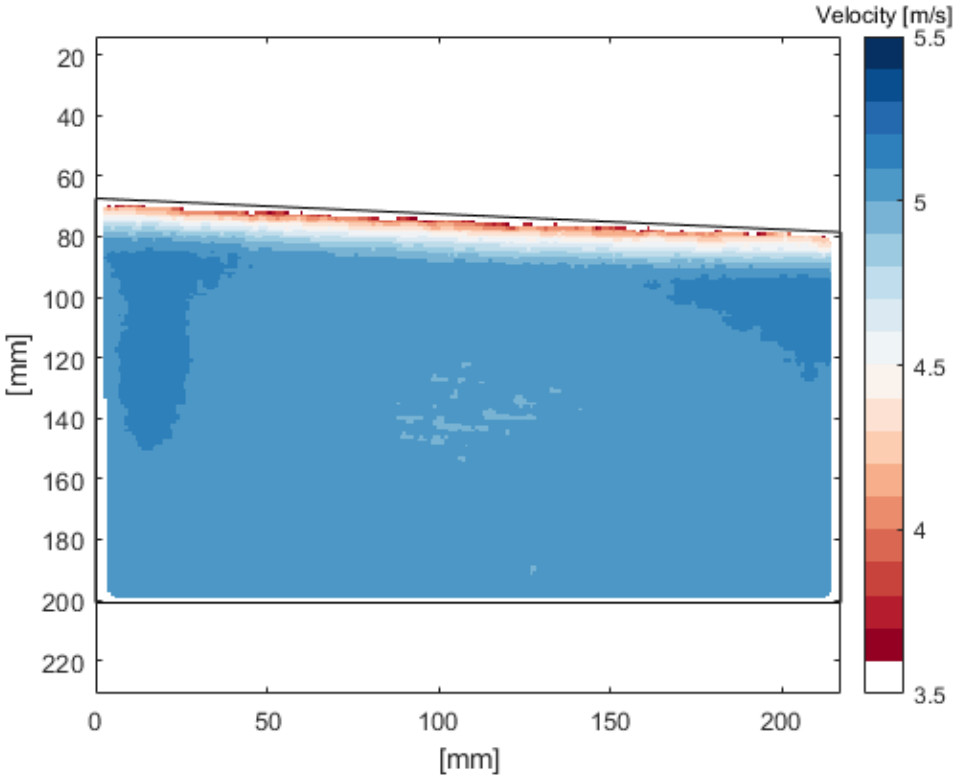

Figure E.4: Flow field for straight stern, vm=5, $\theta = 3$

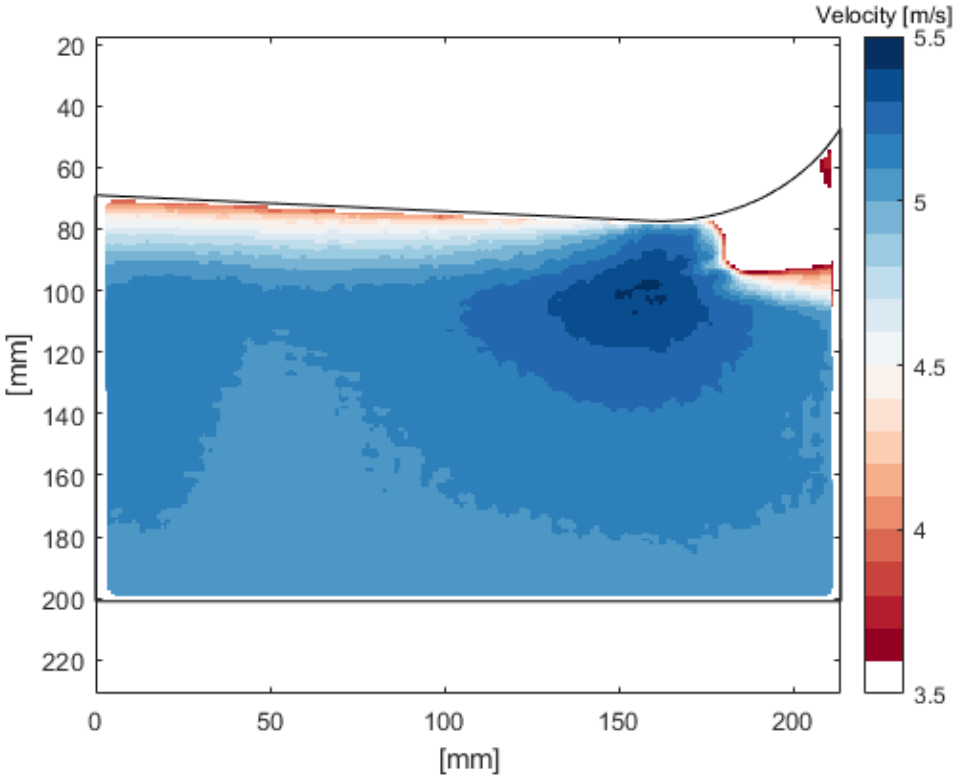

Figure E.5: Flow field for r=50 stern, vm=5, $\theta = 3$

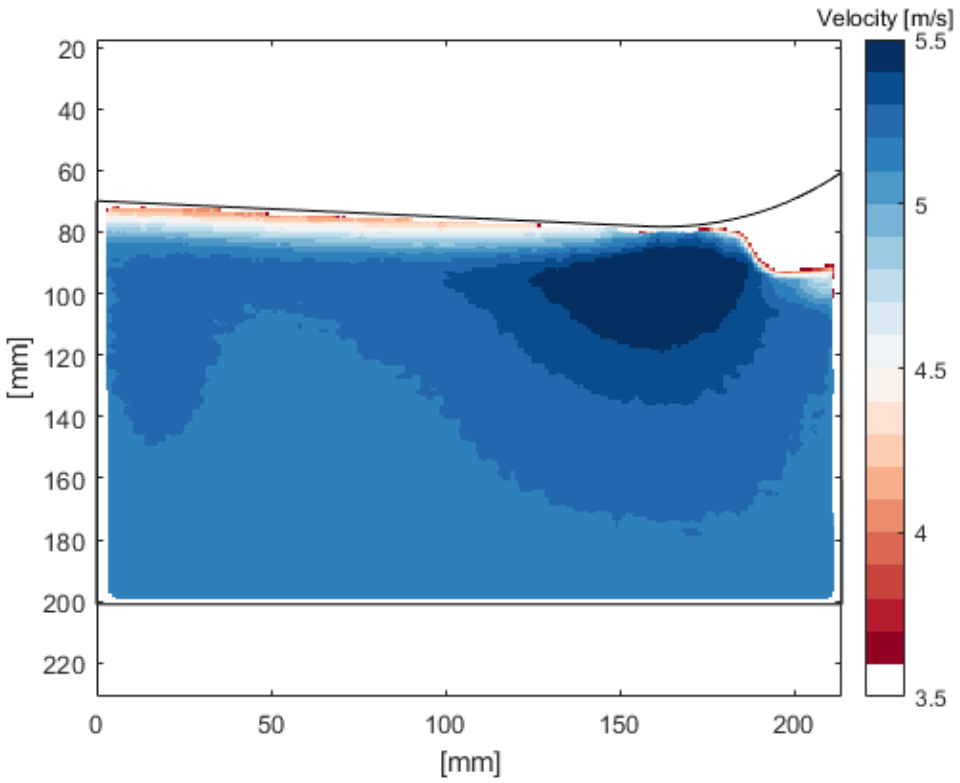

Figure E.6: Flow field for r=70 stern, vm=5, $\theta = 3$

E.2. Boundary layer development

The development of the boundary layer over the hulls are shown in figures E.7, E.8 and E.9.

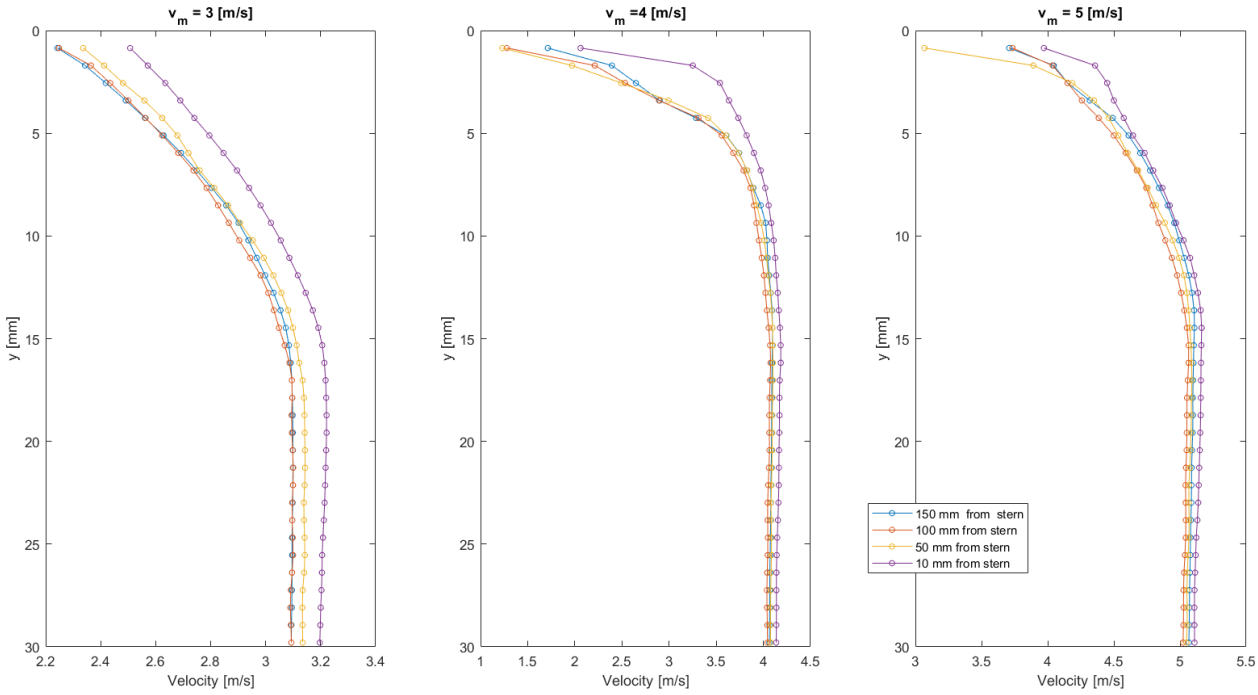

Figure E.7: Development of the boundary layer under the stern shape r=0

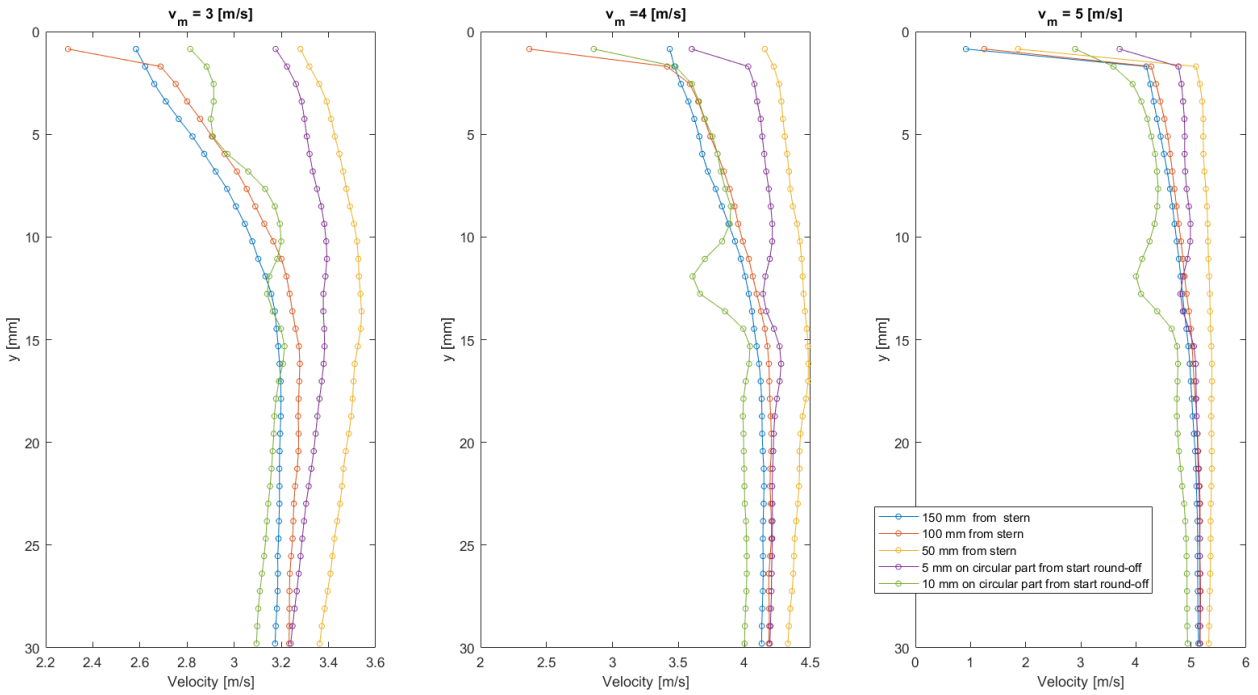

Figure E.8: Development of the boundary layer under the stern shape r=50

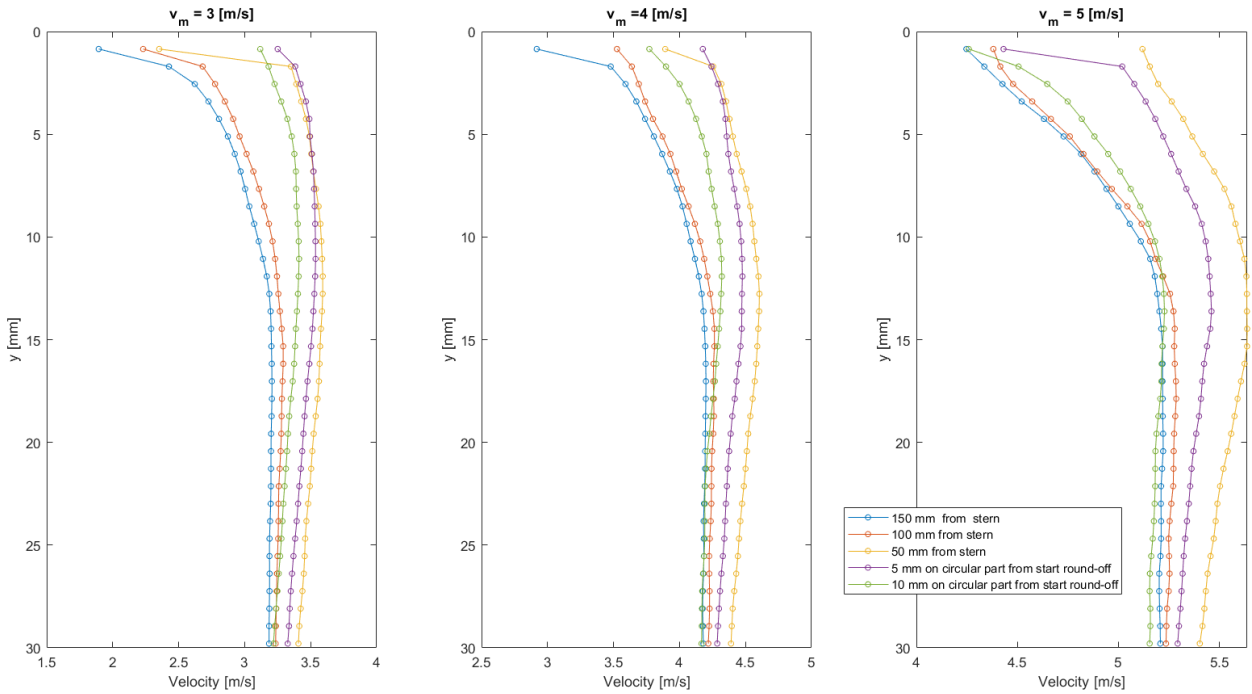

Figure E.9: Development of the boundary layer under the stern shape r=70

About the straight stern shape boundary layer profiles it can be observed that the flow accelerated over the whole measured distance. The velocity increases over the chosen hull points. In case of the round-off sterns, the flow accelerates until the start of the rounding, and decelerates afterwards.

F

Additional results: forced pitch oscillations

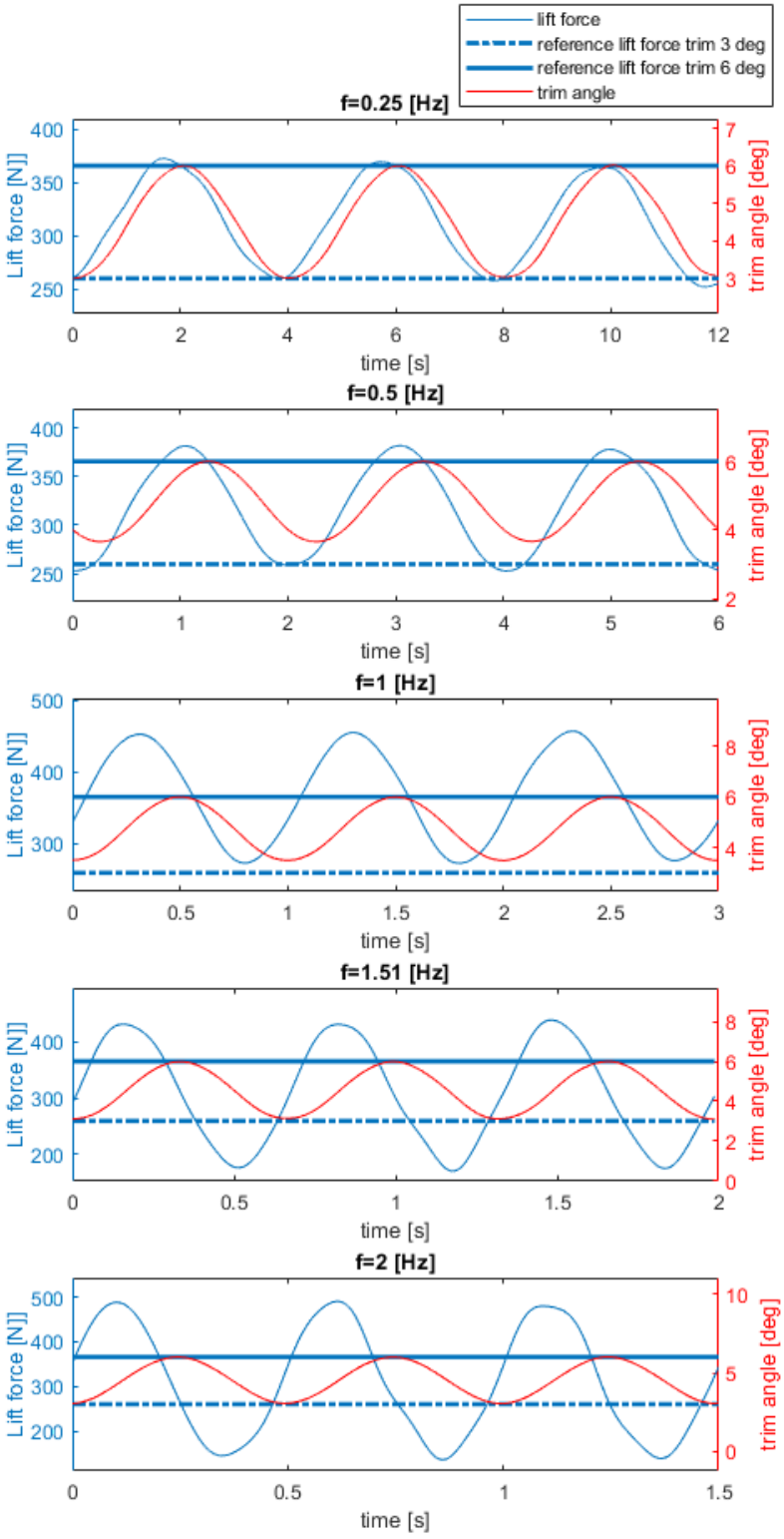

Figure F.1: Lift force during forces pitch oscillations of stern shape r=70

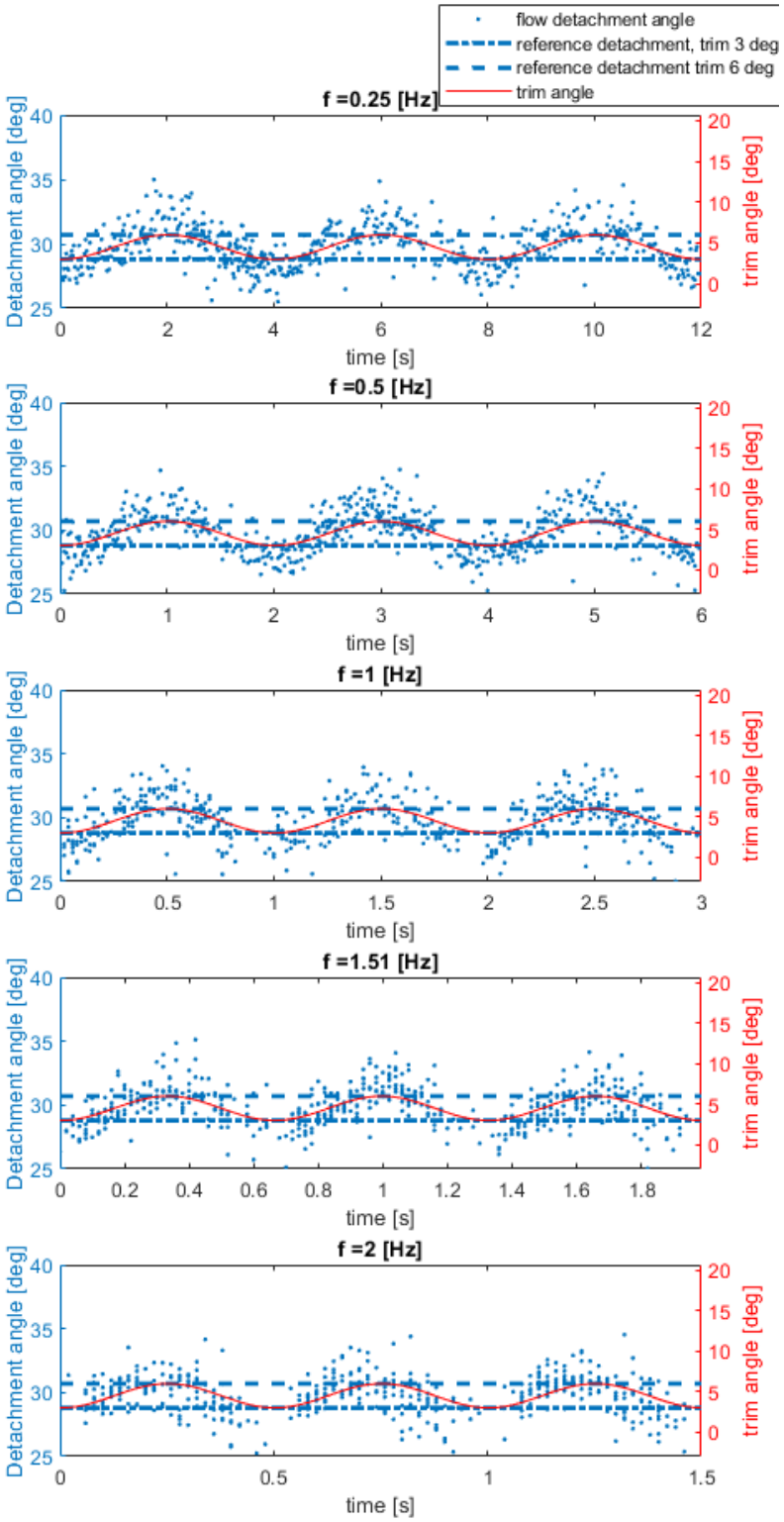

Figure F.2: Flow detachment angle during forced pitch oscillations of stern shape r=70

Bibliography

Bibliography

Lara Adrian, Ronald J Adrian, and Jerry Westerweel. *Particle image velocimetry*. Number 30. Cambridge university press, 2011.

P Anschau and K P Mach. Application of a Stereo PIV System for Investigations of Flow Fields in Towing Tank and Cavitation Tunnel. Technical Report 3, 2007.

Stefano Brizzolara. Hydrodynamic analysis of interceptors with CFD methods. In *7th Int. Conference on Fast Sea Transportation - FAST 2003*, Ischia, 2003.

Tuncer Cebeci, G. J. Mosinskis, and A. M.O. Smith. Calculation of separation points in incompressible turbulent flows. *Journal of Aircraft*, 9(9):618–624, 1972. ISSN 00218669. doi: 10.2514/3.59049.

Paul K Chang. *Separation of flow*. Elsevier, 2014.

MHMA Cleijsen. Trim control-motion reduction of fast-planing vessels with actively controlled trim devices. *Student Thesis, Confidential*, 2013.

Donald Coles. The law of the wake in the turbulent boundary layer. 1956. doi: 10.1017/S0022112056000135.

D Dawson and D Blount. Trim control. *Professional boatbuilder*, 75, 2002.

Pepijn De Jong. Seakeeping behaviour of high speed ships: An experimental and numerical study [ph. d. thesis]. 2011.

Ronald R. Dong, Joseph Katz, and Thomas T. Huang. On the structure of bow waves on a ship model. *Journal of Fluid Mechanics*, 346:77–115, 9 1997.

David Dussol, Philippe Druault, Bachar Mallat, Sylvain Delacroix, and Grégory Germain. Automatic dynamic mask extraction for PIV images containing an unsteady interface, bubbles, and a moving structure. *Comptes Rendus - Mecanique*, 344(7):464–478, 7 2016. ISSN 16310721. doi: 10.1016/j.crme.2016.03.005.

Tale F Egeberg, Hyunse Yoon, Frederick Stern, Bjørnar Pettersen, and Shanti Bhushan. Vortex shedding from a ship hull by means of tomographic piv. In *International Conference on Offshore Mechanics and Arctic Engineering*, volume 45509, page V08AT06A030. American Society of Mechanical Engineers, 2014.

M Falchi, S Grizzi, G Aloisio, M Felli, and F Di Felice. Critical issues in the application of Stereo-PIV in large hydrodynamic facilities: study of a catamaran in steady drift. In *10th international symposium on particle image velocimetry*, 2013.

Massimo Falchi, Mario Felli, Silvano Grizzi, Giovanni Aloisio, M Falchi, • M Felli, • S Grizzi, • G Aloisio, • R Broglia, and • F Stern. SPIV measurements around the DELFT 372 catamaran in steady drift. *Exp Fluids*, 55:1844, 2014. doi: 10.1007/s00348-014-1844-z.

Odd M Faltinsen. *Hydrodynamics of high-speed marine vehicles*. Cambridge university press, 2005.

Paul S Granvlle. A method for the calculation of the turbulent boundary layer in a pressure gradient. Technical report, Navy Department The David w. Taylor model basin, Washington, 5 1951.

L Gui, J Longo, and F Stern. Towing tank PIV measurement system, data and uncertainty assessment for DTMB Model 5512. Technical report, 2001.

Chun-Yu Guo, Tie-Cheng Wu, Wan-Zhen Luo, Xin Chang, Jie Gong, and Wen-Xuan She. Experimental study on the wake fields of a Panamax Bulker based on stereo particle image velocimetry. *Ocean Engineering*, 165(91-106), 2018.

Jakob Pinkster J.A. Keuning and J. van der Velde. The design of a rib lifeboat using the ”enlarged ship concept”. *Work Boat World Europe*, 2002.

Gunnar Jacobi. *The application of particle image velocimetry for the analysis of high speed craft hydrodynamics*. PhD thesis, TU Delft, 2020.

JA Keuning, J Pinkster, and F Van Walree. Further investigations into the hydrodynamic performance of the axe bow concept. In *6th Symposium on High Speed Marine Vehicles (WEMT), Castello di Baia, Italy*, pages 25–38, 2002.

Mohammad Hasan Khademi, Ali Zeinolabedini Hezave, Dariush Mowla, and Mansour Taheri. A simple model for turbulent boundary layer momentum transfer on a flat plate. *Chemical Engineering and Technology*, 33(6):867–877, 6 2010.

KNRM/Flyingfocus. Nieuwste reddingboot komt naar terschelling. https://skylgenet.nl/nieuws-terschelling/2015/04/nieuwste-reddingboot-komt-naar-terschelling/, april 2015.

Pijush K. Kundu, Ira M. Cohen, David R. Dowling, and Tryggvason Grétar. *Fluid mechanics*. Academic Press, 2016.

J Longo, J Shao, M Irvine, and F Stern. Phase-Averaged PIV for the Nominal Wake of a Surface Ship in Regular Head Waves. *Journal of Fluids Engineering*, 129:524–540, 2007.

Joost Margés. Frisc kent eigen kracht niet. https://magazines.defensie.nl/allehens/2018/01/00_frisc, Feb 2018.

Maritime and Coastguard Agency. Mgn 353 (m+f), the merchant shipping and fishing vessels (control of vibration at work) regulations 2007.

John Nicholas Newman. *Marine hydrodynamics*. The MIT press, 2018.

Kartavya Patel. *Airfoil Boundary Layer Separation Prediction*. PhD thesis, San Jose State University, 2014.

Francisco Pedocchi, J. Ezequiel Martin, and Marcelo H. García. Inexpensive fluorescent particles for large-scale experiments using particle image velocimetry. *Experiments in Fluids*, 45(1):183, 7 2008.

Francisco Pereira, Tiziano Costa, Mario Felli, Guido Calcagno, and Fabio Di Felice. A versatile fully submersible stereo-PIV probe for tow tank applications. In *Proceedings of the ASME/JSME Joint Fluids Engineering Conference*, volume 1 A, pages 101–106. American Society of Mechanical Engineers, 2003.

E M Pogozelski, J Katz, and T T Huang. The flow structure around a surface piercing strut. *Physics of Fluids*, 9:1387, 1997.

A Rijkens, H Cleijsen, and J Keuning. On the hydrodynamic performance of an improved motion control device for fast ships. pages 2–5, 2013.

Albert AK Rijkens. *Proactive Control of Fast Ships: Improving the seakeeping behaviour in head waves*. PhD thesis, 2016.

Donald Ross. Evaluation of the momentum integral equation for turbulent boundary layers. *Journal of aeronautical sciences*, 3 1953.

Von J Rotta. Statistische Theorie niehthomogener Turbulenz. *Zeitschrift für Physik*, 131, 8 1951.

Abdollah Sakaki, Hassan Ghassemi, and Shayan Keyvani. Evaluation of the Hydrodynamic Performance of Planing Boat with Trim Tab and Interceptor and Its Optimization Using Genetic Algorithm. *Journal of Marine Science and Application*, 18(2):131–141, 6 2019.

Jeonghwa Seo, Dong Myung Seol, Bumwoo Han, and Shin Hyung Rhee. Turbulent wake field reconstruction of VLCC models using two-dimensional towed underwater PIV measurements. *Ocean Engineering*, 118:28–40, 5 2016.

Ke-Wei Song, Chun-Yu Guo, Jie Gong, Ping Li, and Lian-Zhou Wang. Influence of interceptors, stern flaps, and their combinations on the hydrodynamic performance of a deep-vee ship. *Ocean Engineering*, 2018.

J Tukker, JJ Blok, G Kuiper, and RHM Huijsmans. Wake flow measurements in towing tanks with piv. In *Proceedings of the Ninth International Symposium on Flow Visualization*, 2000.

Alex FJ Van Deyzen. *Improving the operability of planing monohulls using proactive control: From idea to proof of concept*. PhD thesis, 2014.

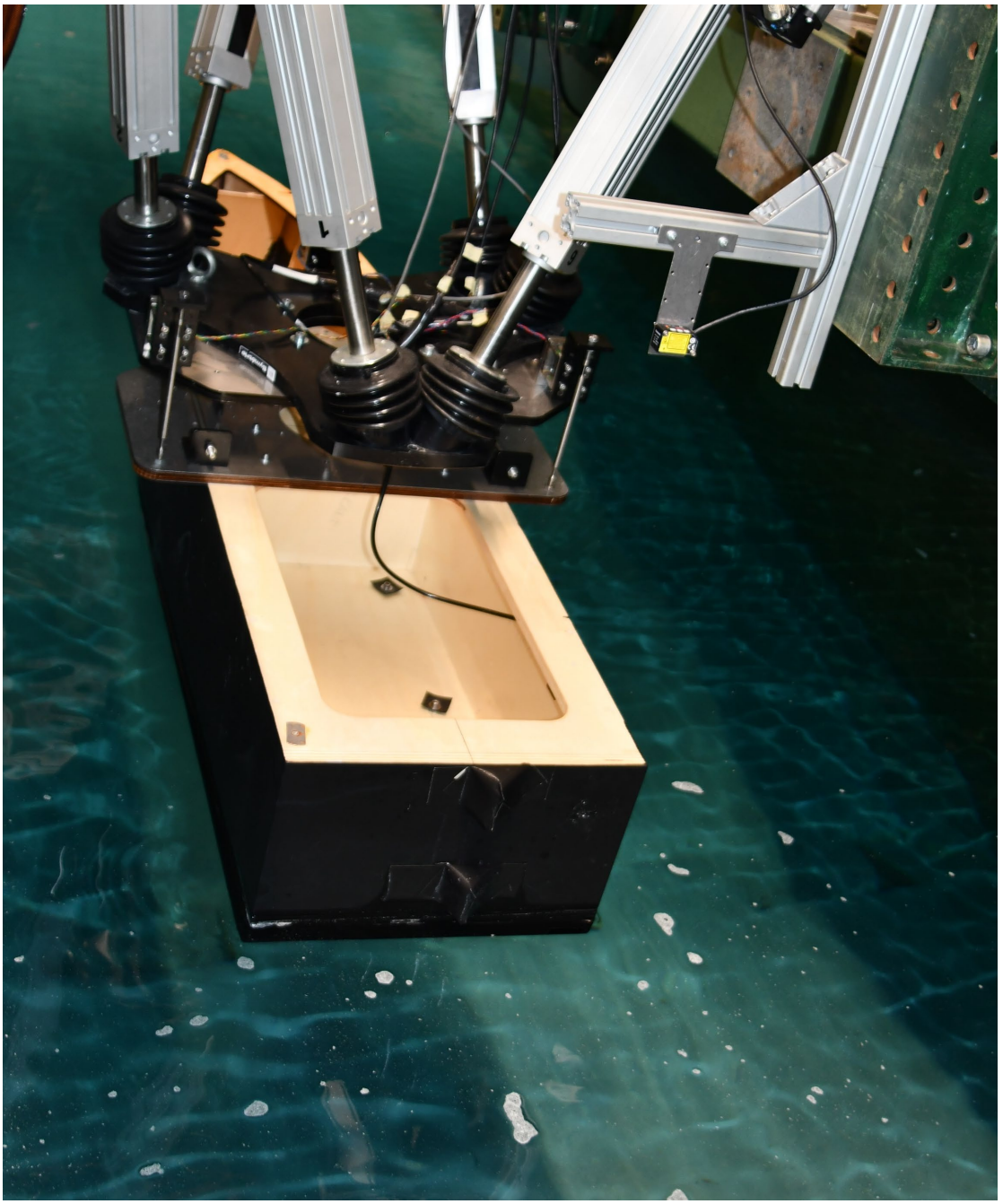

TU Delft

DAMEN